

# Coherent Disaggregation and Uncertainty Quantification for Spatially Misaligned Data

Man Ho Suen<sup>1</sup>, Mark Naylor<sup>2</sup>, and Finn Lindgren<sup>3</sup>

<sup>1,3</sup>School of Mathematics and Maxwell Institute for Mathematical Sciences, University of Edinburgh, Edinburgh, UK

<sup>2</sup>School of GeoSciences, University of Edinburgh, Edinburgh, UK

<sup>1</sup>email address: [m.h.suen@sms.ed.ac.uk](mailto:m.h.suen@sms.ed.ac.uk)

## Abstract

Spatial misalignment problems arise from both data aggregation and attempts to align misaligned data, leading to information loss. We propose a Bayesian disaggregation framework that links misaligned data to a continuous domain model using an iteratively linearised integration method via integrated nested Laplace approximation (INLA). The framework supports point pattern and aggregated count models under four covariate field scenarios: *Raster at Full Resolution (RastFull)*, *Raster Aggregation (RastAgg)*, *Polygon Aggregation (PolyAgg)*, and *Point Values (PointVal)*. The first three involve aggregation, while the latter two have incomplete fields. For PolyAgg and PointVal, we estimate the full covariate field using *Value Plugin*, *Joint Uncertainty*, and *Uncertainty Plugin* methods, with the latter two accounting for uncertainty propagation. These methods demonstrate superior performance, and remain more robust even under model misspecification (i.e. modelling a nonlinear field as linear).

In landslide studies, landslide occurrences are often aggregated into counts based on slope units, reducing spatial detail. The results indicate that point pattern observations and full-resolution covariate fields should be prioritized. For incomplete fields, methods incorporating uncertainty propagation are preferred. This framework supports landslide susceptibility and other spatial mapping, integrating seamlessly with INLA-extension packages.

Keywords: integrated nested Laplace approximation, inlabru, landslides, spatial misalignment, approximate Bayesian computation, uncertainty quantification

# 1 Introduction

The use of the approximate Bayesian inference packages, `R-INLA` and `inlabru`, is gaining popularity in the field of geoscience (Bachl et al., 2019). Specifically, see recent papers, Bayliss et al. (2020); Naylor et al. (2022), in earthquake modelling, and Lombardo et al. (2018, 2019); Loche et al. (2022); Opitz et al. (2022), in earthquake-induced landslides (EQIL) literature. These packages provide rapid and accurate spatio-temporal assessment to EQIL susceptibility which are notoriously hard to predict.

One of the EQIL modelling challenges is to address the data misalignment or assimilation between point-based observations in space and covariates in other resolution scales. A common approach is to aggregate these points into counts defined by certain criteria, such as using slope units (Opitz et al., 2022) or applying a weighting method (Cameletti et al., 2019). Slope units represent terrain partitions of space bounded by drainage and divide lines that these partitions are delimited by their geomorphological characteristics (Alvioli et al., 2020). The assumption is the slope units characterise a collection of underlying trigger factors. However, these trigger factors may have sophisticated structures and change drastically within each slope unit polygon across the evolution of pre-seismic, coseismic, and post-seismic phases. In fact, post-seismic remobilisations are not uncommon (Quigley et al., 2016; Fan et al., 2018). Additionally, monsoon precipitation in the countries like Nepal is likely to perturb the underlying landslides drivers within these units (Jones et al., 2021). Defining slope unit scale and landslides mapping require manual adjustments on terrain and areal parameters. Therefore, relying on slope units to stay constant and unbiased for post-seismic landslides modelling could be wishful thinking. Research suggests that the slope units do not systematically retain the post-seismic landslide susceptibilities (Kincey et al., 2023), which reflect the likelihoods of landslides across space or space-time, modelled via spatial random fields given certain triggering factors (see Section 2).

Nonetheless, it is unrealistic for model prediction to adaptively or simultaneously update these slope unit polygons across time often due to lack of real-time data. More importantly, bias introduced through such aggregation is two-fold. First, the model unavoidably uses proxy covariates

of the slope units to model the landslide count data. Second, it is the loss of the point observation locations, which in turn introduce extra undesired uncertainty. Retaining point information is the cornerstone of point pattern analysis. Some may argue that EQIL are not point pattern events initially and there are multiple ways to define the starting point. More adversely, these points are manually registered, making them prone to errors and bias. Nonetheless, the more precise the locations are the less uncertainty is propagated when constructing the continuous random field. In contrast, the uncertainty propagation in the aggregate polygon setting is intractable since the exact locations of the events are lost while aggregating into counts. Therefore, the uncertainty induced by each event and the resolution scales of the covariate data cannot be tracked down because they are blended inside each aggregate polygon through summary statistics, for example, mean and median.

In reality, it is common to observe only a limited subset of the continuous covariate field. This leads to the choice of whether to reconstruct the covariate field jointly (i.e. one stage), or via two stages. The one-stage approach is often less common in the literature due to the undesirable feedback in joint estimation for spatial models. Examples include autoregressive disturbances with spatial autoregressive models (Kelejian and Prucha, 1998), spatial disaggregation with environmental feedback on land-use transport models (Spiekermann and Wegener, 2008), and two-stage approach on incorporating spatial lag autocorrelation (Lambert et al., 2010). However, it remains unclear in what situation and how the joint estimation (i.e. one-stage) and two-stage approach would affect the model performance in the more flexible INLA-SPDE setting since the neighbouring structure is much finer in scale that depends on the mesh (Rue et al., 2018).

The computation cost is a challenge in modelling EQIL susceptibility given geoscience data are often large-scale. Current EQIL assessments are not rapid enough for post-earthquake humanitarian response (Williams et al., 2018). The wealth of satellite data and recent downscaling techniques, thanks to the advance of remote-sensing technology, soar up computation demand. Questions remain unanswered on how downscaling improves accuracy of the modelling and avoids wasting computational resources. Moreover, we want to formulate a fast and accurate model so

that the least risky post-seismic route of rescue can be computed for optimising resource allocation.

As an example of operational use case of EQIL susceptibility models, the optimal rescue route plans would depend on setting an arbitrary risk threshold for landslide hazard. Given limited time and resources, we can only focus on EQIL above a certain scale which are close to populated area and human property. This leads to anthropogenic drivers of landsliding, in particular road construction. Initial indications suggest that this proliferation of rural roads is leading to extensive landslide hazard-related issues (Kincey et al., 2021; Rosser et al., 2021).

In this paper, we address how to (i) strike a balance between computation and model accuracy when aligning the point data observation and the data resolution, i.e. data misalignment, via linearisation; (ii) model aggregated count and covariate data, incomplete covariate fields (e.g. missing data and downscaling) and incorporate the uncertainty of these fields into the model; and, (iii) handle model misspecification for nonlinear transformations of incomplete covariate fields.

## 2 Definition of Poisson Point and Count Processes

In this paper, we consider unmarked point process and a bounded domain  $\Omega \subset \mathbb{R}^d$ ,  $d \in \mathbb{N}$ . However, our framework for aggregated data is extendable to marked point process, as well as space and time  $\Omega \times T$  settings.

**Definition 2.1** (Poisson Point Process). *Let  $Y \subset \Omega$  be a countable random subset of points. We define a Poisson point process for  $Y$  with an intensity function  $\lambda : \Omega \rightarrow [0, \infty)$  via the counts of points for every Borel measurable set  $A \subseteq \Omega$ ,  $N_Y(A) = \text{card}(Y \cap A)$ , where  $\text{card}(\cdot)$  denotes the cardinality of a set. The counts are Poisson distributed with mean  $\Lambda(A)$ , which is assumed to be non-negative and finite,*

$$N_Y(A) \sim \text{Pois}[\Lambda(A)], \text{ and } \Lambda(A) = \int_{\mathbf{s} \in A} \lambda(\mathbf{s}) d\mathbf{s}, \quad (1)$$

where  $\lambda(\cdot)$  is the intensity function.

If the log intensity function of a spatial point process is a Gaussian random field, this point process is called log-Gaussian Cox process (LGCP) (Møller et al., 1998; Diggle, 2013). In the case of aggregated count observations, we extend the Poisson point process to a Poisson count process.

**Definition 2.2** (Poisson Count Process). *Let  $\{A_p \mid p = 1, \dots, n_A\}$  be disjoint and bounded aggregation sets (regions/volumes) and  $N_p$  be the count of points in  $A_p \subset \Omega$ ,*

$$N_p := N_Y(A_p) \sim \text{Pois} \left( \int_{A_p} \lambda(\mathbf{s}) d\mathbf{s} \right). \quad (2)$$

We define a Poisson count process  $\mathcal{N} := \{N_p\}$  with intensity function  $\lambda : \Omega \rightarrow [0, \infty)$ .

Suppose that we have a point pattern observation  $\mathcal{Y} = \{y_1, \dots, y_N\}$ , where  $N$  is a random variable, the density of  $\mathcal{Y}$  given the intensity function  $\lambda$  and  $N$  being realised to  $n$  is (see Appendix A.1 for derivation),

$$p_Y(\mathcal{Y}, N = n | \lambda) = \frac{e^{-\Lambda(\Omega)}}{n!} \prod_{i=1}^n \lambda(y_i).$$

**Definition 2.3** (Log-likelihood of Poisson Point Process). *The likelihood can be defined as a ratio with respect to a homogeneous Poisson point process, i.e.  $\lambda \equiv 1$ ,*

$$\mathcal{L}(\lambda | \mathcal{Y}) := \frac{p_Y(\mathcal{Y}, N = n | \lambda)}{p_Y(\mathcal{Y}, N = n | \lambda \equiv 1)} = e^{|\Omega| - \Lambda(\Omega)} \prod_{i=1}^n \lambda(y_i). \quad (3)$$

The log-likelihood of a Poisson Point Process is

$$\ell(\lambda | \mathcal{Y}) = \log \mathcal{L}(\lambda | \mathcal{Y}) = \underbrace{|\Omega|}_{\text{domain volume}} - \underbrace{\int_{\Omega} \lambda(\mathbf{s}) d\mathbf{s}}_{\text{domain contribution}} + \underbrace{\sum_{i=1}^n \log \lambda(y_i)}_{\text{observed point contribution}}. \quad (4)$$

**Definition 2.4** (Log-likelihood of Poisson Count Process). *We define the log-likelihood of a Pois-*

son count process

$$\ell(\lambda|\mathcal{Y}, \{A_p\}) = \underbrace{|\Omega|}_{\text{domain volume}} - \underbrace{\int_{\Omega} \lambda(\mathbf{s}) d\mathbf{s}}_{\text{domain contribution}} + \underbrace{\sum_{p=1}^{n_A} \log \lambda(A_p)}_{\text{observed count contribution}} . \quad (5)$$

It is straightforward to compute the observed contribution once we define a log-intensity function as a linear model and extendable to a monotonic increasing nonlinear model. The domain contribution is analytically intractable and would be ideally approximated in a computationally efficient manner (Simpson et al., 2016). Having a triangulation over the domain, we can approximate the spatial random effect in a latent field  $\mathbf{s} \in \mathbb{R}^d$  with  $K$  vertices via a basis expansion,

$$u(\mathbf{s}) = \sum_{k=1}^K \psi_k(\mathbf{s}) u_k, \text{ and } \mathbf{u} = (u_1, \dots, u_k) \sim \mathbf{N}(\mathbf{0}, \mathbf{Q}^{-1}), \quad (6)$$

where  $\{\psi_k\}$  is a set of piecewise linear basis function and  $\mathbf{u}$  are Gaussian distributed weights with a sparse covariance matrix  $\mathbf{Q}^{-1}$ . For illustration, we define the linear predictor to connect to the covariate data  $X(\mathbf{s})$  in a purely spatial setting that is extendable to space-time setting,

$$\log \lambda(\mathbf{s}) \approx \eta(\mathbf{s}) := \mathbf{1}\beta_0 + \beta_x X(\mathbf{s}) + u(\mathbf{s}), \text{ and} \quad (7)$$

$$[\log \lambda(s_i) \approx \eta(s_i), i = 1, \dots, n]^{\top} := \mathbf{A}\mathbf{v}, \quad (8)$$

where  $\beta_0$  is an intercept,  $\beta_x$  is the coefficient of the linear fixed effect covariate,  $X(\mathbf{s})$  is the covariate data;  $\mathbf{A}$  is a projector matrix, and  $\mathbf{v} = [\beta_0, \beta_x, \mathbf{u}^{\top}]^{\top}$ . The product  $\mathbf{A}\mathbf{v}$  represents the evaluation of the field defined by the mesh at any given finite set of locations. Given the data, the model can be fitted via the Integrated nested Laplace approximations (INLA) (Rue et al., 2018). Here the predictor  $\eta(\mathbf{s})$  approximates  $\log \lambda(\mathbf{s})$  and this will be explained in Section 4.

For theory,  $u(\cdot)$  is defined as a stationary Gaussian Random Field (GRF) with zero mean and

Matérn covariance function or kernel,

$$\varrho(\mathbf{s}, \mathbf{s}') = \frac{\sigma^2}{\Gamma(\nu)2^{\nu-1}} (\kappa \|\mathbf{s} - \mathbf{s}'\|)^\nu K_\nu(\kappa \|\mathbf{s} - \mathbf{s}'\|), \quad (9)$$

where  $\sigma^2 > 0$  is the marginal variance,  $\nu > 0$  is the smoothness parameter,  $\kappa > 0$  is the range parameter and  $K_\nu$  is the modified Bessel function of second kind. We evaluate the field  $u(\cdot)$  via mapping to the stochastic partial differential equation (SPDE) (Whittle, 1954, 1963; Lindgren et al., 2011). We follow the re-parametrisation of the Penalised Complexity (PC) prior in Fuglstad et al. (2015) by setting  $\nu = \alpha - \frac{d}{2} > 0$  and  $\kappa = \frac{\sqrt{8\nu}}{\rho}$ , with  $\rho$  as the spatial range, i.e.

$$(\kappa^2 - \Delta)^{\frac{\alpha}{2}} [\sqrt{\tau} u(\mathbf{s})] = \mathcal{W}(\mathbf{s}), \quad (10)$$

where  $\Delta = \sum_{i=1}^d \partial^2 / \partial s_i^2$  is the Laplacian operator,  $\tau = \Gamma(\nu) \left[ (4\pi)^{\frac{d}{2}} \Gamma(\nu + \frac{d}{2}) \sigma^2 \kappa^{2\nu} \right]^{-1} > 0$  is the scaling parameter of  $u(\cdot)$  with  $d$  denoting the dimension of the space and  $\mathcal{W}(\mathbf{s})$  as spatial white noise. In this formulation, the covariance function in equation (9) can be rewritten as

$$\varrho(d_s := \|\mathbf{s} - \mathbf{s}'\|) = \frac{\sigma^2}{\Gamma(\nu)2^{\nu-1}} \left( \frac{\sqrt{8\nu} d_s}{\rho} \right)^\nu K_\nu \left( \frac{\sqrt{8\nu} d_s}{\rho} \right). \quad (11)$$

## 2.1 Taylor Approximation for Intensity Contribution

We partition the sample space  $\Omega$  into disjoint subsets  $\Omega_j$ , such that  $\Omega = \bigcup_{j=1}^J \Omega_j$ , and  $\Omega_j \cap \Omega_{j'} = \emptyset$ ,  $j \neq j'$ . The flexibility on how to define  $\Omega_j$  based on different scenarios will be explained in Section 3. We consider aggregated count data over regions defined by sets  $A_p$  in equation (2), for each  $\Omega_j$ ,  $\Omega_j \subseteq A_p$ . Let  $M_j(\mathbf{u}) = \log \left\{ \int_{\Omega_j} \exp[\eta(\mathbf{s})] d\mathbf{s} \right\}$  in the  $j$ -th subset, we approximate the logarithmic integral of the intensity function for each subset  $\Omega_j$  with the first-order Taylor series,

$$M_j(\mathbf{u}) \approx M_j(\mathbf{u}_*) + \mathbf{J}^{(j)}(\mathbf{u}_*)^\top (\mathbf{u} - \mathbf{u}_*) := \overline{M}_j(\mathbf{u}), \quad (12)$$

where  $\mathbf{u}_*$  are the linearisation points of the Taylor approximation, and  $\mathbf{J}^{(j)}(\cdot)$  is the Jacobian matrix, i.e. first-order derivative matrix for  $M_j$  with respect to  $\mathbf{u}$ . Although we ignore the remaining higher-order terms here, we can assess the approximation by checking the leading error term.

Given a stable integration scheme (see Appendix B.5), we discretise the integrals for each  $\Omega_j$  with weights  $w_{jk} > 0$  at the  $k$ -th knot. Similarly, let  $m_j(\mathbf{u}) = \log \left\{ \sum_{k=1}^{n_j} w_{jk} \exp [\eta(\mathbf{s}_{jk})] \right\}$ , with the first-order Taylor series,

$$m_j(\mathbf{u}) \approx m_j(\mathbf{u}_*) + \mathbf{J}^{(j)}(\mathbf{u}_*)^\top (\mathbf{u} - \mathbf{u}_*) =: \bar{m}_j(\mathbf{u}). \quad (13)$$

Derivations of  $\bar{M}_j(\mathbf{u})$  and  $\bar{m}_j(\mathbf{u})$  in equations (12) and (13) can be found in Appendix A.2.

**Theorem 2.1** (Taylor approximation for the continuous and discretised linearisation). *Assume both  $M_j(\mathbf{u})$  and  $m_j(\mathbf{u})$  are twice differentiable at some points  $\mathbf{u}_* \in \mathbb{R}$ ; and the linear predictor  $\eta(\cdot)$  is an affine function of  $\mathbf{u}$ . For the continuous linearisation, we have*

$$M_j(\mathbf{u}) - \bar{M}_j(\mathbf{u}) = \frac{1}{2}(\mathbf{u} - \mathbf{u}_*)^\top \mathbf{H}^{(j)}(\mathbf{u} - \mathbf{u}_*) + \mathcal{O}(\|\mathbf{u} - \mathbf{u}_*\|^3), \quad (14)$$

where  $\mathcal{O}(\|\mathbf{u} - \mathbf{u}_*\|^3)$  is the higher-order terms with respect to  $\|\mathbf{u} - \mathbf{u}_*\|^3$ . For the discretised linearisation, we have

$$m_j(\mathbf{u}) - \bar{m}_j(\mathbf{u}) = \frac{1}{2}(\mathbf{u} - \mathbf{u}_*)^\top \mathbf{H}^{(j)}(\mathbf{u} - \mathbf{u}_*) + \mathcal{O}(\|\mathbf{u} - \mathbf{u}_*\|^3). \quad (15)$$

Both derivations can be found in Appendices A.3 and A.4.

Hence, the domain contribution can be approximated as

$$-\int_{\Omega} \lambda(\mathbf{s}) d\mathbf{s} \approx \begin{cases} -\sum_{j=1}^J \exp [\bar{M}_j(\mathbf{u})] \\ -\sum_{j=1}^J \exp [\bar{m}_j(\mathbf{u})]. \end{cases} \quad (16)$$

We will compare the accuracy between  $\bar{M}_j(\cdot)$  and  $\bar{m}_j(\cdot)$  approximations in equation (16) in

Section 4. See Appendix A.5 for the implementation of the logarithmic sum, i.e.  $\bar{m}_j(\cdot)$  approximation.

### 2.1.1 Taylor Approximation for Discretised Linearisation

In the `inlabru` package, the linearisation approach in equation (16) requires a sequence of runs of the INLA method, each followed by a line search to locate the optimal linearisation point . If the approximation of the domain contribution is not large enough to counter the observed point contributions in equation (4), the approximation of the likelihood can go to infinity in and cause numerical instability (see Appendix B.6). To avoid the observed contribution overpowering the likelihood, we need to bound the domain contribution. Hence, Theorem 2.1 shows that the Jacobian  $\mathbf{J}^{(j)}$  and Hessian  $\mathbf{H}^{(j)}$  terms of  $m_j(\mathbf{u})$  converge in equation (15). The line search continues until the given tolerance is met and refer to Lindgren et al. (2024) with regard to setting the initial linearisation point and the stopping rule to optimise the fit.

## 3 Domain Partition

The subsets  $\{\Omega_j\}$  from Section 2.1 define the resolution of the intensity field in the outcome prediction. Their volumes have to be smaller than the corresponding  $|A_p|$  (see Definition 2.2). There is no benefit in using subsets smaller than the finest data resolution. The Matérn field term  $u(\mathbf{s})$  in equation (7) has to be bounded by the covariate field in the resolution scale since there may be no observation in the triangular mesh and the Gaussian prior is not enough without any data input. Essentially, the degrees of freedom in the SPDE field should be respected (see Section 7.2). Nonetheless, users may downscale the resolution of the covariate data and refine the mesh size accordingly. Under these constraints, the flexibility to define the subsets then takes into account the observed point locations, the data quality, the integration scheme and the computation costs. For illustration, we set the subsets as the user-defined mesh and solve the SPDE equation (10) via Finite Element Method (FEM) (Lindgren et al., 2011, 2022).

### 3.1 Mesh Shape

In light of the tessellation of mesh elements over the domain, we want the subsets to be regularly shaped, i.e. triangles, squares and hexagons. We do not consider mesh-free methods which treat the data points as nodes. Mesh-free methods can handle particle-like finite element analysis, which can be useful for animal tracking since animals interact with one another (Liu, 2009). However, due to these interactions and dynamical nodes, more computation time is required. Additionally, further handling is needed for a stable integration scheme with the current construction of the likelihood. Mixed-shaped meshes are not considered because their construction can be too flexible and thus more complicated to implement.

Discretisation and orientation effects are undesirable. In this regard, circles do not suffer from orientation bias. However, circles do not tessellate. Hexagon meshes suffer less from edge effects since they are almost circular. Another perspective on discretisation effects is that each hexagon has six neighbours and smooths out the discrepancy between nearby hexagons. In general, hexagonal meshes fit curved boundary domains well, and have good accuracy and solving time. We can construct an equilateral regular hexagon from six uniformly sized equilateral triangles. However, we cannot avoid irregular triangular elements between the hexagons and the boundary. Here, we consider triangular elements, which are flexible and simpler to implement. Square elements can match the raster grid data, e.g. satellite imagery, and can be formulated from triangular mesh element construction.

### 3.2 Data resolution and mesh element size

To define the mesh element size, we take the data resolution as baseline. Refining the elements finer than the data does not improve the accuracy. In the Bayesian setting, the posterior would not improve with the same prior without additional data input in the scenarios where the elements are finer than the data. Choosing the mesh resolution is a compromise between computation time and approximation error. Finer elements may increase accuracy but also computation. We can consider uniform and adaptive meshes.

A uniform mesh places uniformly sized elements across and is easy to implement. In real life, we do not know the exact spatial range and anisotropicity of the data a priori, and we often only observe a limited set of data. Hence, we may not know the optimal balance between mesh resolution and computation time. In addition, any adjustments on maximum element edge in the meshing construction criteria changes the structure of the mesh. Therefore, any two meshes with different settings are not fairly comparable. Since there are multiple factors, we do not know exactly how the mesh refinements affect accuracy. As a general rule, we only need to make sure that the resolution of the mesh is sufficiently fine within the domain; in practice, a reasonable rule of thumb is one third in length for the ratio between mesh element and data resolution (see code in Appendix C.6). We will demonstrate this in Section 5.

An adaptive mesh, i.e. with hybrid element size, refines mesh resolution for the desired domain space. In landslides, we mostly care about the regions with human activities. For instance, we would like to know the landslides susceptibility for planning road construction. Adaptivity can be achieved through dual mesh refinement (Rue et al., 2018). Dual mesh enables a gradual and tractable change in the resolution. In some cases, we have higher resolution data i.e. less uncertainty and more information, at observation sites, such as hospital data in urban area compared to rural and animal tracking in ecology. To reflect this need, we place finer elements at these locations without creating nonconforming meshes during refinement (Lindgren, 2018). Given the expectation difference in equation (18), we would have ideas on the error bound. There is further discussion on computing fine lattice in Sections 2 and 7.3 in Simpson et al. (2016).

The  $k$ -th knot for the weight ( $w_{jk}$  from Section 2.1) in the  $j$ -th subset is introduced through integration point. As the total number of knots goes to infinity, the accuracy does not continue to improve given the data resolution. Hence, we choose  $k$  so that the integration is stable and computationally efficient.

## 4 Computation

If  $\eta$  is a nonlinear expression, i.e. non-linear predictor, say  $f(X) = X^{-2}$ , there would be further expansion of  $\mathbf{A}$  from  $\mathbf{b} + \mathbf{A}\mathbf{u}$  which can be grouped into higher-order terms of  $\|\mathbf{u} - \mathbf{u}_*\|$  after differentiation (see Appendix B.1). Hence, the first-order Taylor expansion remains adequate.

Before we proceed to the assessment of nonlinearity, we take a detour to introduce the structure of hierarchical models in INLA. We denote  $\mathbf{y}$  as the realisations of  $\mathcal{Y}$  which are conditionally independent given  $\boldsymbol{\eta}$  and  $\boldsymbol{\theta}$  in the INLA setting. The INLA implementation requires incorporating the covariance parameters  $\boldsymbol{\theta}$  into equation (6) such that  $\boldsymbol{\theta} \sim p(\boldsymbol{\theta})$ ;  $\mathbf{u}|\boldsymbol{\theta} \sim N(\boldsymbol{\mu}_{\mathbf{u}}, \mathbf{Q}_{\boldsymbol{\theta}}^{-1})$ , and  $\mathbf{y}|\mathbf{u}, \boldsymbol{\theta} \sim p(\mathbf{y}|\eta(\mathbf{u}), \boldsymbol{\theta})$ .

We aim to assess how well the linearisation of the predictor works. To this end, we expand the second-order Taylor polynomial terms and compute the bias. We define  $\log \tilde{\mathbb{P}}(\mathbf{u}|\mathbf{y}, \boldsymbol{\theta})$  as the log-density of the true model expressed in the second-order Taylor expansion and higher-order terms  $\mathcal{O}(\|\mathbf{u} - \mathbf{u}_*\|^3)$ , and  $\log \bar{\mathbb{P}}(\mathbf{u}|\mathbf{y}, \boldsymbol{\theta})$  as the log-density of the linearised model yielded from our proposed method. We assess the Kullback-Leibler (KL) divergence between the  $\tilde{\mathbb{P}}(\mathbf{u}|\mathbf{y}, \boldsymbol{\theta})$  and  $\bar{\mathbb{P}}(\mathbf{u}|\mathbf{y}, \boldsymbol{\theta})$ . Indeed, the KL divergence serves as posterior non-linearity evaluation since it is not easy to come up with a distance metric. With Bayes' theorem, we have  $\mathbb{P}(\mathbf{u}|\mathbf{y}, \boldsymbol{\theta}) = \frac{\mathbb{P}(\mathbf{u}, \mathbf{y}|\boldsymbol{\theta})}{\mathbb{P}(\mathbf{y}|\boldsymbol{\theta})} = \frac{\mathbb{P}(\mathbf{y}|\mathbf{u}, \boldsymbol{\theta})\mathbb{P}(\mathbf{u}|\boldsymbol{\theta})}{\mathbb{P}(\mathbf{y}|\boldsymbol{\theta})}$ . Since  $(\mathbf{u}|\boldsymbol{\theta})$  is Gaussian and  $\mathbb{P}(\mathbf{y}|\boldsymbol{\theta})$  is the normalising factor, we focus on the likelihood factor  $\log \mathbb{P}(\mathbf{y}|\mathbf{u}, \boldsymbol{\theta})$ .

**Theorem 4.1** (Expectation on the difference of the linearisation on the observation log-density).

$$\log \frac{\tilde{\mathbb{P}}(\mathbf{y}|\mathbf{u}, \boldsymbol{\theta})}{\bar{\mathbb{P}}(\mathbf{y}|\mathbf{u}, \boldsymbol{\theta})} = - \sum_j e^{\bar{m}_j(\mathbf{u}_*)} \left[ \frac{1}{2} (\mathbf{u} - \mathbf{u}_*)^\top \mathbf{H}^{(j)} (\mathbf{u} - \mathbf{u}_*) + \mathcal{O}(\|\mathbf{u} - \mathbf{u}_*\|^3) \right]. \quad (17)$$

The derivation of equation (17) can be found in Appendix B.2. Then taking expectation, we have

$$\begin{aligned} \mathbb{E}_{\mathbf{u} \sim N(\boldsymbol{\mu}_{\boldsymbol{\theta}}, \mathbf{Q}_{\boldsymbol{\theta}}^{-1})} \left( \log \frac{\tilde{\mathbb{P}}(\mathbf{y}|\mathbf{u}, \boldsymbol{\theta})}{\bar{\mathbb{P}}(\mathbf{y}|\mathbf{u}, \boldsymbol{\theta})} \right) &= -\frac{1}{2} \sum_j e^{\bar{m}_j(\mathbf{u}_*)} [\text{tr}(\mathbf{H}^{(j)} \mathbf{Q}_{\boldsymbol{\theta}}^{-1}) + (\boldsymbol{\mu}_{\boldsymbol{\theta}} - \mathbf{u}_*)^\top \mathbf{H}^{(j)} (\boldsymbol{\mu}_{\boldsymbol{\theta}} - \mathbf{u}_*)] \\ &\quad + \mathcal{O}[\mathbb{E}(\|\mathbf{u} - \mathbf{u}_*\|^3)]. \end{aligned} \quad (18)$$

The derivation of equation (18) can be found in Appendix B.3.

The expectation in equation (18) depends on the  $\mathbf{H}^{(j)}$  yielded from the true likelihood, which in turns relates to both the estimated intensity function  $\hat{\lambda}$ , and the partial derivative of the nonlinear predictor with respect to the linearisation point  $\mathbf{u}_*$ . Both  $\hat{\lambda}$  and  $\mathbf{u}_*$  can be evaluated in INLA. In other words,  $\mathbf{H}^{(j)}$  depends on the nonlinearity in the predictor in  $l$  and  $l'$  dimensions. When  $\mathbf{H}$  is large, the nonlinear terms deviate more from the estimated mode computed from INLA. We can view  $\mathbf{H}^{(j)}\mathbf{Q}_{\theta}^{-1}$  in equation (18) as a correction term, which is composed of the Hessian term and the covariance structure of the Gaussian components  $\mathbf{u}$ . In the case of  $\mu_{\theta} - \mathbf{u}_* = 0$ , it serves as a sanity check as this would minimise the second term.

Now we have all the ingredients to compute the KL divergence. Since the KL divergence is asymmetric, we will compute both  $\text{KL}\left[\tilde{\mathbb{P}}(\mathbf{u}|\mathbf{y}, \theta) \parallel \bar{\mathbb{P}}(\mathbf{u}|\mathbf{y}, \theta)\right]$  and  $\text{KL}\left[\bar{\mathbb{P}}(\mathbf{u}|\mathbf{y}, \theta) \parallel \tilde{\mathbb{P}}(\mathbf{u}|\mathbf{y}, \theta)\right]$ . We follow the proof from Lindgren et al. (2024).

**Theorem 4.2** (Kullback-Leibler (KL) divergence for the first and second Taylor expansion). *Denote  $\mathbf{G} = -\sum_j e^{\bar{m}_j} \mathbf{H}^{(j)}$  and the linearised and approximate nonlinearised posterior distribution as  $N(\bar{\mu}_{\theta}, \bar{\mathbf{Q}}_{\theta})$  and  $N(\tilde{\mu}_{\theta}, \tilde{\mathbf{Q}}_{\theta})$  respectively, we have*

$$\begin{aligned} \text{KL}\left[\tilde{\mathbb{P}}(\mathbf{u}|\mathbf{y}, \theta) \parallel \bar{\mathbb{P}}(\mathbf{u}|\mathbf{y}, \theta)\right] &= \frac{1}{2}\{\log \det(\bar{\mathbf{Q}}_{\theta} - \mathbf{G}) - \log \det(\bar{\mathbf{Q}}_{\theta}) + \text{tr}[\bar{\mathbf{Q}}_{\theta}(\bar{\mathbf{Q}}_{\theta} - \mathbf{G})^{-1}] \\ &\quad - d + (\bar{\mu}_{\theta} - \tilde{\mu}_{\theta})^\top \bar{\mathbf{Q}}_{\theta}(\bar{\mu}_{\theta} - \tilde{\mu}_{\theta})\} + \mathcal{O}\left[\mathbb{E}(\|\mathbf{u} - \mathbf{u}_*\|^3)\right], \text{ and} \end{aligned} \tag{19}$$

$$\begin{aligned} \text{KL}\left[\bar{\mathbb{P}}(\mathbf{u}|\mathbf{y}, \theta) \parallel \tilde{\mathbb{P}}(\mathbf{u}|\mathbf{y}, \theta)\right] &= \frac{1}{2}\{\log \det(\bar{\mathbf{Q}}_{\theta}) - \log \det(\bar{\mathbf{Q}}_{\theta} - \mathbf{G}) + \text{tr}[(\bar{\mathbf{Q}}_{\theta} - \mathbf{G})\bar{\mathbf{Q}}_{\theta}^{-1}] \\ &\quad - d + (\bar{\mu}_{\theta} - \tilde{\mu}_{\theta})^\top (\bar{\mathbf{Q}}_{\theta} - \mathbf{G})(\bar{\mu}_{\theta} - \tilde{\mu}_{\theta})\} + \mathcal{O}\left[\mathbb{E}(\|\mathbf{u} - \mathbf{u}_*\|^3)\right], \end{aligned} \tag{20}$$

where  $d$  is the dimension of the vector  $\mathbf{u}$ . The derivation can be found in Appendix B.4.

We can see the KL divergences have similar structure as in equation (18). We wish to minimise the difference between the linearised and nonlinearised means  $(\bar{\mu}_{\theta} - \tilde{\mu}_{\theta})$ , which minimises the

both divergences. The term  $(\bar{Q}_\theta - G)$  is a sum of linearised precision matrix and the Hessian term, and can therefore be viewed as an approximation of  $\tilde{Q}_\theta$ .

Indeed, these divergences provide insights for the bias. Once we can compute them in the `inlabru` package, we consider different integration schemes based on different mesh construction for the intensity field  $\lambda$ . Although we do not have control of the precision matrix of the Gaussian components  $\mathbf{u}$ , a more linear predictor would imply a smaller  $|G|$ . The implications of nonlinearity is two-fold. Nonlinearity can be induced by the aggregation and/or in the predictor expression. The former can be alleviated by the mesh construction with respect to the aggregation structure. For the latter, we can increase mesh resolution in an adaptive mesh setting for the volume that is more nonlinear. In spite of the increase of the number of elements, it is hoped that we can minimise  $|G|$  with smaller  $H$ .

## 5 Simulation Study

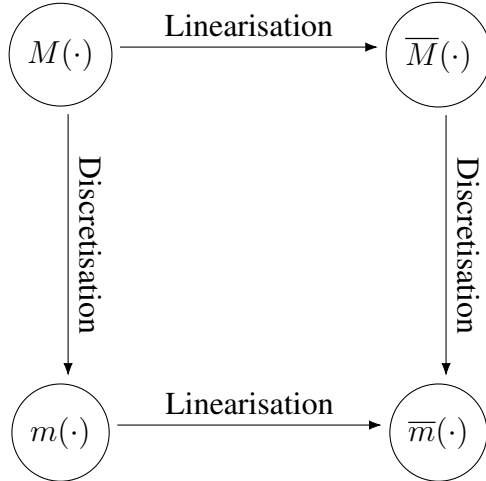


Figure 1: Conceptual diagram of the linearisation and discretisation process. The workflow in the `inlabru` package:  $M(\cdot) \rightarrow m(\cdot) \rightarrow \bar{m}(\cdot)$ . The diagram is not communicative because  $\bar{M}(\cdot) \rightarrow \bar{m}(\cdot)$  depends on the data.

We aim to investigate the relationship of mesh and data resolution regarding the influence on the computation cost and model accuracy, via the linearisation approach. Here we simulate data to illustrate the workflow  $M(\cdot) \rightarrow \bar{M}(\cdot) \rightarrow \bar{m}(\cdot)$  (see Figure 1). More precisely, we cannot evaluate

the discretisation workflow  $\overline{M}(\cdot) \rightarrow \overline{m}(\cdot)$  analytically as this depends on the data. This is the reason why we assess this workflow through the simulation study.

## 5.1 Data

For fair comparison across models, we build two meshes, *mesh (i)* - a hexagonal mesh made of equilateral sub-triangles in the middle, while leaving two triangular edge lengths (i.e.  $2 \times 3.684\text{km}$ ) from the smoothed and buffered inner boundary that covers the entire region, and *mesh (ii)* - half of the resolution of *mesh (i)* (see Appendix C.6 for mesh sizes). The elements along the boundary are constructed according to the meshing algorithm. Hexagonal mesh is known to be optimal in stationary random field setting since it minimizes the discretisation effect. Both the inner and outer boundaries are buffered to smooth the mesh construction via `fmesher::fm_extensions` (see Appendix C.1). Although the integration scheme takes account of the integration points of the triangular meshes that fall outside the boundary of each  $A_p$  (interior boundary) by removing their weights from the integration (see Appendix B.5). A more accurate result could be achieved by constructing the mesh to conform to the interior sub-boundary of each  $A_p$ . This would ensure that none of the integration points fall outside the interior boundary. However, this approach is not implemented in the simulation in Section 5 because the high-resolution interior boundary complicates mesh construction, making the computation expensive.

We simulate point pattern observations over Nepal as a test of method as in equation (1) with the linear predictor

$$\eta(\mathbf{s}) = \beta_0 + \beta_x X(\mathbf{s}) + u(\mathbf{s}), \quad (21)$$

where  $X(\mathbf{s})$  is a continuous covariate field formulated as  $(s_1^2 - s_2^2) \exp\left[-\frac{1}{2}(s_1^2 + s_2^2)\right]$ ;  $s_1 \in [-4, 4]$ ,  $s_2 \in [-2, 2]$  projected to Nepal, and  $u(\mathbf{s})$  is defined in equation (6). We set  $\beta_0 = -7$ ,  $\beta_x = -6$  and  $u(\mathbf{s})$  with  $\rho = 50$  and  $\sigma = 0.5$ . Both  $\beta_0$  and  $\beta_x$  are selected to allow manageable computation for a toy example while the signal of the covariate field can be relatively identifiable compared to the Matérn noise term. We also aggregate count observations  $N_{\mathcal{Y}}(A_p)$  where  $A_p$  is

the  $p$ -th administrative region in Nepal for  $p = 1, \dots, 777$ . This results in 139 simulated observed points. The Coordinate Reference Systems (CRS) of above are projected into Universal Transverse Mercator (UTM) zone 44N and are converted into kilometre (km). We simulate point pattern observations based on the intensity field evaluated pointwise at the *mesh* ( $i$ ) nodes (see code and plots in Appendices C.2 and C.3 respectively).

### 5.1.1 Simulation Scenarios

We consider both point pattern or aggregated count observations with the following scenarios for the observed covariate field: 1) Perfect detection of every covariate raster at full resolution (RastFull) of  $0.858\text{km} \times 0.859\text{km}$  (Section 5.1.2); 2) Covariate raster aggregation (RastAgg) by taking the mean of the RastFull, at a resolution of  $8.584\text{km} \times 8.592\text{km}$  (Section 5.1.2); 3) Polygon aggregation (PolyAgg) by taking the mean of the RastFull across administrative regions in Nepal, i.e.  $n_A = 777$  piecewise-constant polygons (Section 5.1.2); 4) Incomplete covariate field of Point Values (PointVal) and PolyAgg (Sections 5.1.3 and 5.2.2); and 5) nonlinear model misspecification of PolyAgg and PointVal. We refer Scenarios 1) to 3) as aggregation scenarios, and Scenario 4) as incomplete covariate field scenario. We refer to the covariate field input method in RastFull, RastAgg and PolyAgg as Observations Plugin (OP). We then extend Scenarios 3) and 4) to Scenario 5): Nonlinear (NL) misspecification. More precisely, these are model mismatches using linear models to fit the observations with a nonlinear transformed covariate field under an incomplete covariate field setting (Section 5.2.6). We summarise above in a flowchart in Figure 2.

The function on the mesh is defined to be piecewise linear, hence the resolution of the mesh should be similar to that of the data in the optimal case; otherwise we do not fully utilitise the data information. Having said that, the mesh resolution in the simulation is roughly 4 times larger than the covariate raster data at full resolution in Scenario 1). Here we compromise the information from the data to make the computation more efficient. Therefore, it provides insight into the case when we slightly relax the rule of thumb mentioned in Section 3.2.

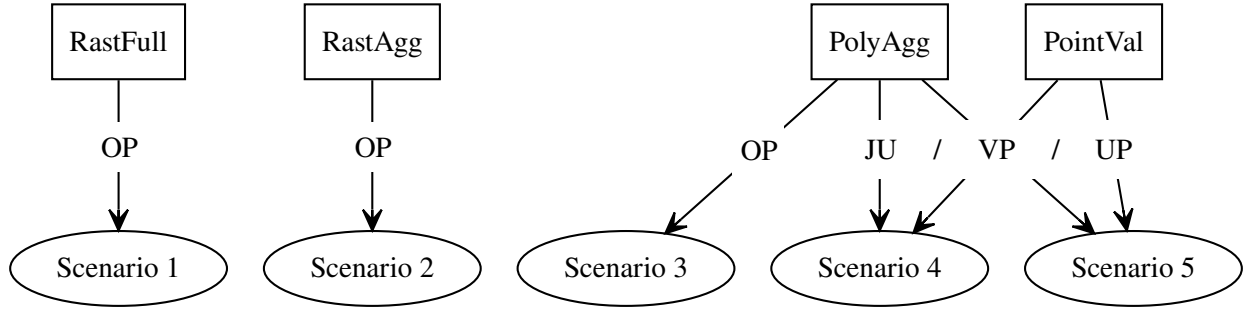


Figure 2: Flowchart of the simulation scenarios. The aggregation scenarios consist of: Raster at Full Resolution (RastFull), Raster Aggregation (RastAgg) and Polygon Aggregation (PolyAgg). The incomplete covariate field scenario is divided into two cases: Point Avalues (PointVal) and PolyAgg. OP: Observation Plugin, JU: Joint Uncertainty, VP: Value Plugin, UP: Uncertainty Plugin.

### 5.1.2 Rasterisation and Polygon Aggregation (PolyAgg) of Covariate Field

We compare the effect of the scales of raster aggregations in the covariate field. In Scenario 1), the covariate field is evaluated at the centre of each raster cell. This corresponds to satellite data that can be obtained everywhere and is treated as constant within each cell. For Scenario 2), we aggregate covariate raster in Scenario 1) into super-cells by a factor of 10. In this case, reconstruction of the continuous covariate field can be easily done in the same spirit as in Section 5.2.2. Under Scenario 3), we aggregate the covariate by averaging the rasters from Scenario 1) over administrative regional polygons. Rasterisation and polygon aggregation can be viewed as a limited set of observed field as the field is not fully observed, and we wish to quantify the accuracy and uncertainty from the resulting estimation procedures.

### 5.1.3 Incomplete Covariate Field for Point Values (PointVal)

Another incomplete measurement setting is pointwise measured covariates. More precisely, we observe a limited set of measured values of  $X(s)$  at a finite set of locations,  $\{s_i\}$ . We assume Gaussian additive noise for the observed covariate values and thus construct an extra layer in the Bayesian hierarchy to model the covariate field. Let  $z_i$  denote the observation of  $X(s_i)$  with

Gaussian additive noise term  $\epsilon_{x_i}$  so that,

$$z_i = X(s_i) + \epsilon_{x_i}, \quad \epsilon_{x_i} \sim \mathbf{N}(0, \sigma_{\epsilon_x}^2), \quad i = 1, \dots, n_z. \quad (22)$$

We randomly sample  $n_z = 777$  observed covariate points, with spatially uniform sampling density within each administrative polygon. We then add noises  $\sigma_{\epsilon_x}^2 = 0.1$  to these stratified samples (see Appendix C.4). This contrasts with the PolyAgg case where only the means of each polygon are used. Joint Uncertainty (JU), i.e. one stage approach, and two-stage approaches, Value Plugin (VP) and Uncertainty Plugin (UP), under the incomplete covariate field scenario will be explained in Sections 5.2.4 and 5.2.5.

#### 5.1.4 Nonlinear (NL) Misspecification

In order to test the robustness of models under the NL misspecification towards model mismatch. For the data generating mechanism, we transform covariate field via a nonlinear transformation  $f(\cdot)$ , i.e.  $\log \check{\lambda}(\cdot) = \check{\eta}(\cdot) = \beta_0 + \beta_x f[X(\cdot)] + u(\cdot)$ , where  $f[X(\cdot)] = b^{-1} \exp[aX(\cdot)] - c$ , and we set  $a = 3$ ,  $b = 9$  and  $c = 3$ . We then simulate point patterns  $\check{\mathcal{Y}}$  and aggregated count observations  $\check{\mathcal{N}}$  accordingly. This formulation results in  $\check{n} = 149$  simulated point observations. The resulting shift in the covariate and intensity field compared to the original simulation is shown in Figure 3.

## 5.2 Model and Method

### 5.2.1 Models with covariate Observation Plugin (OP)

For RastFull, RastAgg, and PolyAgg, we define the models with Observation Plugin (OP), the linear predictor

$$\eta(\cdot) = \beta_0 + \beta_x z(\cdot) + u(\cdot), \quad (23)$$

where each  $z(s)$  is the directly observed value of the covariate field at location  $s$ , and  $u(\cdot)$  is defined in equation (6) given *mesh* (*i*) from Section 5.1 and the PC prior setting (see Appendix C.5 and

refer to Fuglstad et al. (2019) for completeness). This gives six models in total to the point pattern and aggregated count observations under the aggregation scenarios, and the RastFull model with point pattern observation should serve as a benchmark.

### 5.2.2 Covariate Field Estimation Step for Polygon Aggregation (PolyAgg)

We can view aggregated data as incomplete observed field since we only observe some summary statistics, hopefully unbiased, over a region. Here we assume that the covariate is observed as averages,  $z_p$ , of the field over the aggregation sets  $\{A_p\}$  from Definition 2.2. With  $x(\cdot)$  denoting the complete covariate field, we consider

$$z_p = \frac{1}{|A_p|} \int_{A_p} x(\mathbf{s}) + \epsilon(\mathbf{s}) d\mathbf{s} = \frac{1}{|A_p|} \int_{A_p} x(\mathbf{s}) d\mathbf{s} + \underbrace{\frac{1}{|A_p|} \int_{A_p} \epsilon(\mathbf{s}) d\mathbf{s}}_{=: \epsilon_p}, \quad (24)$$

where  $\epsilon(\cdot)$  is a Gaussian field such that  $\{\epsilon_p\}$  are independent,  $\mathbf{N}(0, \sigma_{z_p|x(\cdot)}^2)$ . For simplicity, the simulation study will assume that all  $\sigma_{z_p|x(\cdot)}^2$  are equal to a common scaling parameter  $\sigma_z^2$ . This can easily be extended to a model where the variances are scaled by a function of  $|A_p|$ . The full covariate field  $x(\cdot)$  is modelled by prior model  $X(\cdot) \sim \text{GRF}(\mu_x(\cdot), \varrho_x(\cdot, \cdot))$ , leading to a posterior model  $X(\cdot)|\{z_p\} \sim \text{GRF}(\mu_{x|\{z_p\}}(\cdot), \varrho_{x|\{z_p\}}(\cdot, \cdot))$ .

In Section 5.2.5, this will plug in the posterior mean  $\hat{x}$  is equal to  $\mu_{x|\{z_p\}}$ . With the estimated linear predictor  $\eta(\cdot) = \beta_0 + \beta_x \hat{x}(\cdot) + u(\cdot)$ , where  $\hat{x}(\cdot) = \mathbb{E}(X(\cdot)|\{z_p\})$ , the point patterns and aggregated count observations follow  $\mathcal{Y}|\{z_p\} \sim \text{PoPr}(\exp[\eta(\cdot)])$ , and  $N_p|\{z_p\} \sim \text{Pois}\left(\int_{A_p} \exp[\eta(\mathbf{s})] d\mathbf{s}\right)$ , respectively, where  $\text{PoPr}$  denotes a Poisson Process. When aggregated value of  $x(\cdot)$  is needed, with  $X_j = |\Omega_j|^{-1} \int_{\Omega_j} X(\mathbf{s}) d\mathbf{s}$ , we estimate the covariate field via  $\mathbb{E}(X_j|\{z_p\}) = |\Omega_j|^{-1} \int_{\Omega_j} \hat{x}(\mathbf{s}) d\mathbf{s}$  on *mesh (i)* (see Appendix A.5 for mapper implementation and C.5 for PC prior details). It is worth noting that the smoothness of the predicted field depends on the mesh resolution, i.e. the volume of  $\Omega_j$ .

### 5.2.3 Covariate Field Estimation Step for Point Values (PointVal)

The estimation step for PointVal is similar to that for PolyAgg, apart from that we only observe the covariate field at point locations  $\mathbf{s}$  with added noises  $\{z(s_i) \mid i = 1, \dots, n_z\}$ . In Section 5.2.5, we will have  $\mathcal{Y} \mid \{z(s_i)\} \sim \text{PoPr}(\exp[\eta(\cdot)])$ , and  $N_p \mid \{z(s_i)\} \sim \text{Pois}\left(\int_{A_p} \exp[\eta(\mathbf{s})] d\mathbf{s}\right)$  respectively, and the linear predictor becomes  $\eta(\cdot) = \beta_0 + \beta_x \hat{x}(\cdot) + u(\cdot)$ , where  $\hat{x}(\cdot) = \mathbb{E}(X(\cdot) \mid \{z(s_i)\})$ .

### 5.2.4 One-stage Approach with Joint Uncertainty (JU) Method

The JU approach is to model the covariate field and all the parameters simultaneously,

$$\begin{cases} z(\cdot) = \hat{x}(\cdot) + \epsilon(\cdot), & \epsilon \sim \mathbf{N}(\mathbf{0}, \mathbf{Q}_\epsilon^{-1}), \\ \eta(\cdot) = \beta_0 + \tilde{\beta}_x \hat{x}(\cdot) + u(\cdot), & \tilde{\beta}_x \sim \text{Exp}(\cdot), \end{cases} \quad (25)$$

where  $\epsilon$  uses the same construction of  $\mathbf{u}$  in equation (6). This may bring identifiability or multi-modal concerns between  $\hat{x}(\cdot)$  and  $u(\cdot)$ . Another concern is convergence, which largely depends on whether the coefficient of  $\hat{x}(\cdot)$  can attain an opposite sign, resulting in a bimodal distribution. Nonetheless, as soon as it picks a "side" for  $\beta_x$ , the linearisation makes it unimodal. But different INLA runs, or with different initial values, might pick the opposite sign. However, with some direct observations of the field  $X(\cdot)$  (i.e.  $\{z_p\}$  or  $\{z(s_i)\}$ ), it is unlikely to happen. In practice, we often have prior information on whether positive or negative effect, this allows us to introduce an exponential prior distribution over the covariate coefficient. This is to avoid non-identifiability of the product of two Gaussian processes,  $\beta_x \hat{x}(\cdot)$ , that would have appeared if  $\beta_x$  had been given a Gaussian prior.

We estimate both the covariate field  $\hat{x}(\cdot)$  with *mesh (i)* and Matérn random field  $u(\cdot)$  with *mesh (ii)* from Section 5.1 for all the models under the incomplete covariate field scenarios respectively (See Section 5.1 for the mesh setup and Appendix C.5 for PC prior details). This significantly reduces the computation time by having a coarser *mesh (ii)* and improves the model accuracy by reducing the identifiability issue. The finer mesh resolution for the covariate field reduces the

uncertainty in the second stage. We can impose stronger PC priors by setting different sensible values for the prior parameters of both fields. Our Bayesian framework grants the uncertainty quantification for the estimated covariate field. However, it takes longer to fit a one-stage model than a two-stage model (see Appendix C.10) due to these confounding spatial terms.

### 5.2.5 Two-stage approaches with Value Plugin (VP) and Uncertainty Plugin (UP) Methods

In the estimation step of the two-stage approaches, we compute  $\hat{x}(\cdot)$  from Section 5.2.2 or 5.2.3. The Value Plugin (VP) method inputs the prediction into the full model as in equation (25), i.e.  $\eta(\cdot) = \beta_0 + \tilde{\beta}_x \hat{x}(\cdot) + \epsilon_y(\cdot)$ . The Uncertainty Plugin (UP) method incorporates  $\hat{x}(\cdot)$  and a spatial uncertainty term  $\epsilon_x(\cdot)$  in the second step,

$$\begin{cases} \eta(\cdot) = \beta_0 + \tilde{\beta}_x [\hat{x}(\cdot) + \epsilon_x(\cdot)] + \epsilon_y(\cdot), \\ \tilde{\beta}_x \sim \text{Exp}(\cdot), \epsilon_x(\cdot) \sim \mathbf{N}(\mathbf{0}, \hat{Q}_{\epsilon_x}^{-1}), \text{ and } \epsilon_y(\cdot) \sim \mathbf{N}(\mathbf{0}, Q_{\epsilon_y}^{-1}), \end{cases} \quad (26)$$

where  $\epsilon_x$  and  $\epsilon_y$  uses the same construction of  $\mathbf{u}$  in equation 6 and are modelled on *mesh (i)* and *mesh (ii)* from Section 5.1 respectively (see Appendix C.5 for PC prior details). From a modelling perspective, the noise  $\epsilon_x$  modelled as independent and identically distributed noise as a diagonal covariance matrix will run into identifiability issues. Hence, we use Type 0 generic model in INLA, which can specify the estimated precision matrix  $\hat{Q}_{\epsilon_x}$  accordingly (See Appendix C.7).

We predict the covariate field  $\hat{x}(\cdot)$  with the rasterised mesh elements ( $1.616 \text{ km} \times 1.616 \text{ km}$ ). We have precomputed the point locations to be evaluated at the beginning (see alternative method in Appendix C.7.1). The first step smooths out the covariate field even when the variance of noise  $\sigma_{\epsilon_x}^2$  is large. Unless there is discontinuity in the covariate field, or model mismatch, for example, omitting nonlinear effects, the first step would achieve a decent or a useful covariate model for the second step. Furthermore, we can always check the covariate field estimation before proceeding to the second step.

The VP method shifts the uncertainty  $\epsilon_x$  to the Matérn field noise  $\epsilon_y$ . Estimating only one

noise term significantly speeds up computation. The noise terms  $\epsilon_x$  and  $\epsilon_y$  in the latter two are inevitably confounded and require a sufficiently fine mesh to minimize nonlinearity within the mesh elements and avoid placing additional strain on computing the linearisation. The VP and UP are more computationally efficient than the JU approach. For the computation time of all the models, see Appendix C.10. We wish to make inference on  $\epsilon_x$  for uncertainty quantification. We incorporate covariate uncertainty in the second step as in equation (25). The uncertainty can be propagated via incorporating the precision matrix from the first step (see Appendix C.7).

### 5.2.6 Model Mismatch under Nonlinear (NL) Misspecification

We reuse the model frameworks, i.e. JU, UP and VP methods, specified in Sections 5.2.4 and 5.2.5, to adapt the nonlinear (NL) misspecification mentioned in Section 5.1.4. We aim to check the robustness of these frameworks for the mismatched nonlinear predictor.

### 5.2.7 Profile Likelihood for Uncertainty Propagation

To illustrate a one dimensional toy example, we can compare the model performances in the JU, VP and UP methods. The JU and UP methods have uncertainty propagation. Hence, we try to find the optimal values of  $\beta_0$ ,  $\beta_x$  and  $\epsilon_{x_i}$  according to the log-posterior density. We consider the extreme case where  $\{X(s_i) \mid i = 1, \dots, n_z\}$  are independent of each other, so that the estimation of  $X(s_i)$  cannot borrow strength from another location,  $s_i \neq s_{i'}$ . We formulate the observed covariate field as  $z(s_i) = X(s_i) + \epsilon_{x_i}$ ,  $X(s_i) \sim \mathbf{N}(0, \sigma_x^2)$ ,  $\epsilon_{x_i} \sim \mathbf{N}(0, \sigma_{\epsilon_x}^2)$ . We further assume that there are no missing observations, and we have

$$\begin{cases} X(s_i)|z(s_i) & \sim \mathbf{N}(\hat{x}_i, \sigma_{x_i|z(s_i)}^2), \\ \mathcal{Y}|\hat{x}_i : \eta(s_i) & = \beta_0 + \beta_x(\hat{x}_i + \epsilon_{x_i}) + \epsilon_{y_i}, \quad \epsilon_{x_i} \sim \mathbf{N}(0, \sigma_{x_i|z(s_i)}^2). \end{cases}$$

We aim to check the asymptotic behavior when  $n_z \rightarrow \infty$ ,

$$\mathfrak{p} := \log \mathbb{P}[(\beta_0, \beta_x, \epsilon_{x_i}) | \{X(s_i)\}]$$

$$= \sum_i (-e^{\eta_i} + \eta_i y_i) - \frac{1}{2} \left[ \left( \frac{\beta_0^2}{\sigma_{\beta_0}} \right)^2 + \left( \frac{\beta_x}{\sigma_{\beta_x}} \right)^2 + \sum_{i=1}^{n_z} \left( \frac{\epsilon_{x_i}}{\sigma_{x_i|z(s_i)}} \right)^2 \right]. \quad (27)$$

We have not found a closed form expression for the optimal value of the derivative from equation (27) (see Section C.8.1 in Appendix C.8). For this reason, we instead use numerical optimisation to find the optimal  $(\beta_0, \beta_x, \epsilon_{x_i})$ . Since our focus is on  $\beta_x$ , we use the profile likelihood to optimise  $\beta_x$  with  $n_z \in \{2, 4, 8, 16, 32, 64, 128, 256\}$ ,  $\arg \max_{\beta_x} (\arg \max_{(\beta_0, \epsilon_x)} (\mathbf{p}))$ .

The plots of the log-posterior density against  $\beta_x$  in Appendix C.8.2 show that all the profile posterior modes converge to the true value of  $\beta_x$  as  $n_z$  increases. Although the plots for UP method in Figure 19 in Appendix C.8.2, the profile likelihood is not a strictly convex function though the global maximum is distinct from the local maximum as  $\beta_x$  approaching to infinity. It might pose problem for the optimisation algorithm and one should be careful about the initial starting points. However, we did not encounter any issues in our simulation (see Sections 6.3 and 6.4).

## 6 Results

A prediction score  $S(F, \lambda)$  evaluates some measure of closeness between a pointwise estimate identified by a predictive distribution  $F$ , and an observed value  $\lambda$ . We define the expectation of a score as  $S(F, G) = \mathbb{E}_{\lambda \sim G}[S(F, \lambda)]$ . A negatively oriented score (i.e. the lower the score, the better) is proper if it fulfills  $S(F, G) \geq S(G, G)$ . This implies that any predictive distributions with a higher or lower prediction uncertainty, other than the true one, will not lead to a better score on average (Gneiting and Raftery, 2007). The Squared Error (SE),  $S_{\text{SE}}(F, \lambda) = (\lambda - \hat{\lambda}_F)^2$ , and Dawid-Sebastiani (DS) score,  $S_{\text{DS}}(F, \lambda) = \sigma_F^2(\hat{\lambda})^{-1}(\lambda - \hat{\lambda}_F)^2 + \log[\sigma_F^2(\hat{\lambda})]$ , are common proper scoring rules (Dawid and Sebastiani, 1999). The Mean Squared Error (MSE) and Mean Dawid-Sebastiani (MDS) score for the points across a space are defined as  $S(\{F_i\}, \{\lambda_i\}) = n^{-1} \sum_{i=1}^n S(F_i, \lambda_i)$ .

We compare the prediction accuracy via the proper scoring rules, namely the SE and DS scores for the intensity field  $\lambda$ . The lower the score, the better the model is. We evaluate the mean scores for the intensity field  $\lambda$  pointwise at  $n = 56,809$  evenly distributed point locations across Nepal.

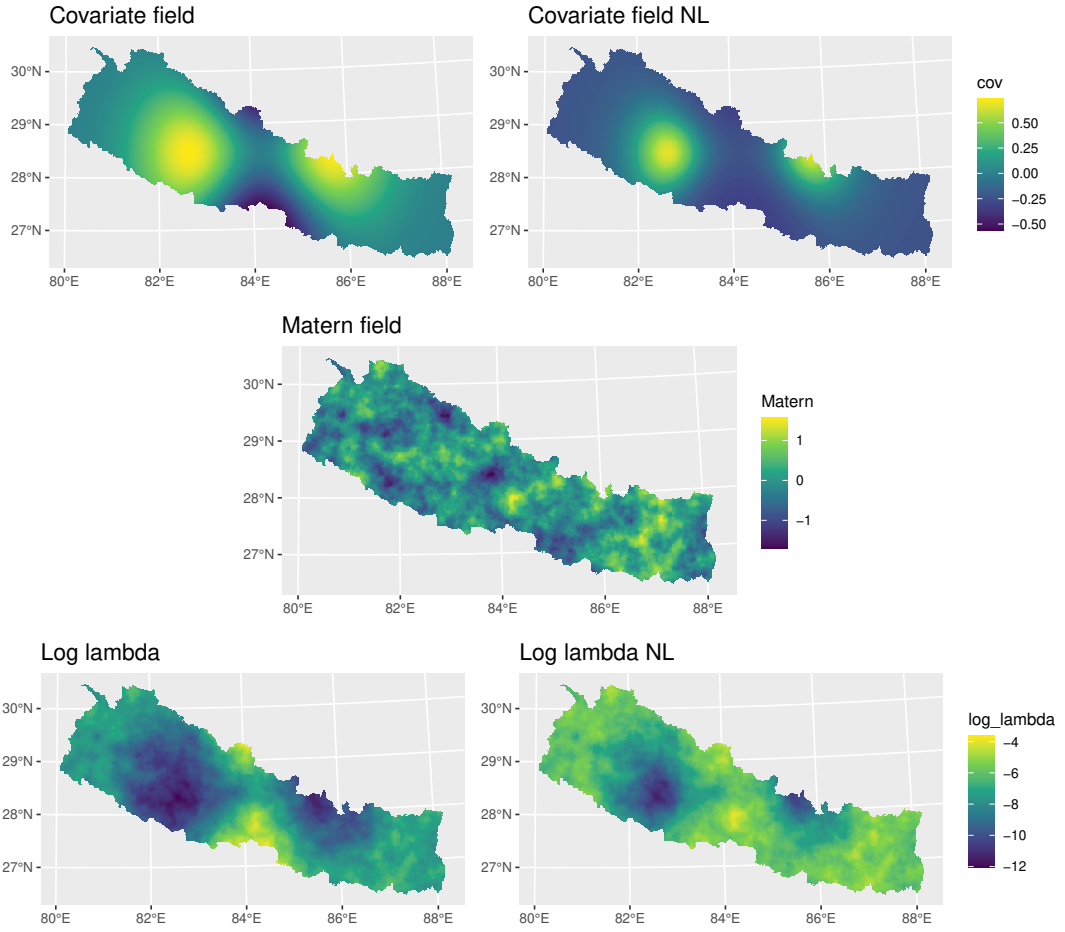


Figure 3: Covariate fields  $X(\cdot)$  and  $f(X(\cdot))$  (top row), Gaussian Matérn field  $u(s)$  (middle) and the intensity fields  $\log(\lambda)$  and  $\log(\check{\lambda})$  (bottom row); where top two and bottom two share the same legend respectively. NL: Nonlinear misspecification.

We compute the SE and DS scores of the intensity field for the simulation models because the true simulated intensity field allows us to compare across point and aggregated count observation models.

## 6.1 Intensity Estimation under Aggregation Scenarios

We compare the performances of the RastFull, RastAgg and PolyAgg OP models for point patterns and aggregated count observations here. In Table 1, the point pattern models outperform the corresponding aggregated count models in both scores. The RastFull point pattern models achieves the best scores. As the aggregation scale and irregularity increase, the scores worsen across each

observation category. The MDS scores for the RastFull and RastAgg models are similar due to well-justified variances.

The score distributions are shown in Figures 4 and 5. The plots retain a piecewise linear pattern for both the RastAgg and PolyAgg models. In Figure 4, most SEs are concentrated in the central region, where the majority of observed points are located. In contrast, the aggregated count models exhibit better DS scores in the smaller provinces due to averaging effects. This observation leads us to consider projecting point observations onto mesh nodes, which will be discussed in Section 7.1. Despite this, the overall MDS scores remain lower for point pattern models. Figure 5 shows that the DS plots for aggregated count models display more consistent variances compared to point pattern models.

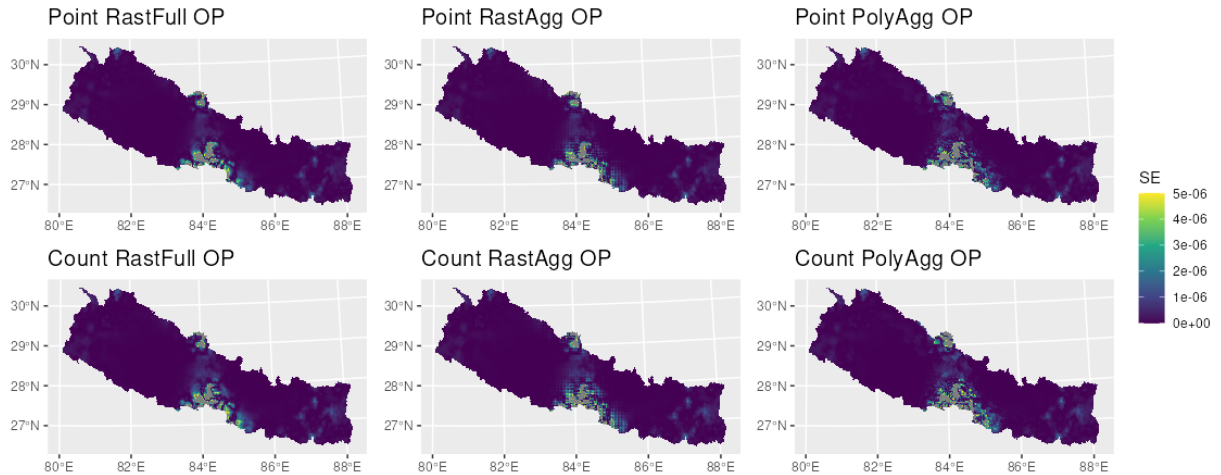


Figure 4: Squared Error (SE) for the intensity field  $\lambda$  across the models under aggregation scenarios (truncated at  $5 \times 10^{-6}$ ). Point Pattern (top row) and Aggregated Count (bottom row) observation models.  $\bar{\lambda} = 2.456 \times 10^{-3}$ . RastFull: Raster at Full Resolution, RastAgg: Aggregated Raster, PolyAgg: Polygon Aggregations, OP: Observation Plugin.

## 6.2 Covariate Estimation under Incomplete Covariate Field Scenario

The PolyAgg and PointVal models are not directly comparable under incomplete covariate field scenario (see Table 4 in Appendix C.9) as the latter includes Gaussian additive noise term  $\epsilon_{x_i}$  from equation (22), while the former does not. However, this noise term negatively impacts the scores

though stratified sampling for each polygon provides more precise point locations of the covariate field. This may partly explain why the PolyAgg models achieve better scores than PointVal models in predicting the covariate field. Under both PolyAgg and PointVal categories, the JU models outperform the VP and UP models. This suggests that jointly modelling the intensity and covariate fields offers more informative predictions than modeling them separately. For the PointVal category, the point pattern JU model slightly outperforms the corresponding aggregated count model in both scores.

Consequently, we will see how the predicted covariate fields may have an knock-on effect on the intensity field prediction in the following subsection given the covariate field is only part of the story to predict the intensity field. It is worth mentioning that there are visible hotspots in DS plots (see Appendix C.9 for DS and other plots) due to lower noises at where the observed points are.

### 6.3 Intensity Estimation under Incomplete Covariate Field Scenario

We compare the performances of the PolyAgg and PointVal models with OP, JU, VP and UP methods for point pattern and aggregated count observations here. In Table 1, in terms of MSE

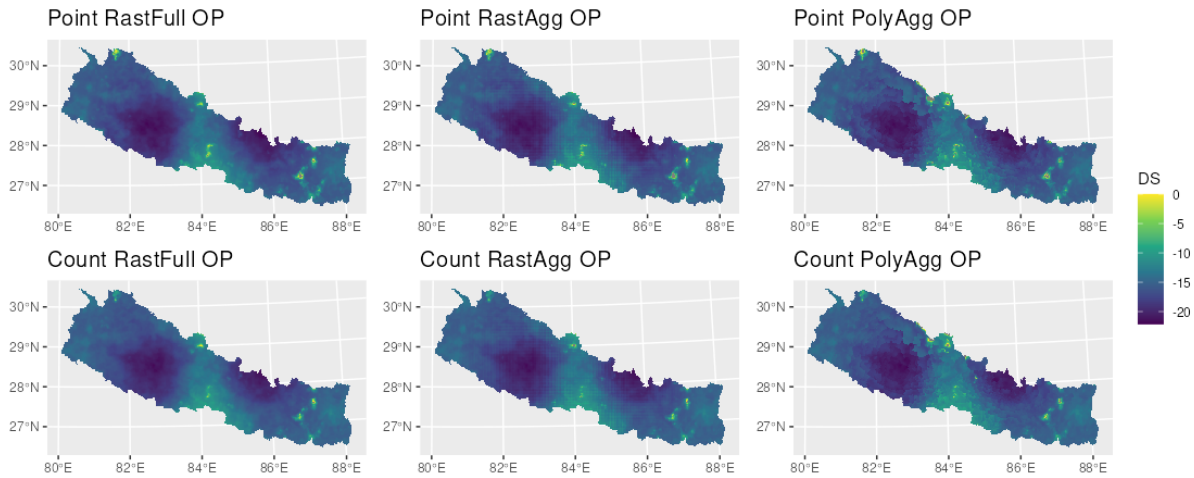


Figure 5: Dawid-Sebastiani (DS) score for the intensity field  $\lambda$  across the models under aggregation scenarios (truncated at 0). Point Pattern (top row) and Aggregated Count (bottom row) observation models. RastFull: Raster at Full Resolution, RastAgg: Aggregated Raster, PolyAgg: Polygon Aggregations, OP: Observation Plugin.

scores for the intensity field estimation under PolyAgg, the JU and UP models perform better than the OP model while the VP models perform worse. Hence, these results underscore the critical role of uncertainty quantification in intensity field prediction and downscaling the covariate field may not improve the model. The JU models perform better than the UP models in terms of MSE score and very close in terms of MDS score. This suggests that the joint estimation provides a slight edge for the robustness against the additional noises. However, the MDS scores of the JU and UP models are similar to the OP models, which might be due to the extra uncertainty introduced via the covariate field estimation (see discussion in Section 7.1).

The performance of PolyAgg models surpasses than that of the corresponding PointVal models due to the additional noises in the PointVal covariate observations, as in the covariate field estimation in the previous subsection. Across all PolyAgg and PointVal categories, the JU models achieve the highest scores or come very close. Despite the under-performance in estimating the predicted covariate field in both PolyAgg and PointVal, the UP models perform reasonably well. In Figure 6, the areas with large SE (where high SE are truncated in grey for visualisation) for the VP models are larger compared to the JU and UP models in the regions with dense observations. The DS plots in Figure 7 show similar effects and the JU and UP models perform better in regions with fewer observations. Hence, this suggests the scores are consistent across Nepal.

Overall, the PolyAgg and PointVal models with the JU and UP methods show significant improvements, compared to the piecewise linear approach in the PolyAgg model in the previous subsection. The hotspots observed in DS plots for predicting the covariate field in the previous subsection are no longer observed in the DS plots for predicting the intensity field. This is likely because the Matérn field compensates for the under-performance at those locations.

## 6.4 Intensity Estimation under Nonlinear (NL) Misspecification

We compare the performances of the PolyAgg and PointVal models with JU, VP and UP methods for point pattern and aggregated count observations under NL here. In Table 2, the JU and UP models clearly outperform the VP models due to the uncertainty propagation. The scores also

are the measures of the robustness of these models under the NL misspecification towards model misspecification. The linearisation and Matérn noise term  $\epsilon_y$  are not flexible enough for the VP method to account for the model misspecification. Indeed, both JU and UP methods are better than the VP one in terms of MSE and, particularly, MDS scores. This is consistent with both the SE and DS plots in Figures 8 and 9. This implies that the uncertainty propagation is better explained in terms of variance thanks to the extra noise term in the UP methods.

Indeed, the VP method under NL misspecification is not as bad as expected in MSE scores because the Matérn field term  $u(s)$  compensates for the model misspecification. Empirically,

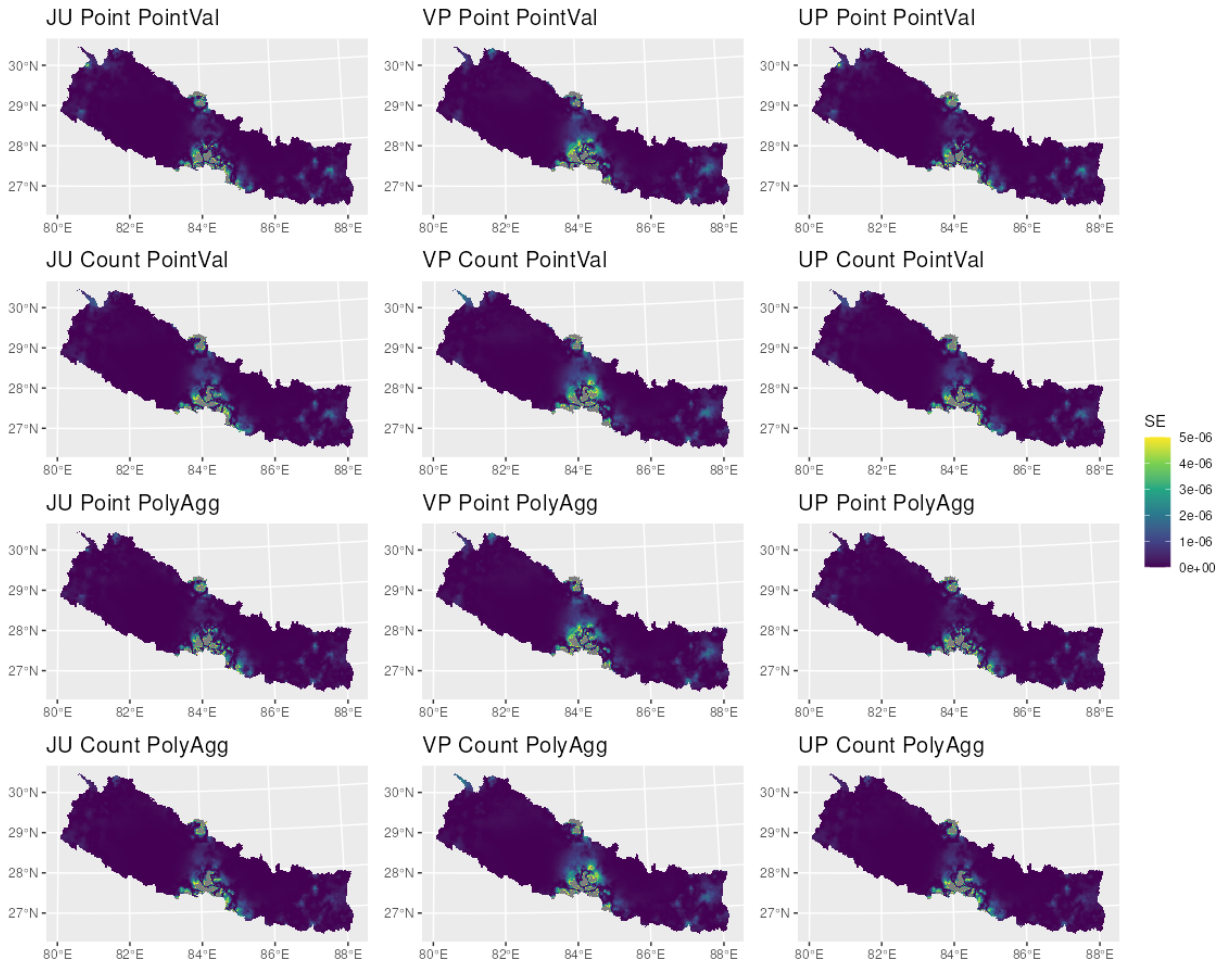


Figure 6: Squared Error (SE) for the intensity field  $\lambda$  across the models under incomplete covariate field scenario (truncated at  $5 \times 10^{-6}$ ). JU: Joint Uncertainty, VP: Value Plugin, UP: Uncertainty Plugin, Point: Point Pattern, Count: Aggregated Count, PolyAgg: Polygon Aggregation, PointVal: Point Values.  $\bar{\lambda} = 2.456 \times 10^{-3}$ .

the JU and UP methods are more robust than the VP method. Again, we observe the PolyAgg models are better than the corresponding PointVal ones due to the additional noises in the observed covariate field. Surprisingly, the aggregated count models are better than point pattern ones in both scores. In Figure 9, the DS plots show the spread of the truncated area more clearly. This finding leads us to consider the projection of point observations into weights on mesh nodes to better explain the variance (see Section 7.1 for discussion).

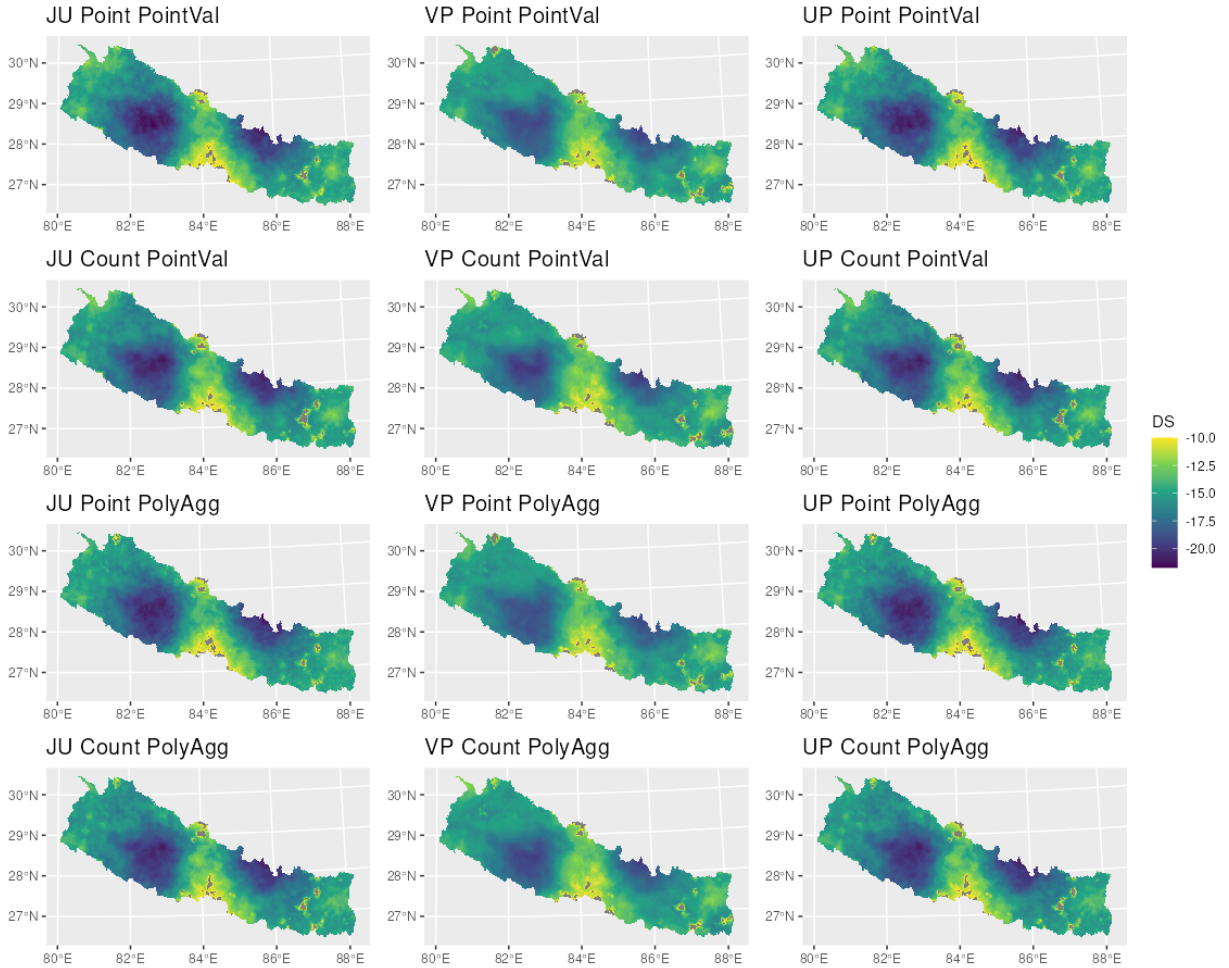


Figure 7: Dawid-Sebastiani (DS) score for the intensity field  $\lambda$  across the models under incomplete covariate field scenario (truncated at  $-10$ ). JU: Joint Uncertainty, VP: Value Plugin, UP: Uncertainty Plugin, Point: Point Pattern, Count: Aggregated Count, PolyAgg: Polygon Aggregation, PointVal: Point Values.

## 7 Conclusion and Discussion

Aggregated data is common, and aligning data geometry through aggregation is a typical approach. Here, we summarise key findings, discuss implications, and highlight study limitations, future research directions, and connections to INLA extension packages.

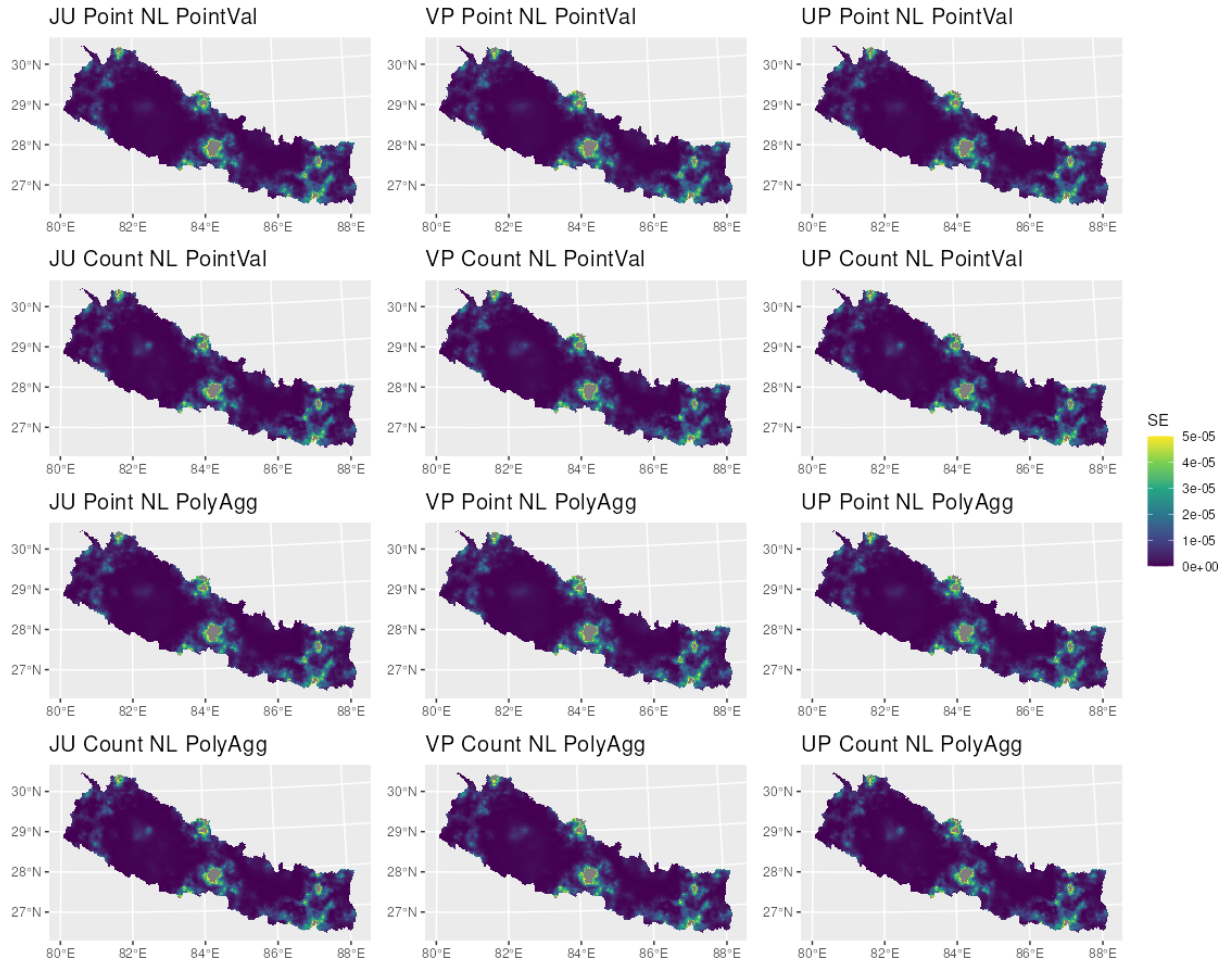


Figure 8: Squared Error (SE) for the intensity field  $\lambda$  across the misspecified models under incomplete covariate field scenario (truncated at  $5 \times 10^{-5}$ ). JU: Joint Uncertainty, VP: Value Plugin, UP: Uncertainty Plugin, Point: Point Pattern, Count: Aggregated Count, NL: Nonlinear misspecification, PolyAgg: Polygon Aggregation, PointVal: Point Values.  $\bar{\lambda} = 2.456 \times 10^{-3}$ .

## 7.1 Versatile Framework for Aggregation

We showed that aggregated count observation and covariate data can introduce bias and degrade model performance, in terms of Mean Squared Error (MSE) and Mean Dawid-Sebastiani (MDS) scores. We illustrated a versatile disaggregation framework with uncertainty quantification leveraging mesh-based modelling approach for aggregated data with a various examples. We demonstrated its use in modelling point and count observation data with point, raster, or polygon covariates to make continuous intensity field prediction. Under aggregation scenarios, the model with

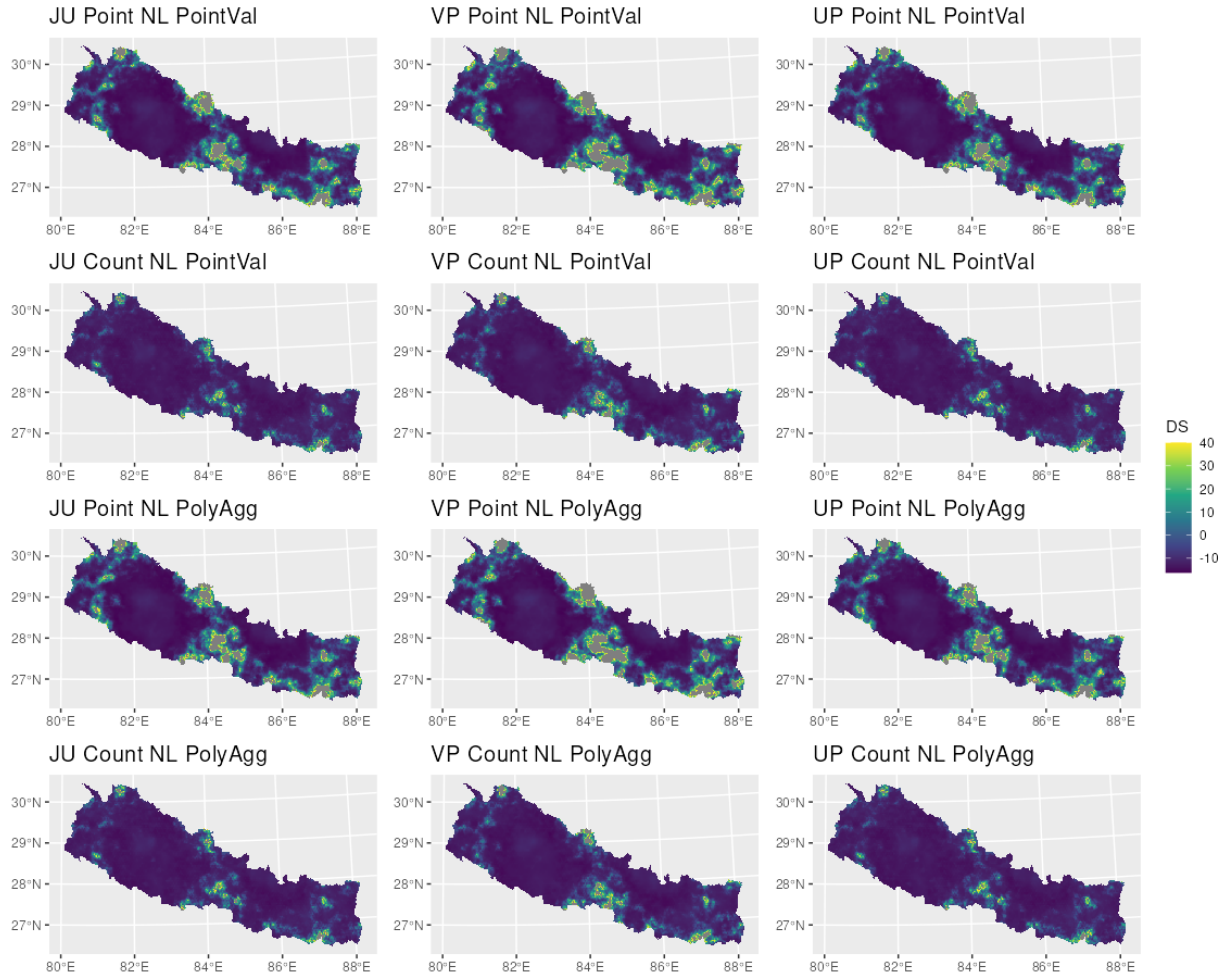


Figure 9: Dawid-Sebastiani (DS) score for the intensity field  $\lambda$  across the misspecified models under incomplete covariate field scenario (truncated at 40). JU: Joint Uncertainty, VP: Value Plugin, UP: Uncertainty Plugin, Point: Point Pattern, Count: Aggregated Count, NL: Nonlinear misspecification, PolyAgg: Polygon Aggregation, PointVal: Point Values.

point patterns ( $\mathcal{Y}$ ), covariate Raster at Full Resolution (RastFull) performed the best, followed by covariate Raster Aggregation (RastAgg). The traditional model with aggregated count ( $\mathcal{N}$ ), Polygon Aggregated (PolyAgg) covariate, performed the worst and took longer computation time. Therefore, preserving point location information is crucial in spatial statistics and data aggregation should be avoided. We presented that appropriate uncertainty propagation enhances models' performance and robustness. Under both incomplete covariate field scenario and Nonlinear (NL) model misspecification , both the Joint Uncertainty (JU) and Uncertainty Plugin (UP) models outperformed the traditional Value Plugin (VP) model. The UP models exhibited faster computational efficiency and better control over the predicted covariate field for easier validation with possible new data. More importantly, knowing the exact link predictor to model the data a priori is unlikely. This approach provides flexibility for handling uncertainty and model misspecification.

## 7.2 Limitations and Future Research Directions

To streamline the paper's focus, we did not explore different precision matrix choices for the uncertainty propagation (see Section 5.2.5 and Appendix C.7) to enhance the uncertainty propagation. The number of iterations needed for convergence is unpredictable and depends on factors such as tolerance levels, line search direction, mode assessment in INLA, the data, and the model specification (see convergence diagnostics in Appendix D). Further research is required to determine the optimal settings. Implementing automatic differentiation can help accelerate computation (see Carpenter et al. (2015)).

Observations, including those related to landslides and other fields, are manually registered, introducing inherent uncertainties regarding their exact spatial and temporal accuracy. To address this, we can split the observed point information and project it onto nearby mesh nodes with partial weights so that we introduce uncertainty in a manner akin to aggregated count models but with more controlled adjustments. This approach helps mitigate the covariate field uncertainties caused by model misspecification.

The flexibility, *degree of freedom (DoF)*, of the estimated intensity field is determined by the

mesh resolution. We have to respect the degrees of freedom to all spatial random fields to ensure a bounded likelihood approximation. In particular, this applies to Matérn effects defined on triangulation meshes and uncertainty propagation fields for high resolution covariates. If too few integration points were to be used, the nonlinear integral approximations would not sufficiently bound the likelihood. We solve this by ensuring the integration scheme respects both the mesh and covariate resolutions. Apart from the linearisation, the Matérn random field in our models indeed accounts for the data misalignment, which can be controlled under stricter PC priors.

The linearisation becomes more stable with an increase in integration points. A finer mesh by subdividing the elements would stabilise the linearisation further (see Appendix B.5). There is a fundamental difference between increasing the integration points within each element and subdivision of elements. The former adds more equally weighted points, while the latter creates more piecewise linear mesh elements to account for the nonlinearity. In the future, we will explore alternative integration schemes, such as Simpson’s rule or Gaussian quadrature.

### 7.3 Connection to INLA Extension Packages

In various applications, including landslides, there is often uncertainty regarding the exact locations, as these are determined manually. In some instances, we cannot revert to the original trigger location over time. Hence, contour map can be useful in assessing the joint uncertainty excursion sets via `excursions` package (Bolin and Lindgren, 2017). These maps add an extra dimension for evaluating contour credible risk regions and help propagate uncertainty arising from the aggregation. Assuming stationarity can be quite restrictive. Extending the models to nonstationary and anisotropic scenarios would be complex, as it requires understanding how meshing and linearisation adapt to underlying unknown nonstationary and anisotropic features (Llamazares-Elias et al., 2024). One potential workaround is to ensure that the mesh resolution is sufficiently fine to accommodate the shortest range of the anisotropic field. Another extension is to consider the nonseparable class of models using the `INLAspacetime` package (Lindgren et al., 2020). The linearisation would work the same for the diffusion process. In principal, a drift term can be incor-

porated into the Matérn field to account for the nonseparability. However, a caveat is that more data would be needed to accurately estimate these models. Additionally, we aim to connect our aggregation framework to the metric graph models in the `MetricGraph` package (Bolin et al., 2024). This linkage is significant as it integrates the aggregation framework with river and road networks. Such networks can be valuable for modelling landslide risk, extending beyond road construction and maintenance planning to include evacuation strategies in the event of an earthquake. The river network can help model flood risk. Furthermore, slope unit delineation primarily depends on the region's topography and geology, shaped by watershed lines.

## Tables

**Abbreviations:** Cov.: Covariate Observation, Obs.: Observation,  $\bar{\lambda}(\cdot)$ : Mean of Intensity Field,  $\check{\bar{\lambda}}$ : Mean of Intensity Field under Nonlinear misspecification (NL), RastFull: Raster at Full Resolution, RastAgg: Aggregated Raster, PolyAgg: Polygon Aggregations, PointVal: Point Values, OP: Observation Plugin, JU: Joint Uncertainty, VP: Value Plugin, UP: Uncertainty Plugin,  $\mathcal{Y}$ : Point Pattern,  $\mathcal{N}$ : Aggregated Count,  $\check{\mathcal{Y}}$ : Point Pattern under Nonlinear misspecification (NL),  $\check{\mathcal{N}}$ : Aggregated Count under Nonlinear misspecification (NL).

Cov.	Obs.	Method	MSE	MDS	$\bar{\lambda}$
RastFull	$\mathcal{Y}$	OP	<b><math>4.226 \times 10^{-7}</math></b>	<b><math>-1.615 \times 10^1</math></b>	$8.915 \times 10^{-4}$
RastAgg			$4.559 \times 10^{-7}$	$-1.610 \times 10^1$	
RastFull	$\mathcal{N}$	OP	<b><math>4.339 \times 10^{-7}</math></b>	<b><math>-1.593 \times 10^1</math></b>	
RastAgg			$4.706 \times 10^{-7}$	$-1.591 \times 10^1$	
PolyAgg	$\mathcal{Y}$	OP	$5.523 \times 10^{-7}$	<b><math>-1.586 \times 10^1</math></b>	
		JU	<b><math>4.090 \times 10^{-7}</math></b>	$-1.573 \times 10^1$	
		VP	$5.946 \times 10^{-7}$	$-1.521 \times 10^1$	
		UP	$4.092 \times 10^{-7}$	$-1.574 \times 10^1$	
	$\mathcal{N}$	OP	$5.995 \times 10^{-7}$	<b><math>-1.579 \times 10^1</math></b>	
		JU	$4.541 \times 10^{-7}$	$-1.578 \times 10^1$	
		VP	$7.228 \times 10^{-7}$	$-1.517 \times 10^1$	
		UP	<b><math>4.540 \times 10^{-7}</math></b>	$-1.578 \times 10^1$	
PointVal	$\mathcal{Y}$	JU	<b><math>4.400 \times 10^{-7}</math></b>	<b><math>-1.568 \times 10^1</math></b>	$2.456 \times 10^{-3}$
		VP	$6.019 \times 10^{-7}$	$-1.522 \times 10^1$	
		UP	$4.933 \times 10^{-7}$	$-1.560 \times 10^1$	
	$\mathcal{N}$	JU	<b><math>4.690 \times 10^{-7}</math></b>	<b><math>-1.568 \times 10^1</math></b>	
		VP	$7.308 \times 10^{-7}$	$-1.517 \times 10^1$	
		UP	$5.354 \times 10^{-7}$	$-1.561 \times 10^1$	

Table 1: Table of the Mean Squared Error (MSE) and Mean Dawid-Sebastiani (MDS) scores for the intensity field  $\lambda$  across the models under the aggregation and incomplete covariate field scenarios.

Cov.	Obs.	Method	MSE	MDS	$\bar{\lambda}$
PolyAgg	$\check{\mathcal{Y}}$	JU	$5.952 \times 10^{-6}$	-2.690	$2.456 \times 10^{-3}$
		VP	$6.150 \times 10^{-6}$	1.354	
		UP	<b><math>5.948 \times 10^{-6}</math></b>	<b><math>-2.901</math></b>	
	$\check{\mathcal{N}}$	JU	$5.401 \times 10^{-6}$	-9.667	
		VP	$5.682 \times 10^{-6}$	-8.125	
		UP	<b><math>5.379 \times 10^{-6}</math></b>	<b><math>-9.797</math></b>	
PointVal	$\check{\mathcal{Y}}$	JU	<b><math>5.962 \times 10^{-6}</math></b>	-2.124	$2.456 \times 10^{-3}$
		VP	$6.152 \times 10^{-6}$	1.504	
		UP	$5.964 \times 10^{-6}$	<b><math>-2.170</math></b>	
	$\check{\mathcal{N}}$	JU	$5.398 \times 10^{-6}$	-9.723	
		VP	$5.702 \times 10^{-6}$	-7.940	
		UP	<b><math>5.379 \times 10^{-6}</math></b>	<b><math>-9.797</math></b>	

Table 2: Table of the Mean Squared Error (MSE) and Mean Dawid-Sebastiani (MDS) scores for the intensity field  $\lambda$  across the models under the Nonlinear misspecification (NL).

## Supplementary Information

# Appendices

## A Derivations related to Poisson Point and Count Processes

Here, we provide the derivations and implementations mentioned in Section 2.

### A.1 Derivation of the likelihood function

Here, we provide the derivation of the likelihood function for the Poisson point process specified in Definition 2.3. Let  $\mathcal{Y} = \{y_1, \dots, y_{N(\Omega)}\}$  be some observed point pattern, where  $N(\cdot)$  is the random count measure on a bounded domain  $\Omega \subset \mathbb{R}^d, d \in \mathbb{N}$ , given some intensity function  $\lambda$  that is defined on every Borel measurable set  $A \subseteq \Omega$ . This point process is locally finite such that  $N(A) < \infty$  for all  $A$ ; this implies the intensity functions are locally integrable (see Baddeley et al. (2007) for details). The likelihood function of the observed point pattern can be specified given the intensity function  $\lambda$  and  $N(\Omega) = n$ ,

$$p_Y(\mathcal{Y}, N(\Omega) = n | \lambda) := \mathbb{P}(N(\Omega) = n | \lambda) \cdot p(\{y_1, \dots, y_n\} | \lambda, N(\Omega) = n),$$

where  $p(\{y_1, \dots, y_n\} | \lambda, N(\Omega) = n)$  is the joint density function of the observations. Since event locations are conditional independent,

$$\begin{aligned} p_Y(\mathcal{Y}, N(\Omega) = n | \lambda) &= \mathbb{P}(N(\Omega) = n | \lambda) \prod_{i=1}^n p(y_i | \lambda, N(\Omega) = n) \\ &= e^{-\Lambda(\Omega)} \frac{[\Lambda(\Omega)]^n}{n!} \prod_{i=1}^n \frac{\lambda(y_i)}{\Lambda(\Omega)} \\ &= \frac{e^{-\Lambda(\Omega)}}{n!} \prod_{i=1}^n \lambda(y_i). \end{aligned}$$

## A.2 Derivations of first-order Taylor approximation

Derivations of  $\bar{M}_j(\mathbf{u})$  and  $\bar{m}_j(\mathbf{u})$  in equations (12) and (13) from Section 2.1 are shown here.

Assuming  $\lambda$  is log-linear,

$$\begin{aligned} - \int_{\Omega} \lambda(\mathbf{s}) d\mathbf{s} &= - \sum_{j=1}^J \int_{\Omega_j} \lambda(\mathbf{s}) d\mathbf{s} \\ &= - \sum_{j=1}^J \int_{\Omega_j} \exp[\underbrace{\log \lambda(\mathbf{s})}_{\approx \eta(\mathbf{s})}] d\mathbf{s} \end{aligned} \quad (\text{A1})$$

$$\neq - \sum_{j=1}^J \exp \left( \int_{\Omega_j} \eta(\mathbf{s}) d\mathbf{s} \right) \quad (\text{A2})$$

A common problem shown in equation (A2) is that the observed point locations are lost when being aggregated with respect to the subset  $\Omega_j$  to overcome the data misalignment. Mathematically speaking, the exponential function and the integral function are not commutative. This can lead to wrong estimation of intensity function thus the effects of the covariates.

Following equation (A1),

$$\begin{aligned} & - \sum_{j=1}^J \int_{\Omega_j} \exp[\eta(\mathbf{s})] d\mathbf{s} \\ &= - \sum_{j=1}^J \exp \left[ \underbrace{\log \left( \int_{\Omega_j} \exp[\eta(\mathbf{s})] d\mathbf{s} \right)}_{=: M_j(\mathbf{u}) \approx m_j(\mathbf{u}_*) + \mathbf{J}^{(j)}(\mathbf{u}_*)^\top(\mathbf{u} - \mathbf{u}_*) =: \bar{M}_j(\mathbf{u})} \right] \\ &\approx - \sum_{j=1}^J \sum_{k=1}^{n_j} w_{jk} \exp(\eta(\mathbf{s}_{jk})) \\ &= - \sum_{j=1}^J \exp \left[ \underbrace{\log \left( \sum_{k=1}^{n_j} w_{jk} \exp[\eta(\mathbf{s}_{jk})] \right)}_{\approx m_j(\mathbf{u}) \approx m_j(\mathbf{u}_*) + \mathbf{J}^{(j)}(\mathbf{u}_*)^\top(\mathbf{u} - \mathbf{u}_*) =: \bar{m}_j(\mathbf{u})} \right] \end{aligned}$$

It is worth noting that  $w_{jk}$  do not have unique solutions. Thus  $\sum_{k=1}^{n_j} w_{jk}$  do not have to sum up to 1 because these account for the contributions of the integration points towards an integral via a

stable integration scheme (see details in Appendix B.5).

When  $J \rightarrow \infty$ , then the function is closer to a piecewise linear function across  $\Omega_j$  as  $\Omega_j \rightarrow 0$ , thus converges into the true field.

### A.3 Continuous Linearisation Case

Here, we provide the proof for the continuous linearisation case mentioned in Theorem 2.1. We assume the following:

1. The function  $M_j(\mathbf{u})$  is twice differentiable at some points  $\mathbf{u}_* \in \mathbb{R}$ ; and
2. The linear predictor  $\eta(\cdot) = b + \mathbf{A}\mathbf{u}$  is an affine function of  $\mathbf{u}$ .

Given the subset  $\Omega_j$  does not depend on  $\mathbf{u}$  and by Leibniz's integral rule, the terms related to  $\partial\Omega_j$  disappear. we spell out the derivation for the first and second-order partial derivatives of the  $j$ -th term with respect to the  $l$  and  $l'$ , for  $l, l' = 1, \dots, L$ ,

$$\frac{\partial m_j}{\partial u_l} = \frac{\int_{\Omega_j} \lambda(s) \nabla_u \eta(s) \, ds}{\int_{\Omega_j} \lambda(s) \, ds} < \infty, \quad (\text{A3})$$

$$\begin{aligned} \frac{\partial^2 m_j}{\partial u_l \partial u_{l'}} &= \frac{\partial}{\partial u_{l'}} \frac{\int_{\Omega_j} \lambda(s) \nabla_u \eta(s) \, ds}{\int_{\Omega_j} \lambda(s) \, ds} \\ &= \frac{\int_{\Omega_j} \lambda(s) \nabla_u \eta(s) \nabla_u^\top \eta(s) \, ds}{\int_{\Omega_j} \lambda(s) \, ds} - \frac{\int_{\Omega_j} \lambda(s) \nabla_u \eta(s) \, ds}{\int_{\Omega_j} \lambda(s) \, ds} \cdot \frac{\int_{\Omega_j} \lambda(s) \nabla_u^\top \eta(s) \, ds}{\int_{\Omega_j} \lambda(s) \, ds} < \infty. \end{aligned} \quad (\text{A4})$$

Hence, equations (A3) and (A4) are bounded because  $\int_{\Omega_j} \lambda(s) \, ds$  is bounded by definition and  $\nabla_u \eta(\cdot) = \mathbf{A}$  is bounded. We interpret equation (A4) as the difference between the product of gradient average and a product of average gradient. Recall that the predictor  $\eta(\cdot)$  comprises of covariate contribution here; without such contribution, there might be identifiability issue.

The subsets can be specified as `block` argument with `ibm_eval` function in the `inlabru` package.

```
R> ibm_eval(..., input = list(block = .block, weights = weight))
```

## A.4 Discretised Linearisation Case

Here, we provide the proof for the discretised linearisation case mentioned in Theorem 2.1. We assume the following:

1. The function  $m_j(\mathbf{u})$  are twice differentiable at some points  $\mathbf{u}_* \in \mathbb{R}$ ;
2. The linear predictor  $\eta(\cdot) = b + \mathbf{A}\mathbf{u}$  is an affine function of  $\mathbf{u}$ .

Given the subset  $\Omega_j$  does not depend on  $\mathbf{u}$  and by Leibniz's integral rule, the terms related to  $\partial\Omega_j$  disappear, we spell out the derivation for the first and second-order partial derivatives of the  $j$ -th term with respect to the  $l$  and  $l'$  for  $l, l' = 1, \dots, L$ .

We denote the following vectors and matrices, for  $j = 1, \dots, J$ , and  $k = 1, \dots, n_j$ ,

$$\begin{aligned} \mathbf{s}_j &:= \begin{bmatrix} \vdots \\ \mathbf{s}_{jk} \\ \vdots \end{bmatrix}, \\ \eta_{jk} = \eta(\mathbf{s}_j; \mathbf{u}) &:= \begin{bmatrix} \vdots \\ \eta(\mathbf{s}_{jk}) \\ \vdots \end{bmatrix} = b^{(j)} + \mathbf{A}^{(j)}\mathbf{u}, \\ \mathbf{J}^{(j)} &= \begin{bmatrix} \frac{\partial m_j}{\partial u_1} & \dots & \frac{\partial m_j}{\partial u_L} \end{bmatrix}, \\ \mathbf{H}^{(j)} &= \begin{bmatrix} \frac{\partial^2 m_j}{\partial u_1^2} & \dots & \frac{\partial^2 m_j}{\partial u_1 \partial u_L} \\ \vdots & \ddots & \vdots \\ \frac{\partial^2 m_j}{\partial u_L \partial u_1} & \dots & \frac{\partial^2 m_j}{\partial u_L^2} \end{bmatrix}. \end{aligned}$$

Then for the  $j$ -th component of the first-order derivative, we denote  $q_{jk} = w_{jk} \exp(\eta_{jk})$  and  $\mathbf{A}_{kl}^{(j)} = \frac{\partial \eta_{jk}}{\partial u_l}$  and we have

$$\frac{\partial m_j}{\partial u_l} = \frac{\sum_k w_{jk} \exp(\eta_{jk}) \frac{\partial \eta_{jk}}{\partial u_l}}{\sum_k w_{jk} \exp(\eta_{jk})}$$

$$\begin{aligned}
&= \frac{\sum_k q_{jk} \frac{\partial \eta_{jk}}{\partial u_l}}{\sum_k q_{jk}} \\
&= \frac{\sum_k q_{jk} \mathbf{A}_{kl}^{(j)}}{\sum_k q_{jk}} < \infty \\
&= \frac{\mathbf{A}^{(j)\top} \mathbf{q}^{(j)}}{\mathbf{1}^\top \mathbf{q}^{(j)}}.
\end{aligned}$$

Since the term  $\mathbf{q}^{(j)}$  is bounded by definition given a stable integration scheme, thus the Jacobian term is bounded. For the second-order derivative, by the quotient rule  $\frac{d}{dx} \frac{f}{g} = \frac{f'g - fg'}{g^2}$ , and for some  $l, l' = 1, \dots, L$ , we have

$$\frac{\partial^2 m_j}{\partial u_l \partial u_{l'}} = \frac{(\sum_k q_{jk})(\sum_k q_{jk} \mathbf{A}_{kl}^{(j)} \mathbf{A}_{kl'}^{(j)}) - (\sum_k q_{jk} \mathbf{A}_{kl}^{(j)})(\sum_k q_{jk} \mathbf{A}_{kl'}^{(j)})}{(\sum_k q_{jk})^2} < \infty.$$

Hence, the matrix  $\mathbf{J}^{(j)}$  is a ratio with nominator adjusted by the gradient of the linear predictor function at  $\mathbf{u}$ .  $\mathbf{H}^{(j)}$  is the difference between the ratios. For  $l, l' = 1, \dots, L$ ,  $\frac{\partial m_j}{\partial u_l} < \infty$  and  $\frac{\partial^2 m_j}{\partial u_l \partial u_{l'}} < \infty$  are bounded. To further simplify the notation, we denote

$$\begin{aligned}
\mathbf{q}^{(j)} &= \mathbf{q}_{j\cdot}, \\
\widehat{\mathbf{q}}^{(j)} &:= \frac{\mathbf{q}^{(j)}}{\sum_k q_{jk}}, \\
\mathbf{d}^{(j)} &= \text{diag}(\mathbf{q}^{(j)}), \\
\widehat{\mathbf{d}}^{(j)} &= \text{diag}\left(\frac{\mathbf{q}^{(j)}}{\sum_k q_{jk}}\right).
\end{aligned}$$

Then we can simplify the expressions into,

$$\begin{aligned}
\mathbf{J}^{(j)} &= \mathbf{A}^{(j)\top} \widehat{\mathbf{q}}^{(j)} \\
\mathbf{H}^{(j)} &= \frac{(\mathbf{1}^\top \mathbf{q}^{(j)})(\mathbf{A}^{(j)\top} \mathbf{d}^{(j)} \mathbf{A}^{(j)}) - (\mathbf{A}^{(j)\top} \mathbf{q}^{(j)})(\mathbf{q}^{(j)\top} \mathbf{A}^{(j)})}{(\mathbf{1}^\top \mathbf{q}^{(j)})^2} \\
&= \mathbf{A}^{(j)\top} \widehat{\mathbf{d}}^{(j)} \mathbf{A}^{(j)} - \mathbf{A}^{(j)\top} \widehat{\mathbf{q}}^{(j)} \widehat{\mathbf{q}}^{(j)\top} \mathbf{A}^{(j)}.
\end{aligned}$$

## A.5 Aggregation Mapper

Here, we provide the implementation of the logarithmic sum, i.e.  $\bar{m}_j(\cdot)$  approximation mentioned in Section 2.1. The two mapper functions, `bru_mapper_aggregate` and `bru_mapper_logsumexp`, in the `inlabru` package, construct mapper objects to compute the blockwise sum and logarithmic sum of exponential terms in equation (16). Here the blocks (`sf_obj` in the sample code below) are defined by  $\Omega_j$ . By default, `n_block=NULL`, the maximum block index in the inputs is used, i.e. `nrow(sf_obj)`. Otherwise, `n_block` can be defined as the predetermined number of output blocks by users.

A shortcut tool for aggregating these latent state vectors  $\mathbf{u}$  to effect scalars  $\bar{m}_j(\mathbf{u})$  for each `inlabru` latent model component in equation (16) are provided by the low level mapper `bru_mapper_logsumexp`. This mappers aggregates elements of `exp(state)`, where `state` are components, with optional non-negative weighting, and then takes the `log()`, so it can be used

- for `rescale=FALSE` (default),  $v_k = \log[\sum_{i \in I_k} w_k \exp(u_i)]$ , and
- for `rescale=TRUE`,  $v_k = \log[\sum_{i \in I_k} w_k \exp(u_i) / \sum_{i \in I_k} w_k]$ .

The mapper `bru_mapper_logsumexp` relies on the input handling methods for `bru_mapper_aggregate`, but also allows the weights to be supplied on a logarithmic scale as `log_weights`.

To avoid numerical overflow, it uses the common method of internally shifting the state block-wise via  $\Omega_j$  with

```
(state-log_weights)[block] - max((state-log_weights)[block]),
```

and shifts the result back afterwards.

The reconstruction of continuous covariate field mentioned in Section 5.2.2 is to evaluate aggregated field with the piecewise linear mesh via the `bru_mapper_aggregate(..., rescale = TRUE)` mapper, where `rescale = TRUE` indicates that  $z_p$  is taken as the mean of the covariate field in the  $p$ -th polygon. A sample code is illustrated as follows.

```

R> # sf_obj: the aggregated polygon sf object
R> # matern: the model defined by inla.spde2.pcmatern here
R> cmp <- ~ x(main = geometry, model = matern)
R> agg_mapper <- bru_mapper_aggregate(rescale = TRUE,
+                                         n_block = NULL)
R> fml <- ~ ibm_eval(agg_mapper,
+                      input = list(block = .block,
+                                   weights = weight),
+                      state = x)

```

## B Derivations related to Computation

Here, we provide the derivations mentioned in Section 4.

### B.1 Nonlinear Taylor Expansion

Here, we provide the derivation of a further Taylor expansion on a nonlinear predictor expression mentioned in Section 4. This is an extension from the linearisation case in Appendices A.3 and A.4. Let  $f$  be some known non-linear function and once differentiable,

$$\eta_{jk} = b^{(j)} + \mathbf{A}^{(j)}f(\mathbf{u}), \text{ and } \frac{\partial \eta_{jk}}{\partial u_l} = \mathbf{A}^{(j)} \frac{\partial f(\mathbf{u})}{\partial u_l} < \infty.$$

With first-order Taylor expansion, we have

$$f(\mathbf{u}) = f(\mathbf{u}_*) + \mathbf{J}(\mathbf{u}_*)^\top (\mathbf{u} - \mathbf{u}_*) + \mathcal{O}(\|\mathbf{u} - \mathbf{u}_*\|^2).$$

## B.2 Linearisation Difference

Here, we provide the derivation of the difference between the continuous and discretised linearisation cases mentioned in Theorem 4.1.

By definition,  $\exp(x) := \sum_{k=0}^{\infty} \frac{x^k}{k!} = 1 + x + \frac{x^2}{2} + \dots$ , we ignore the higher-order terms that are more than or equal to cubic. Then we have the difference of the domain contribution terms between the continuous and discretised linearisation cases is

$$\begin{aligned}
\log \frac{\tilde{\mathbb{P}}(\mathbf{y}|\mathbf{u}, \boldsymbol{\theta})}{\mathbb{P}(\mathbf{y}|\mathbf{u}, \boldsymbol{\theta})} &= \sum_j^J e^{\bar{m}_j} - \sum_j^J e^{m_j} \\
&= \sum_j^J (e^{\bar{m}_j} - e^{m_j}) \\
&= \sum_j^J e^{\bar{m}_j} (1 - e^{m_j - \bar{m}_j}) \\
&= \sum_j^J [e^{\bar{m}_j(\mathbf{u}_*) + \mathbf{J}_j(\mathbf{u}_*)^\top(\mathbf{u} - \mathbf{u}_*)}] \\
&\quad \cdot \left[ 1 - \exp \left\{ \frac{1}{2} (\mathbf{u} - \mathbf{u}_*)^\top \mathbf{H}^{(j)} (\mathbf{u} - \mathbf{u}_*) + \mathcal{O}(\|\mathbf{u} - \mathbf{u}_*\|^3) \right\} \right] \\
&= - \sum_j^J [e^{\bar{m}_j(\mathbf{u}_*) + \mathbf{J}_j(\mathbf{u}_*)^\top(\mathbf{u} - \mathbf{u}_*)}] \\
&\quad \cdot \left[ \frac{1}{2} (\mathbf{u} - \mathbf{u}_*)^\top \mathbf{H}^{(j)} (\mathbf{u} - \mathbf{u}_*) + \mathcal{O}(\|\mathbf{u} - \mathbf{u}_*\|^3) \right] \\
&= - \sum_j^J [e^{\bar{m}_j(\mathbf{u}_*)} (1 + \mathbf{J}_j(\mathbf{u}_*)^\top(\mathbf{u} - \mathbf{u}_*) + \mathcal{O}(\|\mathbf{u} - \mathbf{u}_*\|^2))] \\
&\quad \cdot \left[ \frac{1}{2} (\mathbf{u} - \mathbf{u}_*)^\top \mathbf{H}^{(j)} (\mathbf{u} - \mathbf{u}_*) + \mathcal{O}(\|\mathbf{u} - \mathbf{u}_*\|^3) \right] \\
&= - \sum_j^J e^{\bar{m}_j(\mathbf{u}_*)} \left[ \frac{1}{2} (\mathbf{u} - \mathbf{u}_*)^\top \mathbf{H}^{(j)} (\mathbf{u} - \mathbf{u}_*) + \mathcal{O}(\|\mathbf{u} - \mathbf{u}_*\|^3) \right]
\end{aligned}$$

## B.3 Expectation Difference

Here, we provide the derivation of the expectation difference between the continuous and discretised linearisation cases mentioned in Theorem 4.1. We denote  $\mu_{\boldsymbol{\theta}} = \mathbb{E}(\mathbf{u}|\mathbf{y}, \boldsymbol{\theta})$  and  $\mathbf{Q}_{\boldsymbol{\theta}}^{-1} =$

$$\text{Var}(\mathbf{u}|\mathbf{y}, \boldsymbol{\theta}) = \mathbb{E}[(\mathbf{u} - \boldsymbol{\mu})(\mathbf{u} - \boldsymbol{\mu})^\top | \mathbf{y}].$$

$$\begin{aligned}
\mathbb{E}_{\mathbf{u} \sim \mathcal{N}(\boldsymbol{\mu}, \mathbf{Q}^{-1})} \left( \log \frac{\tilde{\mathbb{P}}(\mathbf{y}|\mathbf{u}, \boldsymbol{\theta})}{\bar{\mathbb{P}}(\mathbf{y}|\mathbf{u}, \boldsymbol{\theta})} \right) &= \mathbb{E}_{\mathbf{u} \sim \mathcal{N}(\boldsymbol{\mu}, \mathbf{Q}^{-1})} \left( \sum_{j=1}^J e^{\bar{m}_j} - \sum_{j=1}^J e^{m_j} \right) \\
&= \mathbb{E} \left( - \sum_j^J e^{\bar{m}_j(\mathbf{u}_*)} \left[ \frac{1}{2} (\mathbf{u} - \mathbf{u}_*)^\top \mathbf{H}^{(j)} (\mathbf{u} - \mathbf{u}_*) + \mathcal{O}(\|\mathbf{u} - \mathbf{u}_*\|^3) \right] \right) \\
&= -\frac{1}{2} \sum_j^J e^{\bar{m}_j(\mathbf{u}_*)} \mathbb{E} \left( \text{tr} [(\mathbf{u} - \mathbf{u}_*)^\top \mathbf{H}^{(j)} (\mathbf{u} - \mathbf{u}_*)] \right) \\
&\quad + \mathcal{O}(\mathbb{E} [\|\mathbf{u} - \mathbf{u}_*\|^3 | \mathbf{y}]) \\
&= -\frac{1}{2} \sum_j^J e^{\bar{m}_j(\mathbf{u}_*)} \\
&\quad \cdot \mathbb{E} \left( \text{tr} \left\{ \mathbf{H}^{(j)} [(\mathbf{u} - \boldsymbol{\mu}) + (\boldsymbol{\mu} - \mathbf{u}_*)] [(\mathbf{u} - \boldsymbol{\mu}) + (\boldsymbol{\mu} - \mathbf{u}_*)]^\top \right\} \right) \\
&\quad + \mathcal{O}(\mathbb{E} [\|\mathbf{u} - \mathbf{u}_*\|^3 | \mathbf{y}]) \\
&= -\frac{1}{2} \sum_j^J e^{\bar{m}_j(\mathbf{u}_*)} \left[ \text{tr}(\mathbf{H}^{(j)} \mathbf{Q}^{-1}) + (\boldsymbol{\mu} - \mathbf{u}_*)^\top \mathbf{H}^{(j)} (\boldsymbol{\mu} - \mathbf{u}_*) \right] \\
&\quad + \mathcal{O}(\mathbb{E} [\|\mathbf{u} - \mathbf{u}_*\|^3 | \mathbf{y}])
\end{aligned}$$

## B.4 Kullback-Leibler (KL) Divergence

Here, we provide the derivation of the KL divergence between the continuous and discretised linearisation cases mentioned in Theorem 4.2. We follow the proof of Theorem 1 in Lindgren et al. (2024) and denote

$$\mathbf{G} = \sum_i \mathbf{J}^{(i)}|_{\mathbf{u}_*} \mathbf{H}^{(i)}|_{\mathbf{u}_*} = - \sum_i e^{\bar{m}_i} \mathbf{H}^{(i)}. \quad (\text{B1})$$

We denote  $\bar{\mathbf{m}}_\boldsymbol{\theta} = \mathbb{E}_{\bar{p}}(\mathbf{u}|\mathbf{y}, \boldsymbol{\theta})$  and  $\bar{\mathbf{Q}}_\boldsymbol{\theta}^{-1} = \text{Cov}_{\bar{p}}(\mathbf{u}, \mathbf{u}|\mathbf{y}, \boldsymbol{\theta})$ . Hence, the first term in the KL divergence is

$$\mathbb{E}_{\bar{p}} [\log \tilde{p}(\mathbf{y}|\mathbf{u}, \boldsymbol{\theta}) - \log \bar{p}(\mathbf{y}|\mathbf{u}, \boldsymbol{\theta})] = \frac{1}{2} \text{tr}(\mathbf{G} \bar{\mathbf{Q}}_\boldsymbol{\theta}^{-1}) + \frac{1}{2} (\bar{\mathbf{m}}_\boldsymbol{\theta} - \mathbf{u}_*)^\top \mathbf{G} (\bar{\mathbf{m}}_\boldsymbol{\theta} - \mathbf{u}_*)$$

$$+ \mathcal{O}(\mathbb{E}_{\bar{p}} [\|\boldsymbol{u} - \boldsymbol{u}_*\|^3 | \boldsymbol{y}, \boldsymbol{\theta}]). \quad (\text{B2})$$

*Proof.* The KL divergence for the first and second Taylor expansion can be expressed as

$$\text{KL}\left(\tilde{\mathbb{P}}(\boldsymbol{u}|\boldsymbol{y}, \boldsymbol{\theta}) \middle\| \bar{\mathbb{P}}(\boldsymbol{u}|\boldsymbol{y}, \boldsymbol{\theta})\right) = E_{\tilde{\mathbb{P}}} \left[ \log \frac{\tilde{\mathbb{P}}(\boldsymbol{y}|\boldsymbol{u}, \boldsymbol{\theta})}{\bar{\mathbb{P}}(\boldsymbol{y}|\boldsymbol{u}, \boldsymbol{\theta})} \right] - \log \frac{\bar{\mathbb{P}}(\boldsymbol{y}|\boldsymbol{\theta})}{\tilde{\mathbb{P}}(\boldsymbol{y}|\boldsymbol{\theta})} \quad (\text{B3})$$

The details of the first term and corresponding derivation see Lindgren et al. (2024).

$$\begin{aligned} \mathbb{E}_{\bar{p}} \left[ \log \tilde{\mathbb{P}}(\boldsymbol{y}|\boldsymbol{u}, \boldsymbol{\theta}) - \log \bar{\mathbb{P}}(\boldsymbol{y}|\boldsymbol{u}, \boldsymbol{\theta}) \right] &= -\frac{1}{2} \text{tr}(\boldsymbol{G} \bar{\boldsymbol{Q}}_{\boldsymbol{\theta}}^{-1}) - \frac{1}{2} (\bar{\boldsymbol{\mu}}_{\boldsymbol{\theta}} - \boldsymbol{u}_*)^\top \boldsymbol{G} (\bar{\boldsymbol{\mu}}_{\boldsymbol{\theta}} - \boldsymbol{u}_*) \\ &\quad + \mathcal{O}(\mathbb{E}_{\bar{p}} [\|\boldsymbol{u} - \boldsymbol{u}_*\|^3 | \boldsymbol{y}, \boldsymbol{\theta}]) \end{aligned}$$

The second term above can be expressed as

$$-\text{tr} \left[ \left( \sum_j e^{\bar{m}_j(\boldsymbol{u}_*)} \boldsymbol{H}^{(j)} \right) (\boldsymbol{Q}_{\boldsymbol{\theta}} + \sum_j e^{\bar{m}_j(\boldsymbol{u}_*)} \boldsymbol{H}^{(j)})^{-1} \right], \quad (\text{B4})$$

where  $\boldsymbol{Q}_{\boldsymbol{\theta}}$  is the Gaussian prior on the latent variable  $\boldsymbol{u}$ .  $\square$

## B.5 Stable Integration Scheme

Here, we provide the technical details of a stable integration scheme mentioned in Sections 2.1 and 5.1. We present the stable integration scheme for  $\mathbb{R}^2$  implemented in INLA and `inlabru` packages. There are alternative stable integration schemes to be implemented in the pipeline.

We refer to a stable integration scheme as a bounded estimate of the likelihood which is the combination of the domain and the observed contribution, as shown in equation (4), is bounded, i.e.  $\ell(\lambda|\mathcal{Y}) < \infty$ . The calculation of observed contribution is evaluated at the observed point which further details available in Simpson et al. (2016).

We denote a function on a triangulation of space  $f(\cdot)$  with  $t = 1, \dots, n_t$  and  $v = 1, 2, 3$ , as the indices of the triangular mesh and the vertex respectively and  $\mathcal{T}_t$  referring to the  $t$ -th element. We

further define  $f_{(t,v)} := f(s_{(t,v)})$  and  $\sum_t^{n_t} \sum_{v \in \mathcal{T}_t} w_{(t,v)} = 1$ , for some weights  $\{w_{(t,v)}\}$ , and some vertices  $\{s_{(t,v)}\} \subset \Omega$  inside the sample space. The domain contribution can be approximated via integration points as,

$$\int_{\Omega} f(s) ds \approx \sum_t^{n_t} \sum_{v \in \mathcal{T}_t} w_{(t,v)} f_{(t,v)}; \quad (\text{B5})$$

A 3-column integer matrix with 1-based vertex indices for each triangle  $(t, v)$  (with reference to `mesh$loc`) is stored under `mesh$graph$tv` in the mesh object under the `fmesher` package.

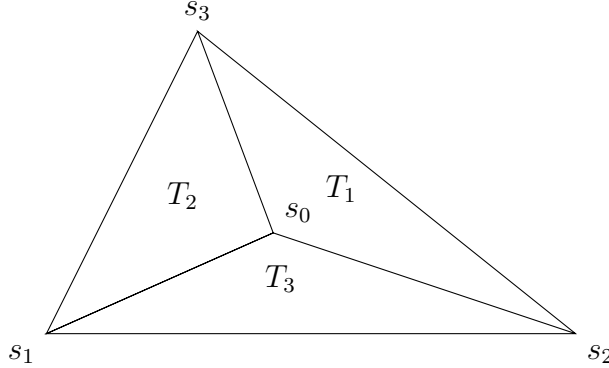


Figure 10: Barycentric coordinates of a triangle. The volume of  $T_v$  for  $v = 1, 2, 3$  is  $|T_{(t,v)}|$ .

We illustrate with a single triangle, i.e.  $t = 1$ , as in Figure 10. We denote the volume of the triangle  $|T_{(t,\cdot)}| = \sum_{v=1}^3 |T_{(t,v)}|$  where  $|T_{(t,v)}$  are the volume of the sub-triangles through barycentric subdivision. We assume a piecewise linear function within the triangle  $\Delta s_1 s_2 s_3$ . The barycentre can be computed

$$s_{t_0} = \sum_{v=1}^3 w_{(t,v)} s_{(t,v)}; \quad w_{(t,v)} = \frac{|T_{(t,v)}|}{|T_{(t,\cdot)}|}, \quad (\text{B6})$$

where  $w_{t,v}$  is known as the barycentric coordinates with respect to  $s_{t_0}$ . Since the triangle is piecewise linear,  $w_{t,v} = \psi_{k(t,v)}(s_{t_0})$  specified in equation (6). The weighted sum of a function evaluated at these points is the integral of this function approximated by linear basis functions  $\psi_{k(t,v)}$  as in equation (6). Hence, the function evaluated at the barycentre

$$f(s_{t_0}) = \sum_{v=1}^3 w_{(t,v)} f_{(t,v)}. \quad (\text{B7})$$

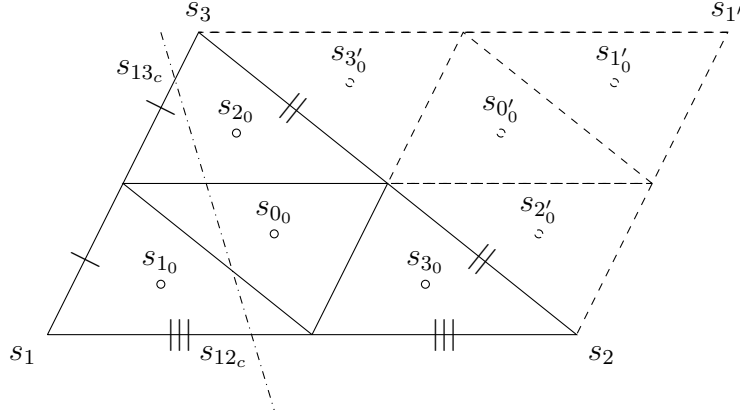


Figure 11: Illustration of integration points with mirror triangle and mid-edge subdivision. Circle: integration points; Points above the diagonal ( $s_2s_3$ ) should be reflected into the lower triangle. Solid line: triangular mesh; Dashed line: mirror image; Dashdotted line: cut.

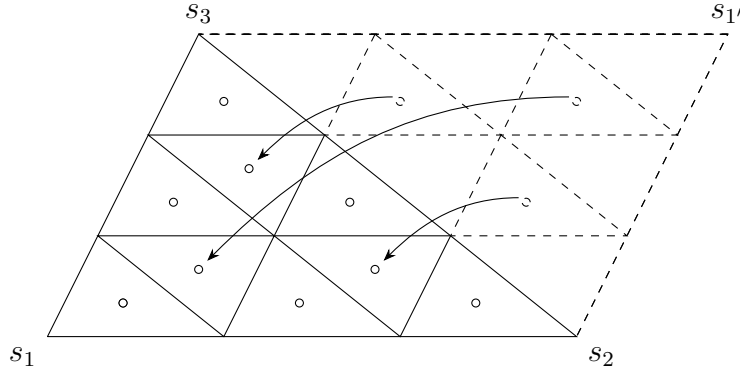


Figure 12: Illustration of integration points with mirror triangle and mid-edge subdivision. Circle: integration points; Solid line: triangular mesh; Dashed line: mirror image

We mirror the triangular element to create a parallelogram and distribute integration points  $s_{i_0}$  for  $i = 1, \dots, n$  over the parallelogram in Figure 11 and halve the integration in the end. Generally speaking, the more integration points are, the more accurate the approximation is. It is an implementation trick to avoid considering whether the integration points are inside or outside the triangle. The integration points are the barycentres of the sub-triangles generated via mid-edge subdivision. Let  $w_{(t_i, v)}$  be the barycentric weight with respect to the  $v$ -th vertex of the  $i$ -th sub-triangle in the  $t$ -th triangle and  $s_{t_i 0}$  be the barycentre of the sub-triangle. The integral of the function for the triangle can be approximated as

$$\begin{aligned}
\int_{|T_{(t,\cdot)}|} f(s_{t_0}) ds &\approx \frac{|T_{(t,\cdot)}|}{n} \sum_{i=1}^n f(s_{t_{i_0}}) \\
&= \frac{|T_{(t,\cdot)}|}{n} \sum_{i=1}^n \sum_{v=1}^3 f_{(t_i, v)} w_{(t_i, v)} \\
&= \sum_{v=1}^3 f_{(t, v)} \underbrace{\frac{|T_{(t,\cdot)}|}{n} \sum_{i=1}^n w_{(t_i, v)}}_{:=w_{(t, v)}}
\end{aligned} \tag{B8}$$

In the scenario of removing a part of the integration via triangle dissection, say due to out of the boundary  $\partial\Omega$ , we simply set the weights to zero. For instance, the line segment  $s_{13_c}s_{12_c}$  cuts through the mesh, thus  $\Delta s_1 s_{13_c} s_{12_c}$  is removed and the weight of  $s_{1_0}$  set to zero in Figure 11). Refer to Hjelle and Dæhlen (2006) for further details of the algorithm.

If we consider the function  $f(\cdot)$  to be nonlinear, we can improve the approximation by subdividing each mesh through the mid-edge subdivision thus with more integration points, each with less weight (via `fm_subdivide` function in the `inlabru` package, see figure 13). When the sub-triangles are sufficiently fine in scale, we can assume piecewise linear sub-triangles and approximate the integral. Gaussian quadrature rule is considered as well but reweighing integration points on the corners complicates the rule when there is a cut.

A sample code of the `bru_mapper_logsumexp` mapper is shown below.

```
R> logsumexp_mapper <- bru_mapper_logsumexp(
+   rescale = FALSE,
+   n_block = nrow(sf_object))
R> formula <- ~ ibm_eval(logsumexp_mapper,
+   input = list(block = .block, weights = weight),
+   state = state)
```

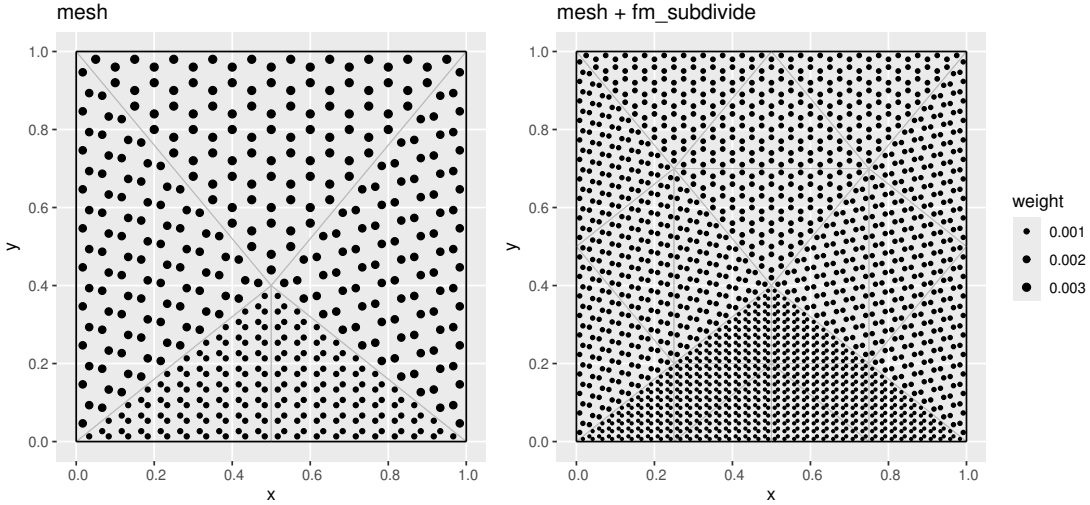


Figure 13: An example of integration points weights given a triangulation over a unit square

## B.6 Degree of Freedom (DoF)

Here, we provide the technical details of the degree of freedom (Dof) mentioned in Section 2.1.1.

We use the notations from the previous section B.5. The DoF is a measure of the flexibility of a function space. We simplify and rewrite equation (6) as

$$\log \lambda(\mathbf{s}) = \eta(\mathbf{s}) := u(\mathbf{s}) = \sum_{k=1}^K \psi_k(\mathbf{s}) u_k, \quad (\text{B9})$$

for some weight  $u_k$ . Given the volume of the bounded domain  $|\Omega|$  is fixed, we only consider the latter two terms in equation (4), and combining with equation (B5),

$$-\int_{\Omega} \lambda(\mathbf{s}) d\mathbf{s} + \sum_{i=1}^n \log \lambda(y_i) \approx - \sum_t \sum_{v \in \mathcal{T}_t} w_{(t,v)} \lambda_{(t,v)} + \sum_{i=1}^n \sum_{k=1}^K u_k \psi_k(y_i), \quad (\text{B10})$$

where  $\{u_1, \dots, u_k\}$  is defined in equation (6). We can see observations are pulling the likelihood upwards, hence the locations of the integration points are crucial to bound the estimation of the likelihood.

By placing the integration points at proper locations in the domain space, we can bound the likelihood specified in equations (4) and (5). We now illustrate how the construction in equation

(B8) is crucial to obtain stable estimation for the numerical integration of the likelihood function.

We consider an example of unstable and stable integration schemes via one dimensional mesh on the range  $[0, 1]$  (see Figure 14). We only put one integration point at  $x = 0.5$  for the unstable one but two at 0 and 1 for the stable one. We have one observation point for both cases. Describe the Arrows. Figure 5 the single point integration scheme leads to an unbounded integration. Since we put the integration point at the end points, we can stabilise the integration. This one dimensional mesh example translates to the integration points in triangular mesh formulation. The message that we want to convey here is with `fmesher::fm_subdivide` which subdivides an existing mesh, we can improve the approximation of likelihood by placing the more integration points evaluated at more locations.

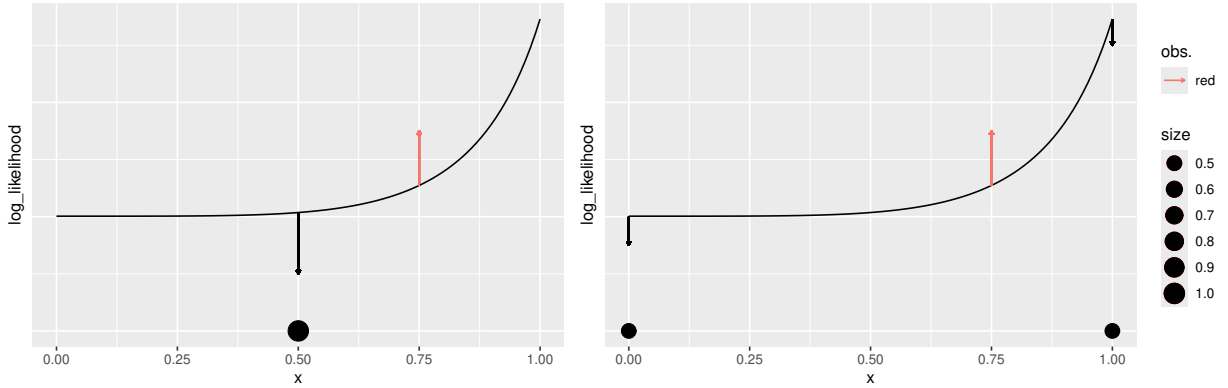


Figure 14: Unstable integration point (left) and stable integration point (right) with respect to log-likelihood for a single observation point (red). Arrow: observed contribution (red), domain contribution (black).

## C Simulation

Here, we provide the implementation details and plots of the simulation study mentioned in Section 5.

## C.1 Implementation Details of `fmesher::fm_extensions`

Here, we provide the implementation details of the function `fmesher::fm_extensions` mentioned in Section 5.1. The function `fmesher::fm_extensions` constructs inner and outer boundaries of a mesh. internally calls `fmesher::fm_nonconvex_hull` to create nonconvex hull over the domain.

```
R> # d1, d2: some distances from the boundary
R> mesh <- fm_mesh_2d_inla(...,
+                               boundary = fm_extensions(bnd,
+                               c(d1, d2)))
```

For this reason, the covariate field is simulated over the mesh domain for the purpose of easy handling. In real life, we might not have data at the buffered region that `inlabru::bru_fill_missing` can help fill missing data with nearest neighbour.

## C.2 Sampling from an Inhomogeneous Poisson Process

Here, we provide the implementation details of the function `inlabru::sample.lgcp` mentioned in Section 5.1. The function `inlabru::sample.lgcp` is a function for sampling from an inhomogeneous Poisson process. The log intensity has to be provided via its values at the vertices of the mesh elements. In between mesh nodes the log intensity is assumed to be linear. The function is called as follows:

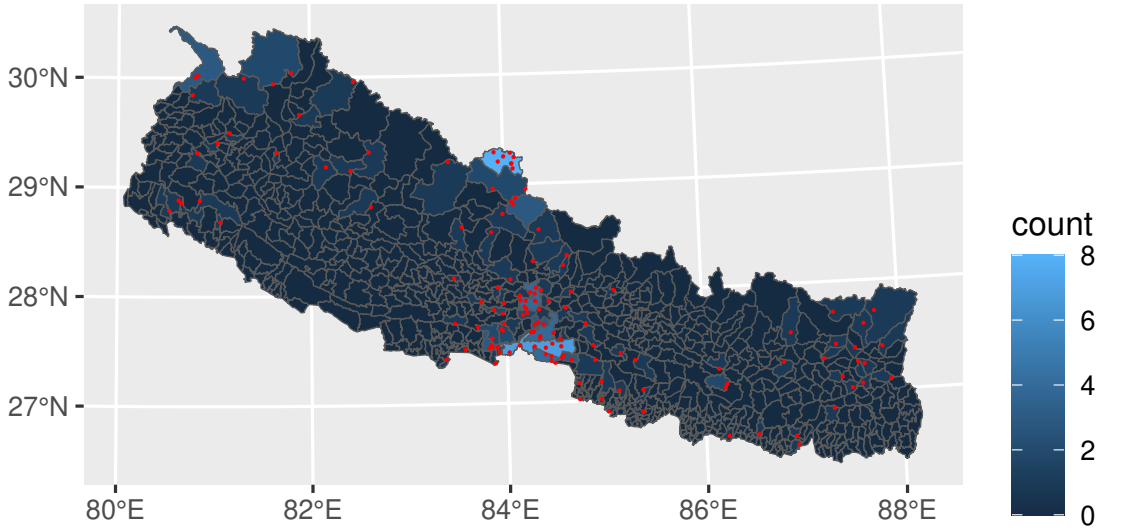
```
R> # mesh: An INLA::inla.mesh object
R> # loglambda: A vector of log intensities at the mesh vertices
R> # samplers: A sf or inla.mesh object where simulated points
R> #                               that fall outside these polygons are discarded.
R> sample.lgcp(mesh, loglambda, samplers)
```

The algorithm is based on rejection sampling. The maximum of the `loglambda`, denoted by `wmax`, is input to simulate a Poisson random variable based on the product of the areas of the mesh elements and the maximal for each mesh element. If this random variable is larger than zero, another uniform random variable is simulated based on this Poisson random variable. The point(s) is only accepted with a probability that the uniform random variable is smaller than  $\exp(\text{loglambda} - \text{wmax})$ . This is repeated for all mesh elements within the samplers.

### C.3 Simulated Point Pattern

Here, we provide the plots of the simulated point patterns mentioned in Section 5.1. The point pattern observations over Nepal are simulated via `sample.lgcp` (see Appendix C.2) according to equation (1) with the linear predictor  $\eta(\mathbf{s}) = \beta_0 + \beta_x X(\mathbf{s}) + u(\mathbf{s})$ , where  $X(\mathbf{s})$  is a continuous covariate field formulated as  $(s_1^2 - s_2^2) \exp\left[-\frac{1}{2}(s_1^2 + s_2^2)\right]$ ;  $s_1 \in [-4, 4]$ ,  $s_2 \in [-2, 2]$  projected to Nepal, and  $u(\mathbf{s})$  is defined in equation (6). We set  $\beta_0 = -7$ ,  $\beta_x = -6$  and  $u(\mathbf{s})$  with  $\rho = 50$  and  $\sigma = 0.5$ . The nonlinear transformation of the covariate field is via a nonlinear function  $f(\cdot)$ , i.e.  $\log \check{\lambda}(\cdot) := \check{\eta}(\cdot) = \beta_0 + \beta_x f[X(\cdot)] + u(\cdot)$ . We construct  $f(\cdot)$  as a nonlinear function,  $f[X(\cdot)] = b^{-1} \exp[aX(\cdot)] - c$ , where we set  $a = 3$ ,  $b = 9$  and  $c = 3$ .

Aggregated Count



Aggregated Count NL

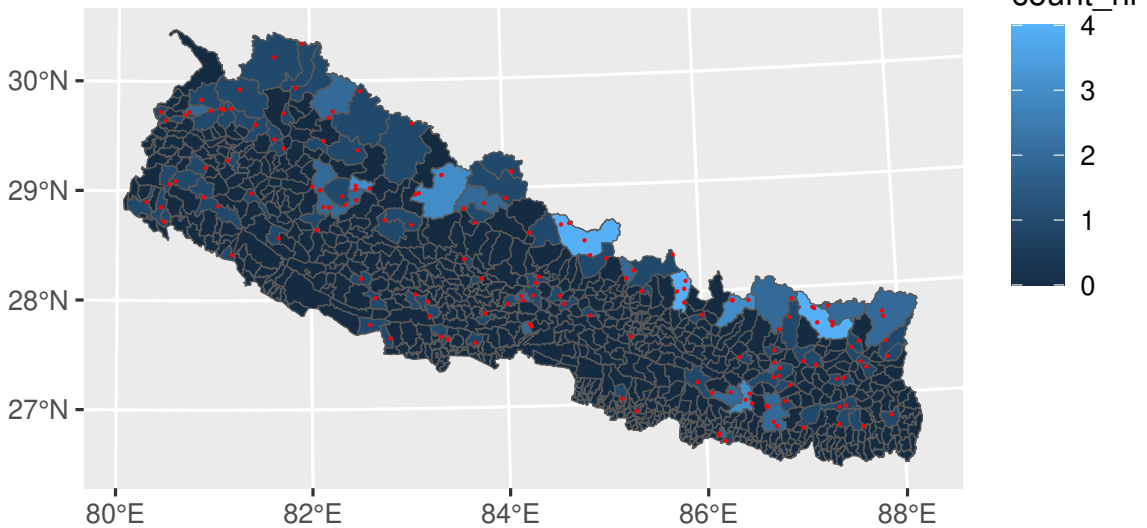


Figure 15: Simulated point pattern (red dots) and aggregated count observations from covariate field (top) and covariate field after nonlinear transformation (bottom). The underlying intensity field of the top panel follows equation (21) in the main text while the bottom follows equation in the main text.

#### C.4 Sampled Covariate Points

Here, we illustrate the plot of Incomplete covariate field for Point Values (PointVal) mentioned in Section 5.1.3. We sample one point from each administrative district and evaluate the covariate

field at that point.

### Sampled covariate point locations

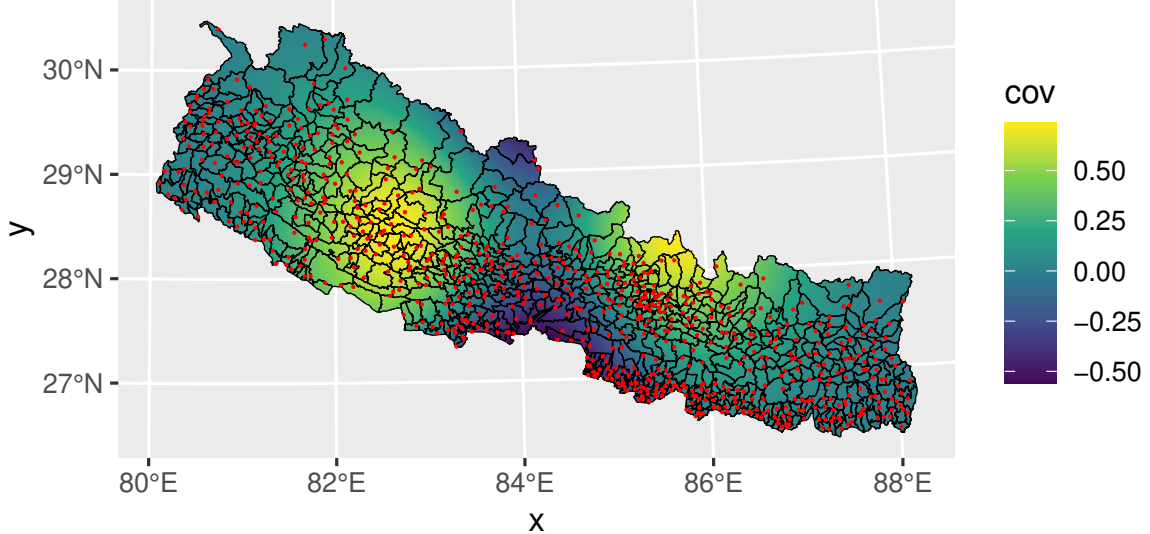


Figure 16: Sampled covariate points (red dots) with the covariate field.

## C.5 PC Priors

Here, we provide the implementation code for the Penalised Complexity (PC) priors mentioned in Sections 5.2.1, 5.2.2 and 5.2.5. The PC priors are implemented in the `inlabru::inla.spde2.pcmatern` function. The PC priors are used to set the range and standard deviation of the Matérn covariance function following equation (11).

In Sections 5.2.1 and 5.2.2, the PC priors for *mesh (i)* are set to be  $\mathbb{P}(\rho < 4) = 0.1$  and  $\mathbb{P}(\sigma > 2) = 0.1$ .

In Section 5.2.5, the PC priors for *mesh (ii)* are set to be  $\mathbb{P}(\rho < 8) = 0.1$  and  $\mathbb{P}(\sigma > 2) = 0.1$ .

The PC priors are implemented for *mesh (i)* as follows:

```
R> INLA::inla.spde2.pcmatern(mesh_A, prior.range = c(4, 0.1),
+                               prior.sigma = c(2, 0.1))
```

## C.6 Rasterisation

Here, we provide the cell area range and the implementation details of the rasterisation mentioned in Sections 3.2 and 5.1.

	RastFull	RastAgg	Predicted raster	Mesh A	Mesh B
Cell Area range ( $km^2$ )	0.737	73.70	2.61	6.787	26.11

Table 3: Area of the rasters and meshes.

A rule of thumb is that the mesh resolution should not be 10 times larger than the data resolution in length, i.e.  $\max.\text{edge} < \frac{1}{10} \cdot \text{correlation range}$ , in the `fmesher::fm_mesh_2d()` argument.

## C.7 Precision Matrix (**CMatrix**)

Here we illustrate how to convert upper triangular storage precision matrix  $\mathbf{U}_{\epsilon_x}$  generated from INLA into the full symmetric matrix  $\hat{\mathbf{Q}}_{\epsilon_x}$  mentioned in Sections 5.2.5 and 7.2.

$$\text{adiag}(\hat{\mathbf{Q}}_{\epsilon_x}) = \text{adiag}(\mathbf{U}_{\epsilon_x} + \mathbf{U}_{\epsilon_x}^\top)$$

$$\text{diag}(\hat{\mathbf{Q}}_{\epsilon_x}) = \text{diag}(\mathbf{U}_{\epsilon_x}),$$

where `adiag` denotes the anti-diagonal matrix. The implementation code for fitting Type 0 generic model and making the full symmetric precision matrix is shown below.

```
R> # fit: a INLA/inlabru bru object
R> # cmp: inlabru model component object
R> # make_sym function to make the precision matrix symmetric
R> make_sym <- function(Q) {
+   d <- diag(Q)
+   Q <- (Q + t(Q))
+   diag(Q) <- d
+   return(Q)
```

```

+
}

R> Q_hat <- make_sym(fit$misc$configs$config[[1]]$Q)

R> cmp <- ~ covariate(geometry,
+
+                         mapper = bru_get_mapper(matern),
+
+                         model = "generic0", Cmatrix = Q_hat)

```

Type 0 generic model implements a precision matrix  $\mathbf{Q} = \tau \hat{\mathbf{Q}}_{\epsilon_x}$  as in equation 26, where  $\tau$  is a precision parameter.

We did not explore different priors for the precision matrix in this paper. However, different initial values can be set to explore the effect of the priors on the estimation.

### C.7.1 Creating a Mesh for Prediction `fm_pixels`

Here, we present an alternative method to create a rasterised mesh for prediction mentioned in Section 5.2.5. The function `fmshер::fm_pixels` can generate lattice locations from a rasterised mesh for prediction. A sample code is shown below.

```

R> # mesh: the mesh object
R> # dims: the dimensions of the raster
R> # mask: the boundary sf object
R> fm_pixels(mesh, dims = rep(250, 2),
+
+             mask = bnd_buff, format = "sf")

```

## C.8 One- and Two-stage Uncertainty Quantification

Here, we illustrate the analytical and computational approaches for accessing the stability of the model mentioned in Section 5.2.7.

### C.8.1 Analytical Approach for Uncertainty Quantification

Here, we try to find a closed form solution for the derivatives of the density with respect to the coefficient and the uncertainty term.

$$\begin{aligned}
\frac{\partial \log p(\theta|x)}{\partial \epsilon_{x_j}} &= \sum_j (-e^{\eta_j} + y_j)(\beta_x) - \frac{\epsilon_{x_j}}{\sigma_{x_j|z_p}^2} = 0 \\
\frac{\partial^2 \log p(\theta|x)}{\partial \epsilon_{x_j}^2} &= \sum_j -e^{\eta_j} \beta_x^2 - \frac{1}{\sigma_{x_j|z_p}^2} < 0 \\
\frac{\partial \log p(\theta|x)}{\partial \beta_x} &= \sum_i (-e^{\eta_i} + y_i)(\hat{x}_i + \epsilon_{x_i}) = 0 \\
\frac{\partial^2 \log p(\theta|x)}{\partial \beta_x^2} &= \sum_i (-e^{\eta_i})(\hat{x}_i + \epsilon_{x_i})^2 \leq 0 \\
&\Rightarrow \sum_i \frac{\epsilon_{x_i}(\hat{x}_i + \epsilon_{x_i})}{\beta_x \sigma_{x_i|z_i}^2} = 0 \\
&\Rightarrow \sum_i \frac{(\hat{x}_i \epsilon_{x_i} + \epsilon_{x_i}^2)}{\sigma_{x_i|z_i}^2} = 0 \\
&\Rightarrow \sum_i \left( \frac{\hat{x}_i + 2\epsilon_{x_i}}{2\sigma_{x_i|z_i}} \right)^2 = \sum_i \left( \frac{\hat{x}_i}{2\sigma_{x_i|z_i}} \right)^2
\end{aligned}$$

Hence, we cannot derive a closed form solution for the derivatives.

### C.8.2 Profile Likelihood for Uncertainty Quantification

Since we cannot derive a closed form solution, we seek to optimise the profile likelihood for the coefficient. Here, we illustrate one dimensional toy example for JU, VP and UP methods. We use the profile likelihood to optimise  $\beta_x$  with  $n_z \in \{2, 4, 8, 16, 32, 64, 128, 256\}$ ,  $\arg \max_{\beta_x} (\arg \max_{(\beta_0, \epsilon_x)} (\mathfrak{p}))$  as in equation (27) in Section 5.2.7. In Figures 17 and 18, there are only one global maximum for JU and VP methods. However, in Figure 19, there is another one local maximum for  $\beta_x$  approaching infinity for UP method. This shows that one should be careful about the initial starting points when using the UP method. Nonetheless, we did not encounter optimisation issues in the simulation.

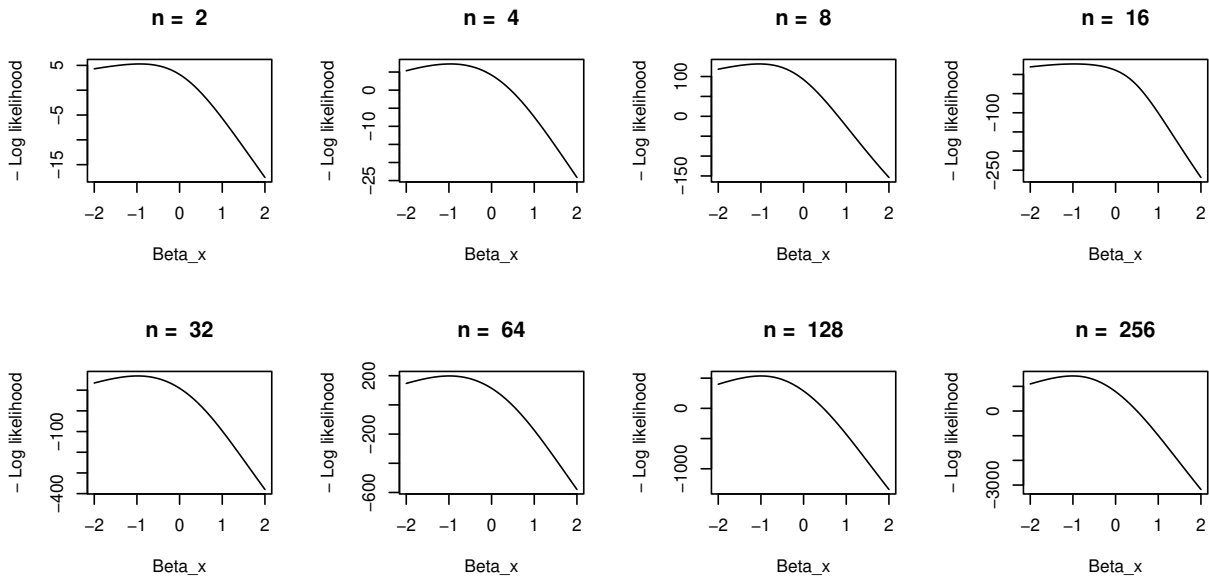


Figure 17: Profile likelihood optimisation of  $\beta_x$  for single-stage Joint Uncertainty (JU) approach.

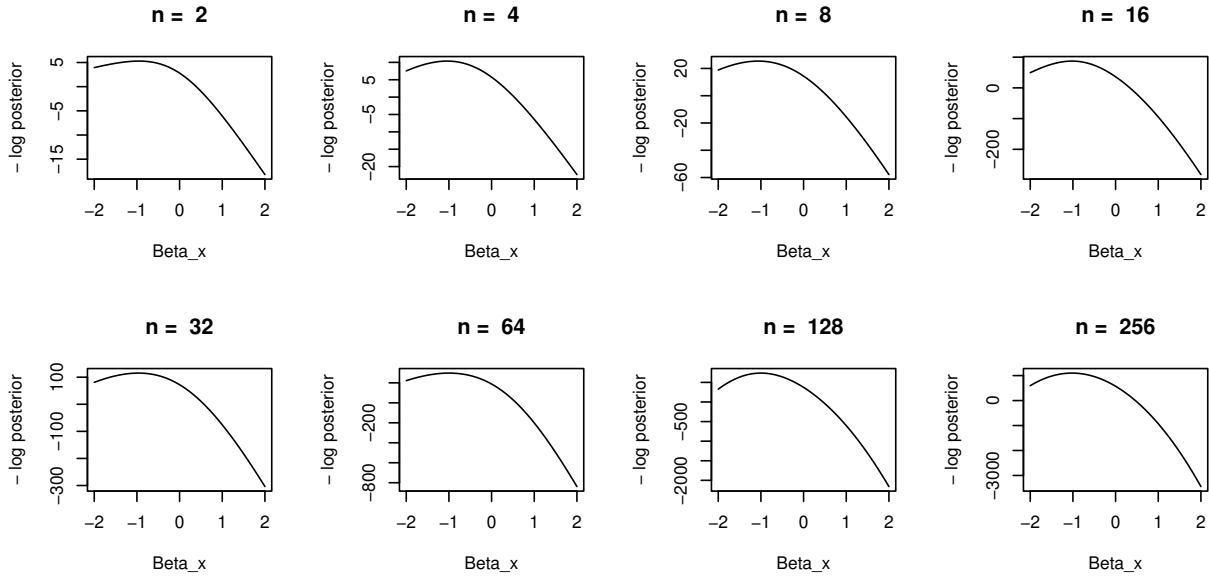


Figure 18: Profile likelihood optimisation of  $\beta_x$  for two-stage Value Plugin (VP) approach.

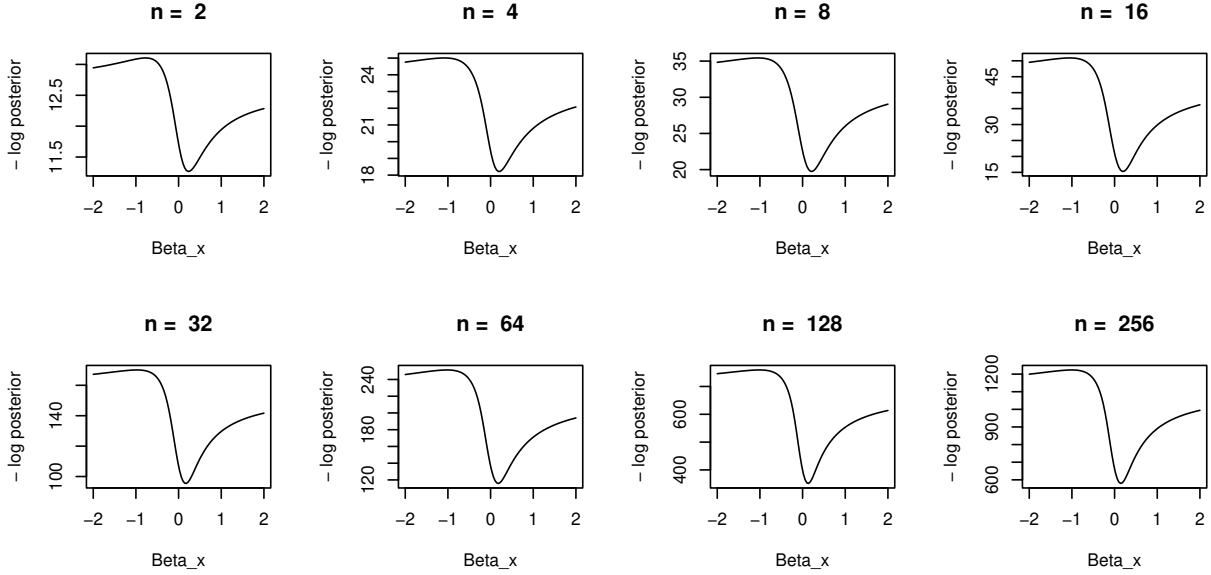


Figure 19: Profile likelihood optimisation of  $\beta_x$  for two-stage Uncertainty Plugin (UP) approach.

## C.9 Covariate Estimation under Incomplete Covariate Field Scenario

The table and plots refer to Section 6.2.

Cov.	Obs.	Method	MSE	MDS	$\bar{X}(\cdot)$
PolyAgg	$\mathcal{Y}, \check{\mathcal{Y}}, \mathcal{N}, \check{\mathcal{N}}$	VP and UP	$7.915 \times 10^{-6}$	$-1.115 \times 10^1$	0.18262
	$\mathcal{Y}$	JU	$7.571 \times 10^{-6}$	$-1.116 \times 10^1$	
	$\mathcal{N}$		$7.575 \times 10^{-6}$	$-1.116 \times 10^1$	
	$\check{\mathcal{Y}}$		$7.562 \times 10^{-6}$	$-1.116 \times 10^1$	
	$\check{\mathcal{N}}$		$7.513 \times 10^{-6}$	$-1.116 \times 10^1$	
PointVal	$\mathcal{Y}, \check{\mathcal{Y}}, \mathcal{N}, \check{\mathcal{N}}$	VP and UP	$1.309 \times 10^{-3}$	-5.842	0.18262
	$\mathcal{Y}$	JU	$1.116 \times 10^{-3}$	$-5.908$	
	$\mathcal{N}$		$1.163 \times 10^{-3}$	-5.891	
	$\check{\mathcal{Y}}$		$1.247 \times 10^{-3}$	-5.861	
	$\check{\mathcal{N}}$		$1.196 \times 10^{-3}$	-5.883	

Table 4: Table of the Mean Squared Error (MSE) and Mean Dawid-Sebastiani (MDS) scores for the covariate field  $x$  across the models under incomplete covariate field scenario. PointVal: Point Values, PolyAgg: Polygon Aggregation,  $\bar{X}(\cdot)$ : Mean of Covariate field.

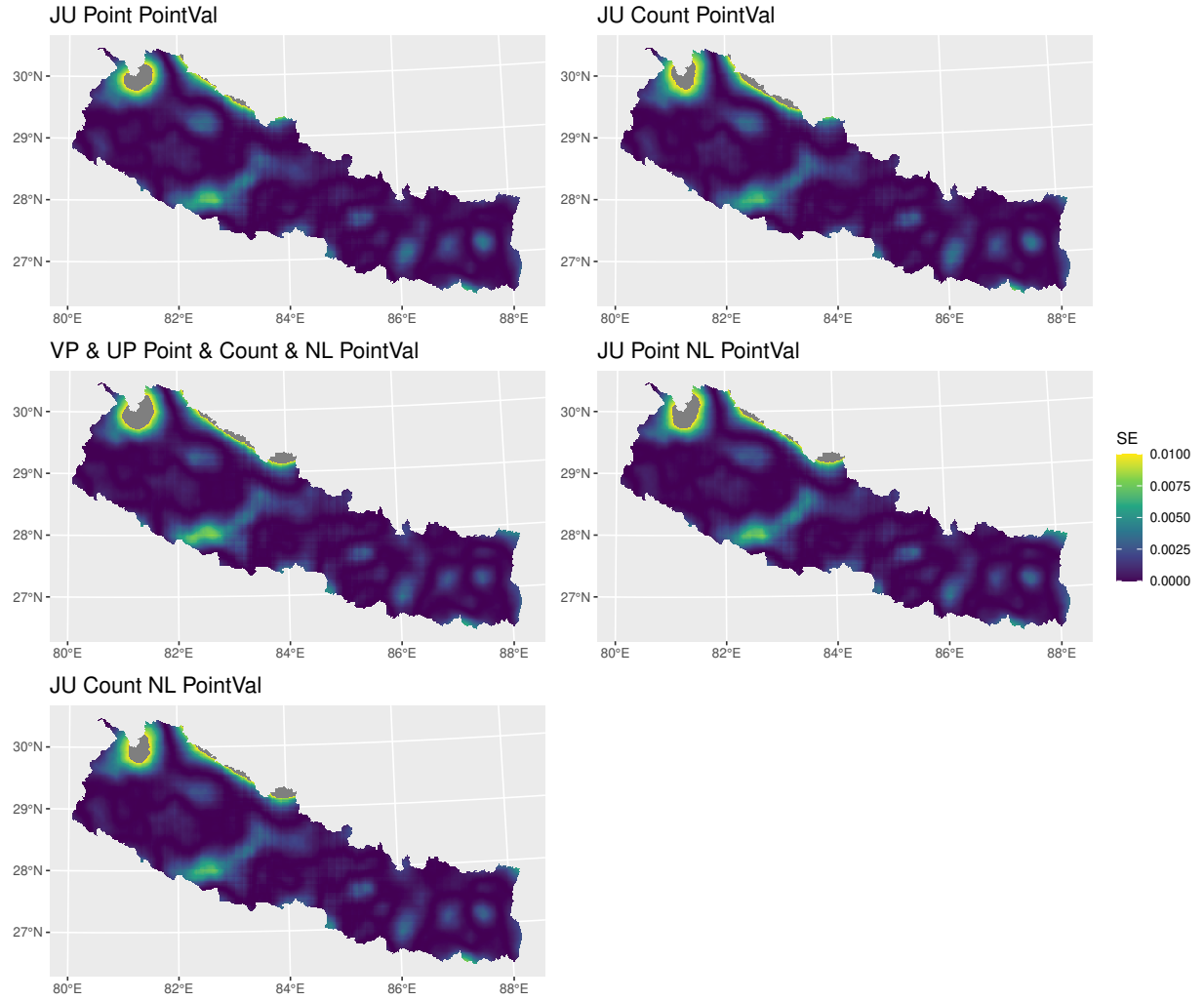


Figure 20: Squared Error (SE) for the covariate field  $X$  across the models under incomplete covariate field scenario with observed noises  $\sigma_{\epsilon_x}$  (truncated at 0.01). JU: Joint Uncertainty, VP: Value Plugin, UP: Uncertainty Plugin, Point: Observed Point, Count: Aggregated Count, PointVal: Point Values.  $\bar{X}(\cdot) = 0.18262$

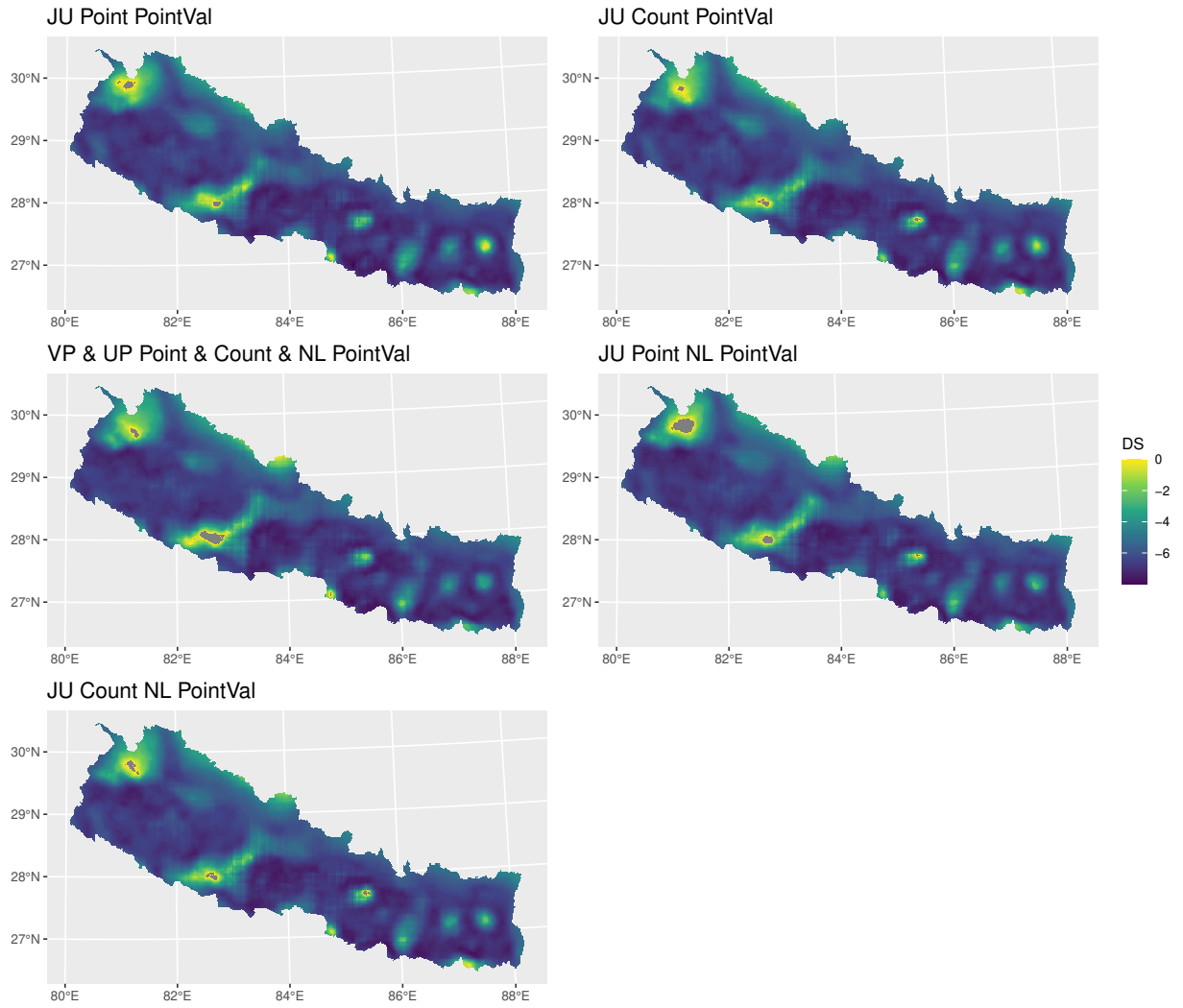


Figure 21: Dawid-Sebastiani (DS) score for the covariate field  $X$  across the models under incomplete covariate field scenario with observed noises  $\sigma_{\epsilon_x}$  (truncated at 0). JU: Joint Uncertainty, VP: Value Plugin, UP: Uncertainty Plugin, Point: Observed Point, Count: Aggregated Count, PointVal: Point Values.

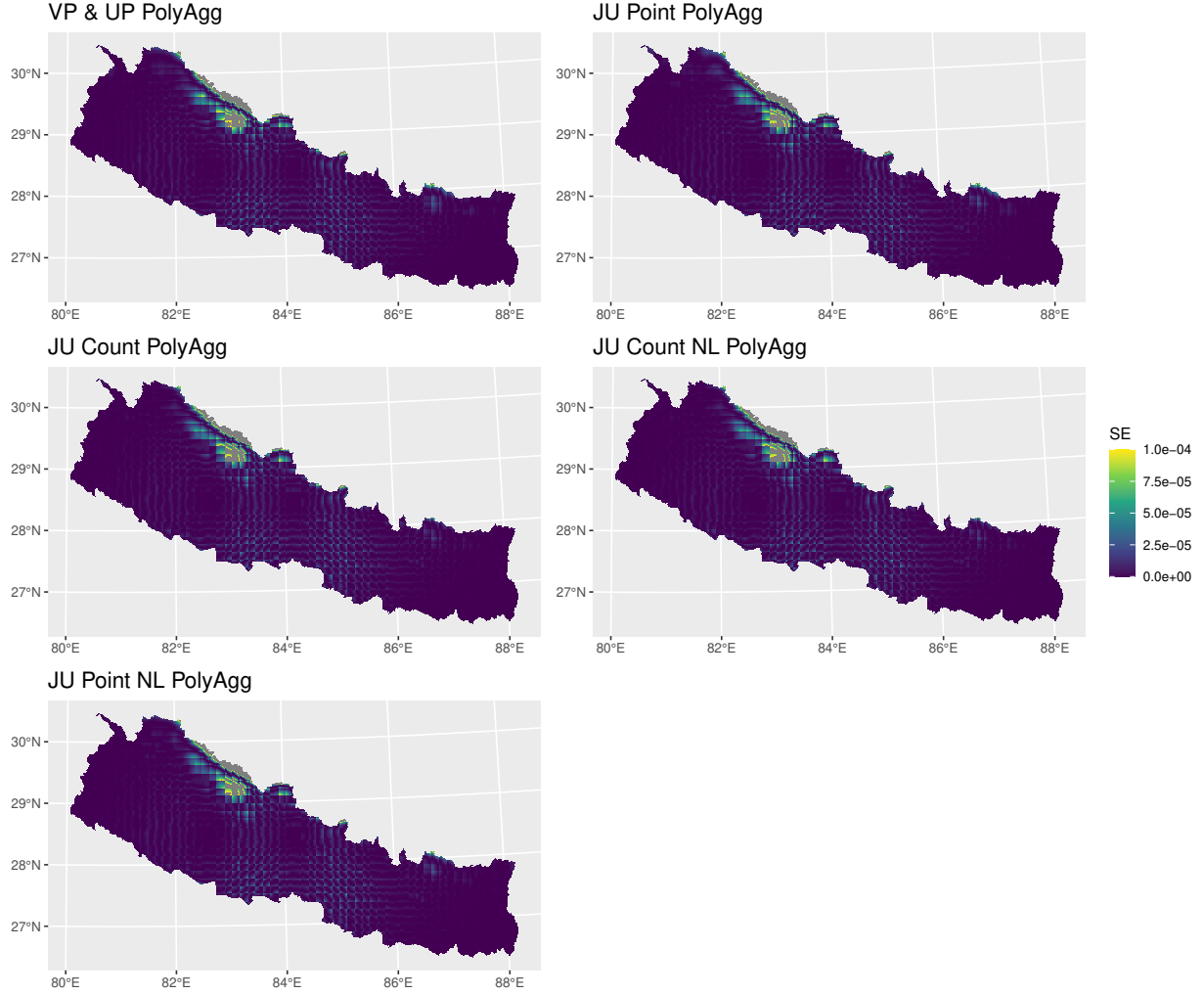


Figure 22: Squared Error (SE) for the covariate field  $X$  across the models under incomplete covariate field scenario with observed noises  $\sigma_{\epsilon_x}$  (truncated at  $1 \times 10^{-4}$ ). JU: Joint Uncertainty, VP: Value Plugin, UP: Uncertainty Plugin, Point: Observed Point, Count: Aggregated Count, PolyAgg: Polygon Aggregation.  $\bar{X}(\cdot) = 0.18262$

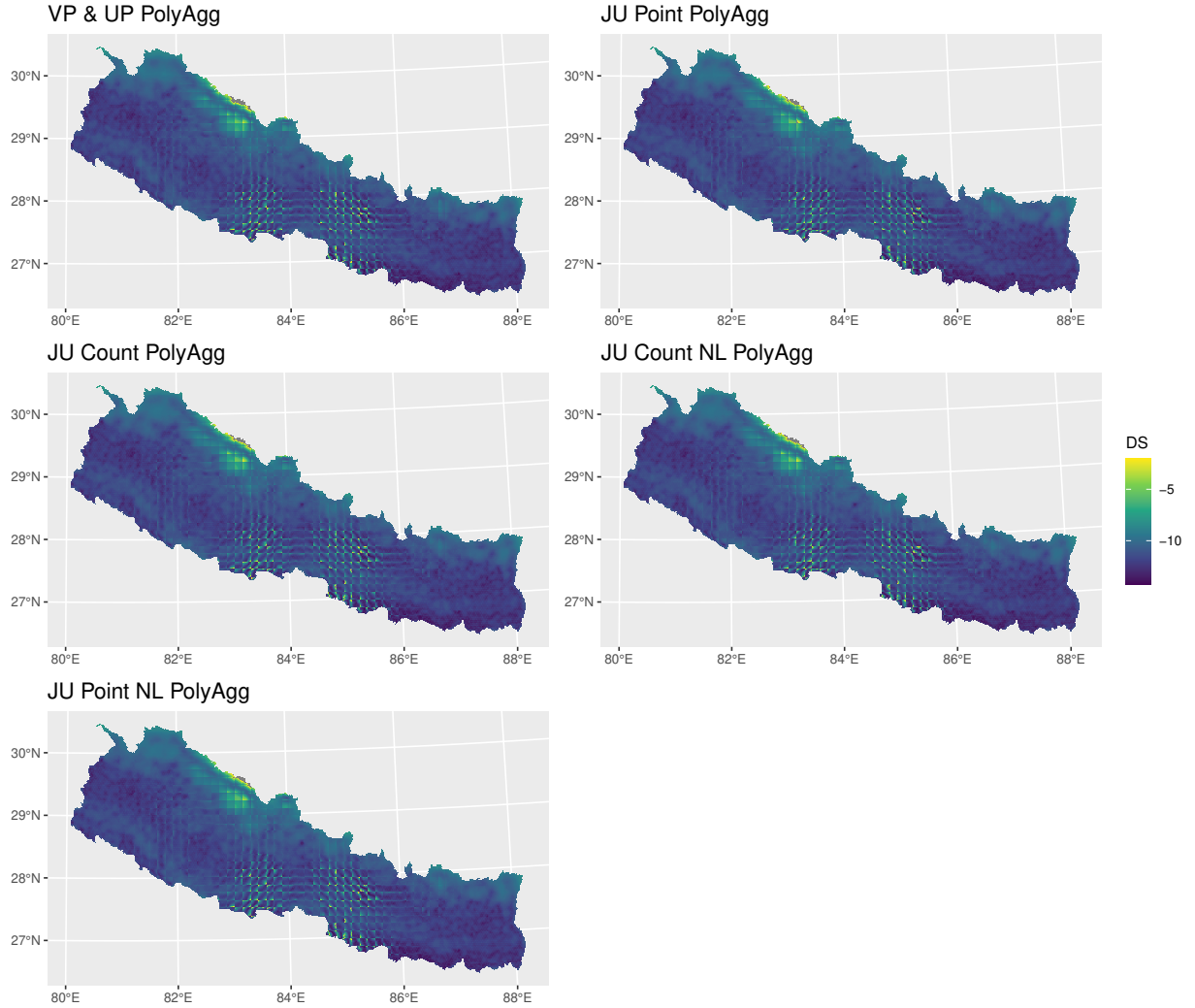


Figure 23: Dawid-Sebastiani (DS) score for the covariate field  $X$  across the models under incomplete covariate field scenario with observed noises  $\sigma_{\epsilon_x}$  (truncated at 0). JU: Joint Uncertainty, VP: Value Plugin, UP: Uncertainty Plugin, Point: Observed Point, Count: Aggregated Count, PolyAgg: Polygon Aggregation.

## C.10 Computation Time

Here refers to Sections 5.2.4 and 5.2.5 to compare the computation time across different models.

All numerical experiments for the case study/simulation were performed limited to 10 threads

on a Four Intel Xeon E5-2680 v3 2.5GHz, 30M Cache, 9.6 GT/s QPI 192 GB RAM machine (i.e. 48 cores in total and 2 threads each core).

Model name	Description	Time (sec)
fit_pts	Point RastFull	413.67
fit_pts_agg	Point RastAgg	387.74
fit_pts_poly	Point PolyAgg	412.79
fit_count	Count RastFull	1223.40
fit_agg	Count RastAgg	1327.17
fitly	Count PolyAgg	1383.79
fit_icov_sd01	VP and UP point+count NL PointVal	474.51
fit_ap	VP and UP PolyAgg	973.82
fit_ic_pts_sd01	JU Point PointVal	5373.32
fit_ic_sd01	JU Count PointVal	6549.09
fit_ic_ap_pts	JU Point PolyAgg	10479.75
fit_ic_ap	JU Count PolyAgg	13643.07
fit_ic_pts_sd01_nl	JU Point NL PointVal	4822.12
fit_ic_sd01_nl	JU Count NL PointVal	4950.74
fit_ic_ap_pts_nl	JU Point NL PolyAgg	5374.53
fit_ic_ap_nl	JU Count NL PolyAgg	8100.82
fit_icov2_pts_sd01	VP Point PointVal	335.58
fit_icov2_sd01	VP Count PointVal	475.57
fit_icov2_ap_pts	VP Point PolyAgg	421.68
fit_icov2_ap	VP Count PolyAgg	487.53
fit_icov2_pts_nl_sd01	VP Point NL PointVal	308.22
fit_icov2_nl_sd01	VP Count NL PointVal	609.28
fit_icov2_ap_pts_nl	VP Point NL PolyAgg	286.63
fit_icov2_nl_ap	VP Count NL PolyAgg	613.25
fit_icov3_pts_sd01	UP Point PointVal	1540.68
fit_icov3_sd01	UP Count PointVal	2899.59
fit_icovap_pts	UP Point PolyAgg	2255.58
fit_icovap	UP Count PolyAgg	3189.34
fit_icov3_pts_nl_sd01	UP Point NL PointVal	2605.85
fit_icov3_nl_sd01	UP Count NL PointVal	2840.81
fit_icovap_nl	UP Point NL PolyAgg	3485.97
fit_icovap_pts_nl	UP Count NL PolyAgg	3670.17

Table 5: Table of computation times for different models. JU: Joint Uncertainty, VP: Value Plugin, UP: Uncertainty Plugin, Point: Observed Point, Count: Aggregated Count, PointVal: Point Values, PolyAgg: Polygon Aggregation.

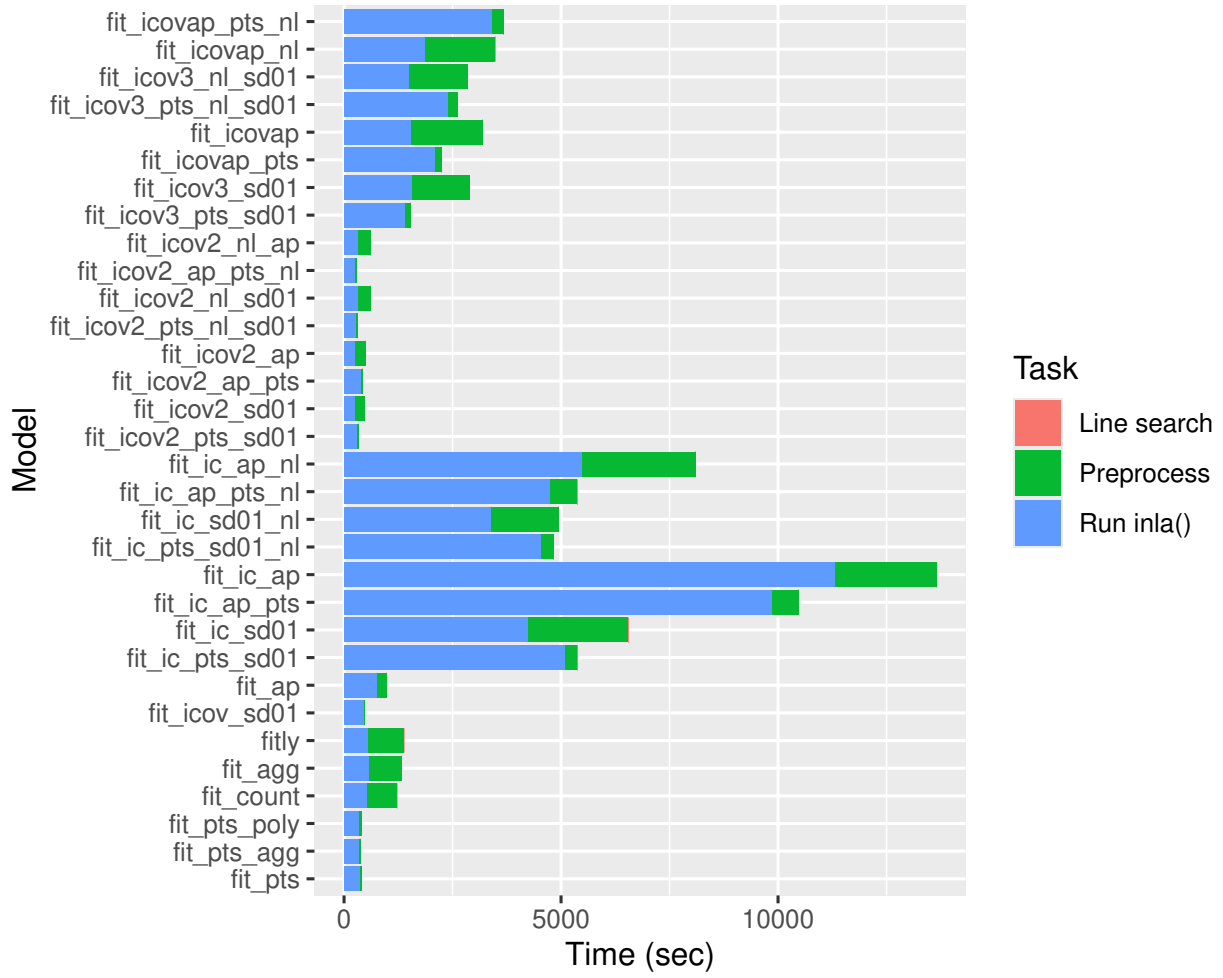


Figure 24: Computation times for different models.

## D Convergence Diagnostic for Linearisation

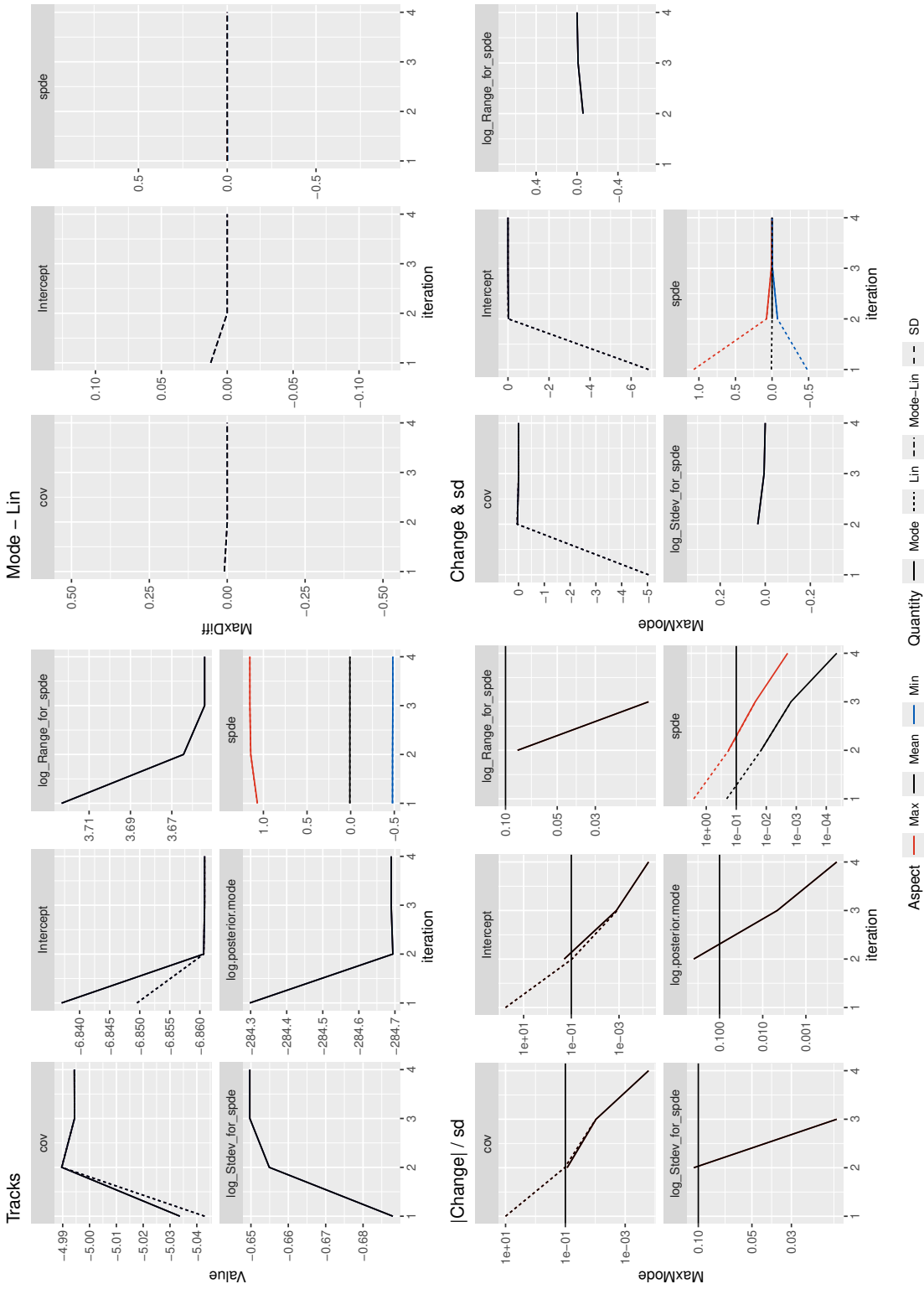
In Section 7.2, we discussed the limitations on convergence iterations. The convergence plots of the models across iterations are shown below. The four panels of convergence diagnostics:

- Tracks: Mode and linearisation values for each effect;
- Mode - Lin: Difference between mode and linearisation values for each effect;
- $|Change|/sd$ : Absolute change in mode and linearisation values divided by the standard deviation for each effect;

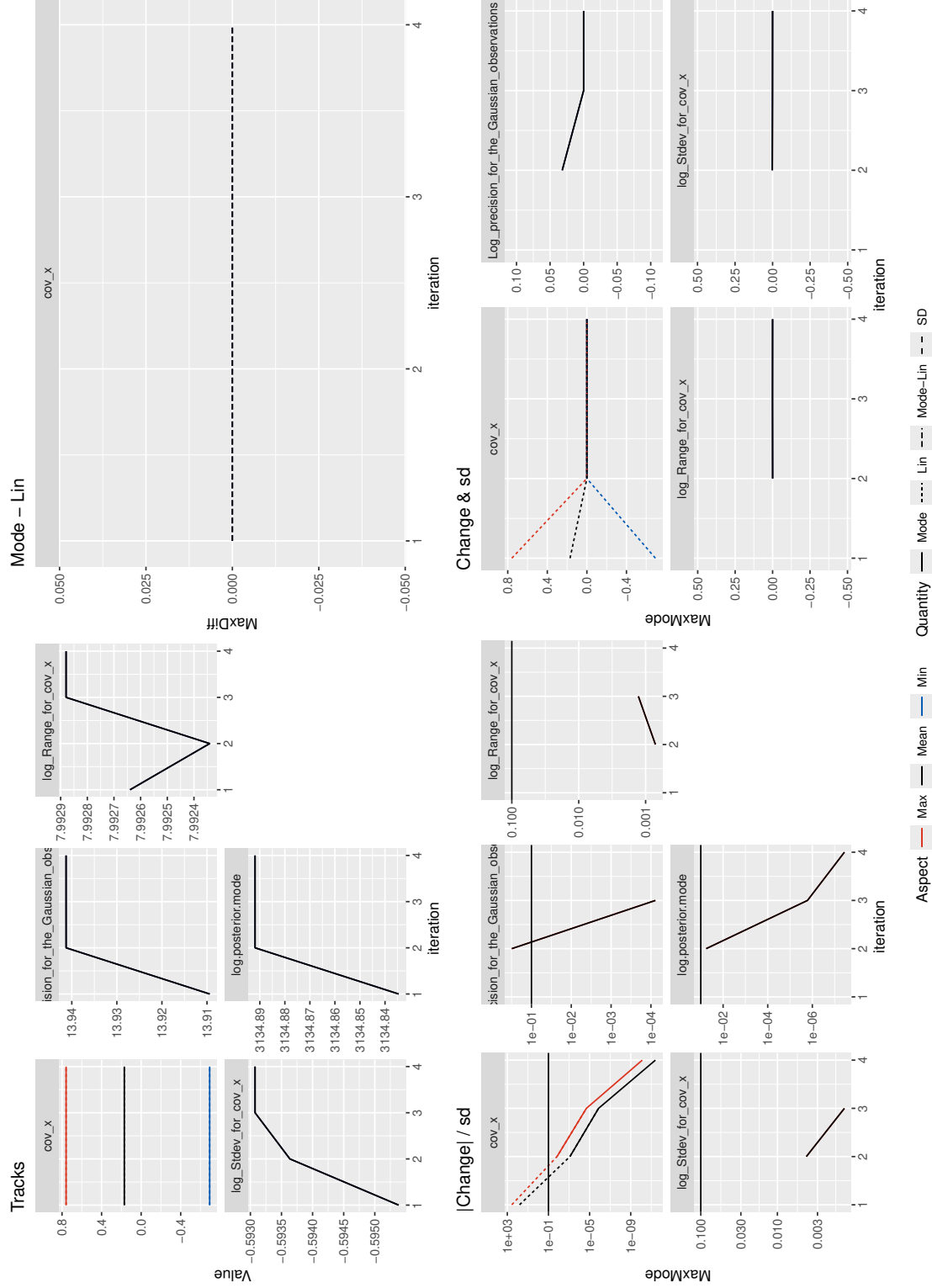
- Change & sd: Absolute change in mode and linearisation values and standard deviation for each effect.

Refer to Table 5 in Appendix C.10 for the model names and descriptions.

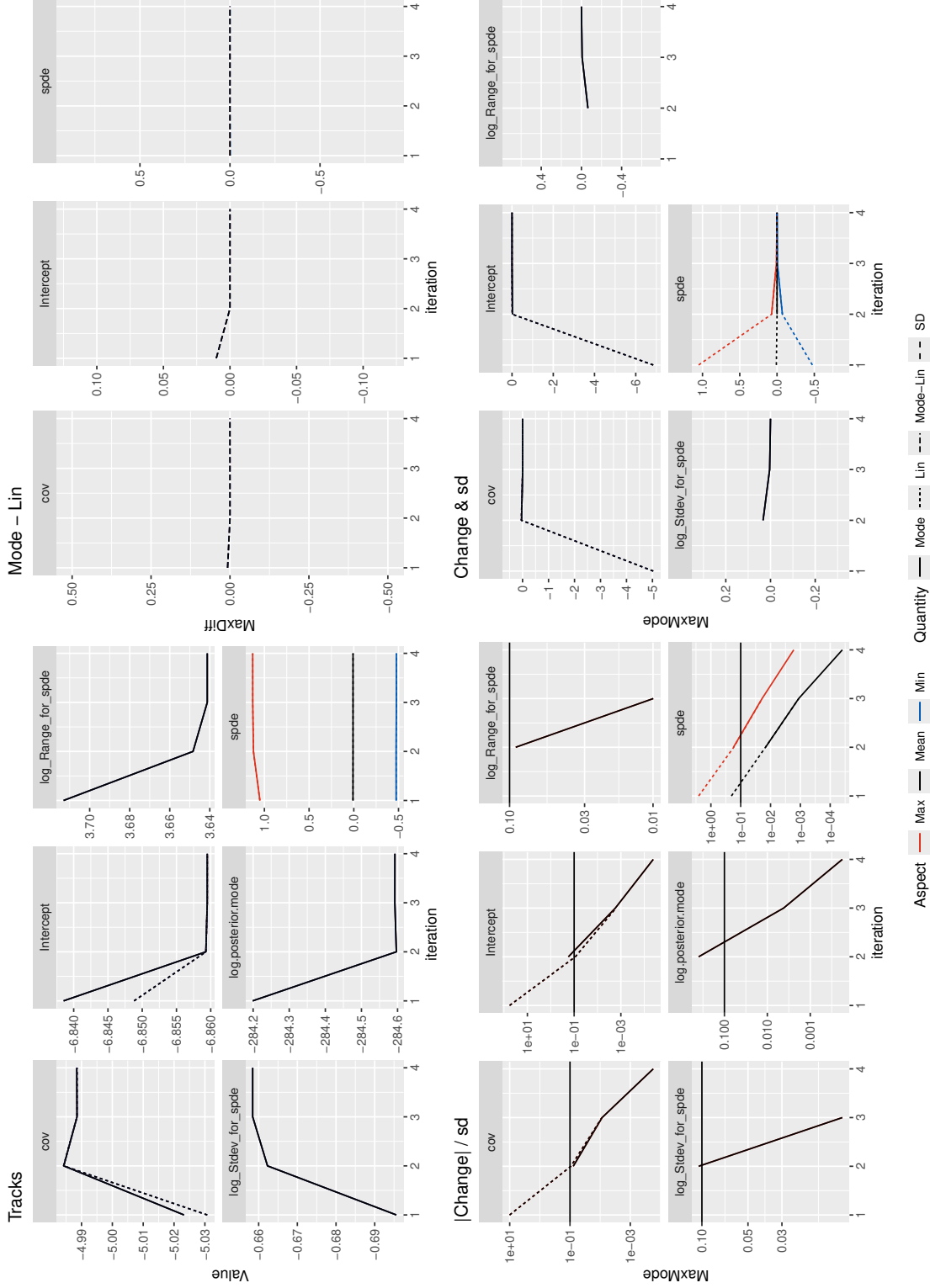
## Convergence plots for fit\_agg



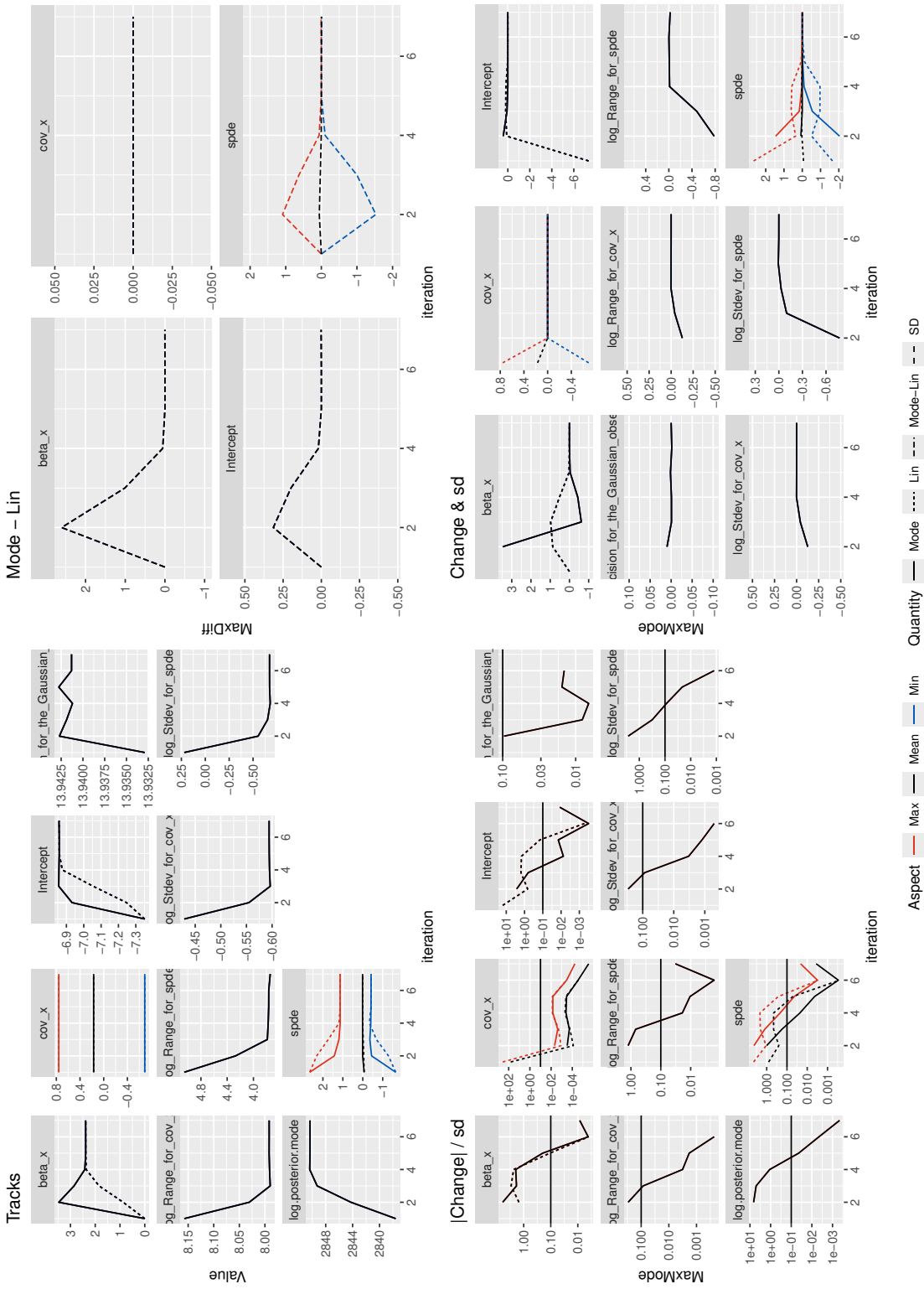
## Convergence plots for fit\_ap



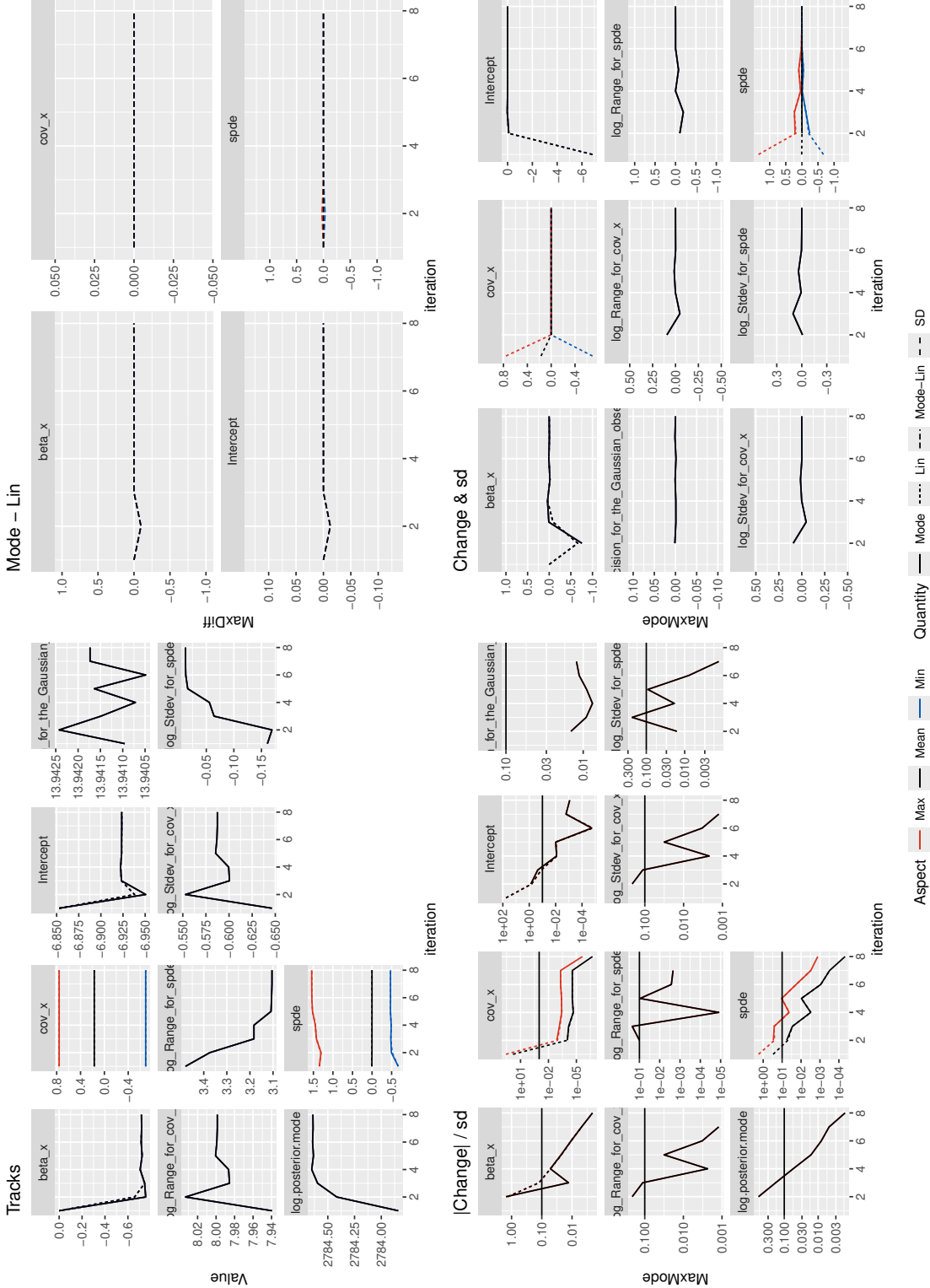
### Convergence plots for fit\_count



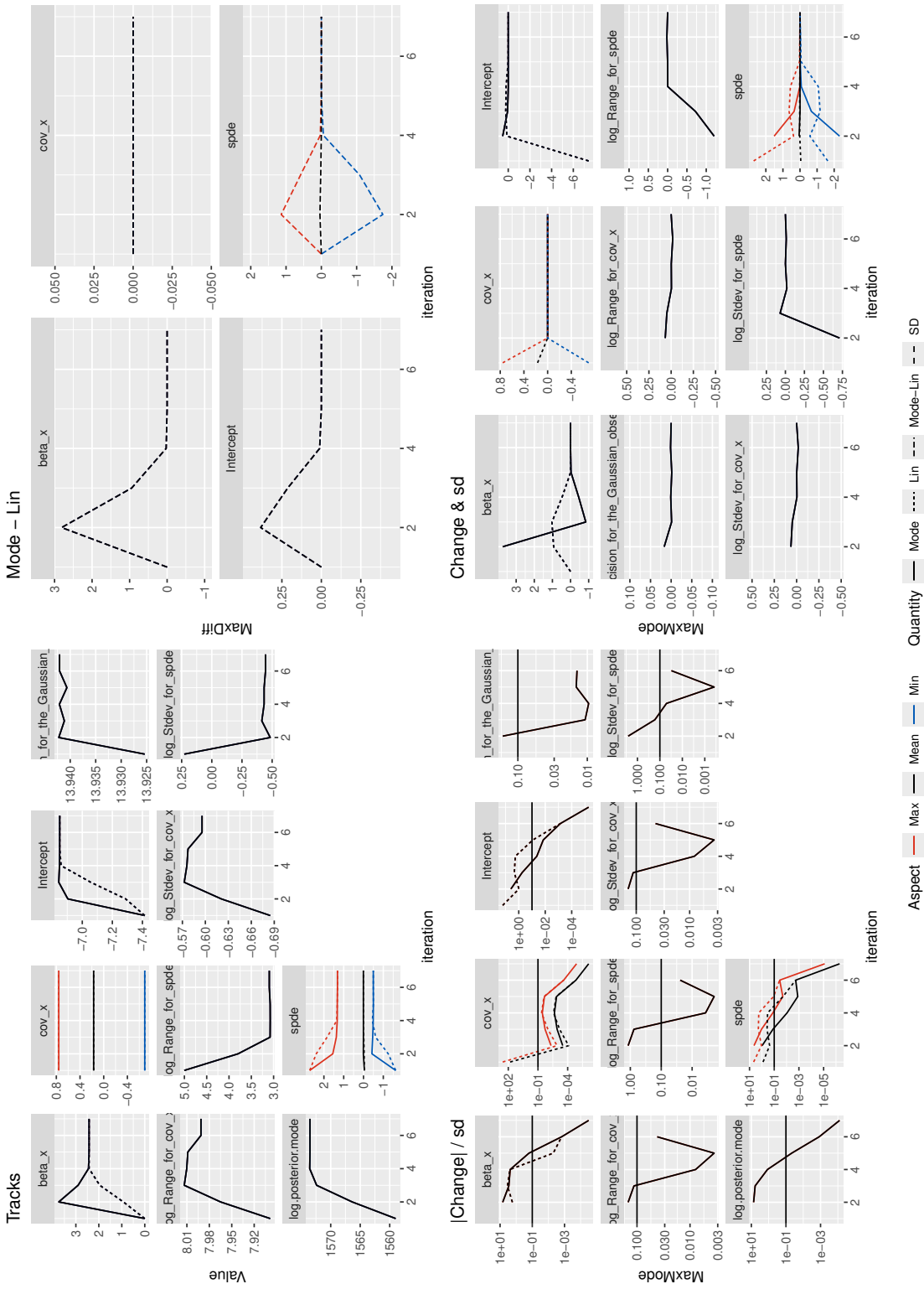
## Convergence plots for fit\_ic\_ap



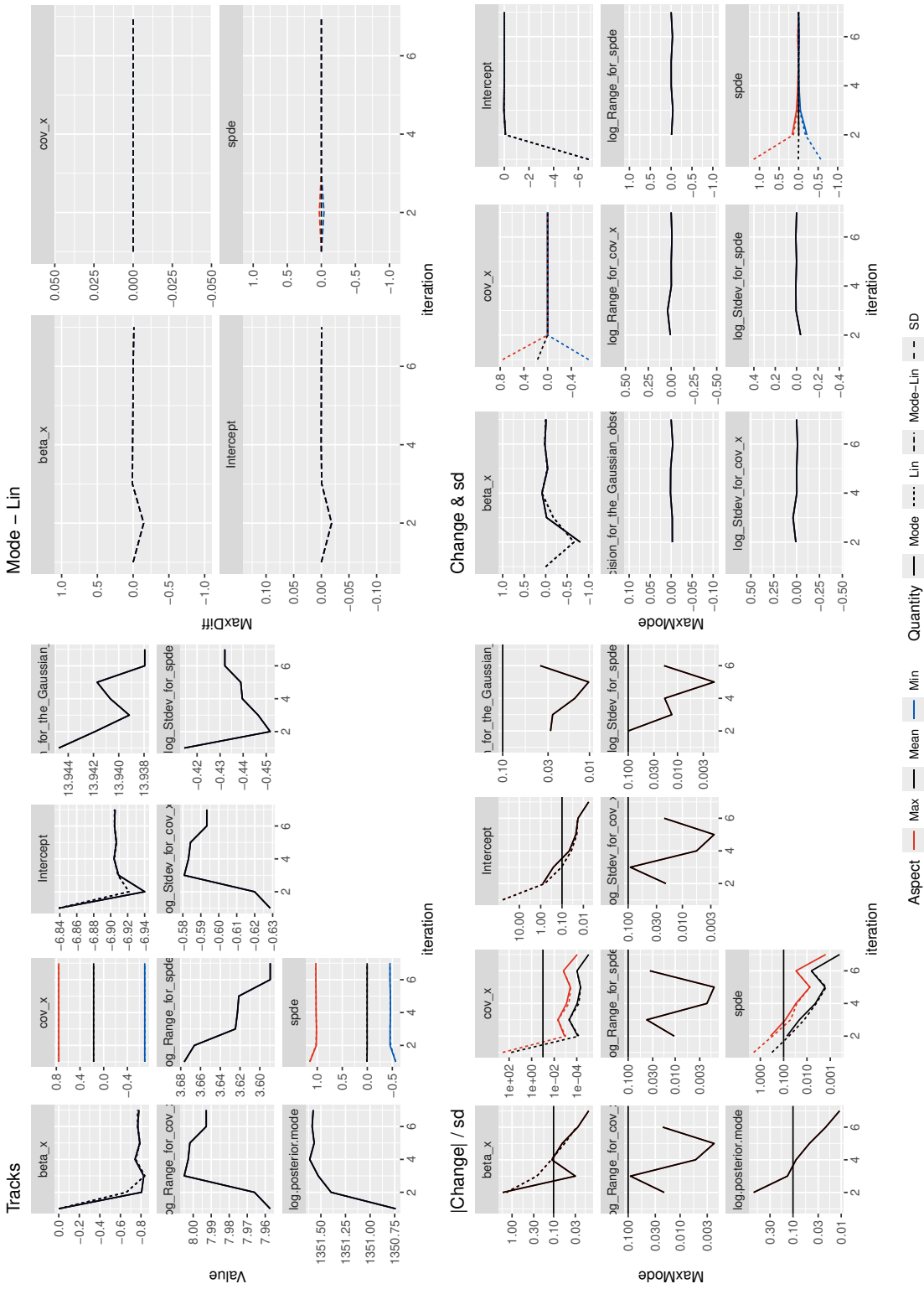
## Convergence plots for fit\_ic\_ap\_nl



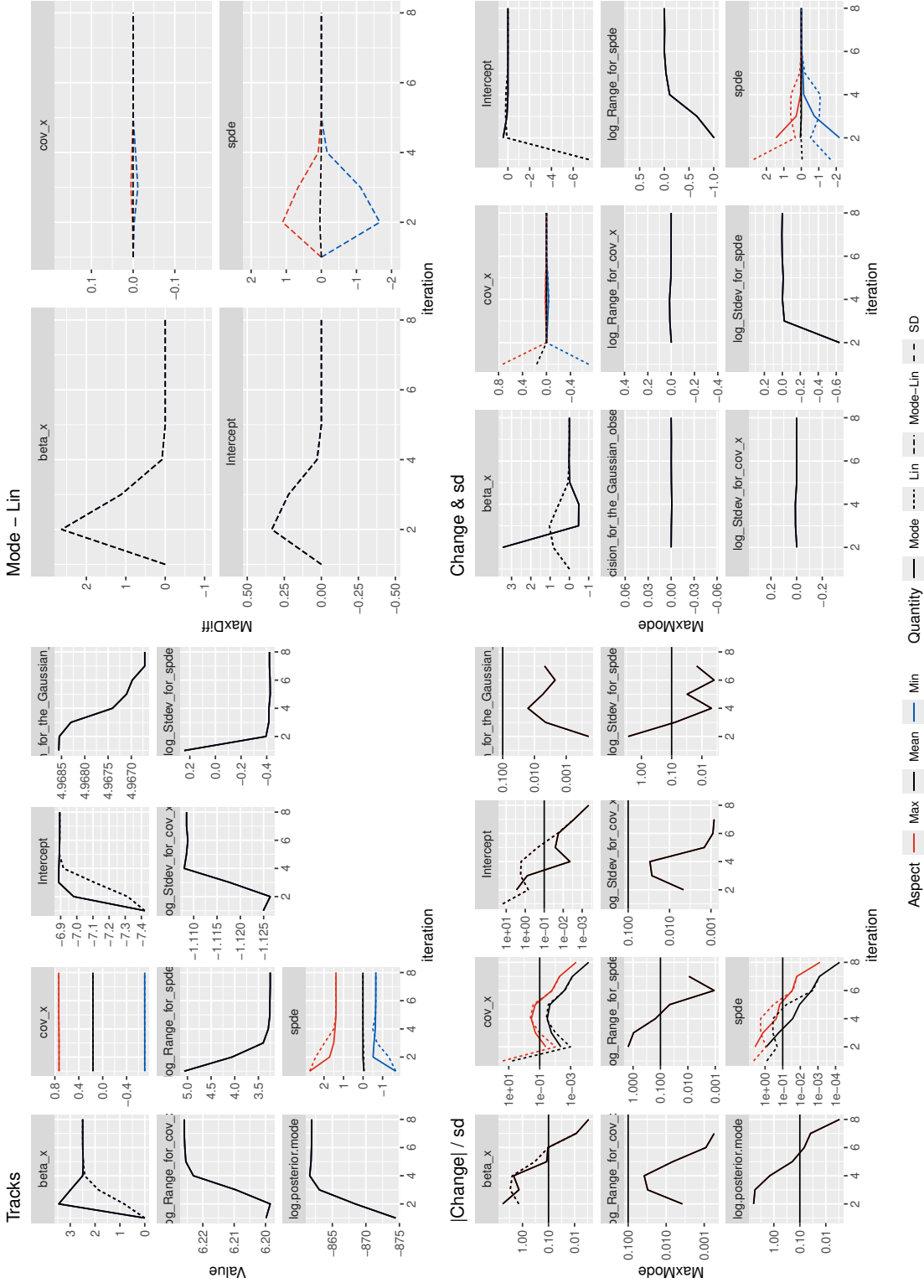
## Convergence plots for fit\_ic\_ap\_pts



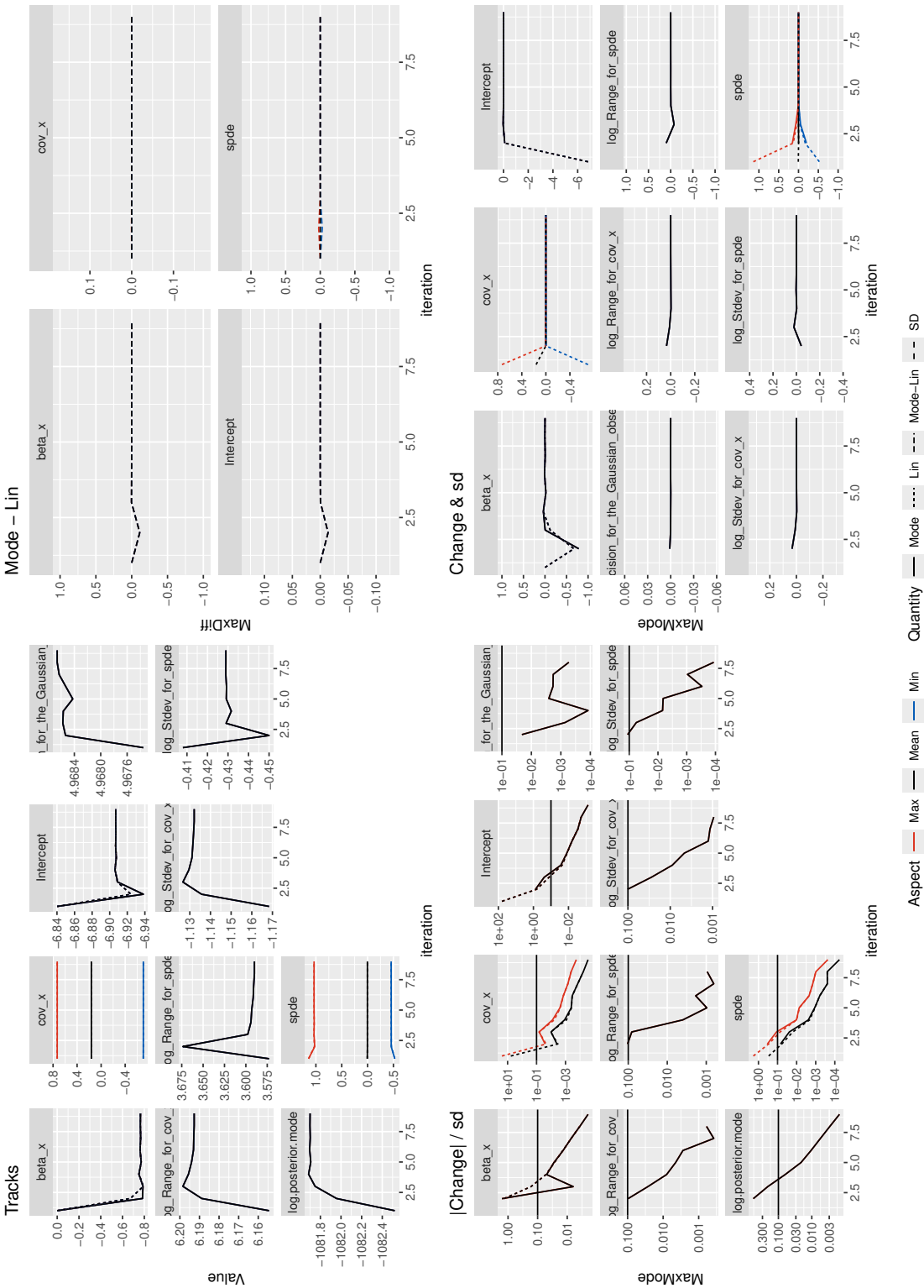
## Convergence plots for fit\_ic\_ap\_pts\_nl



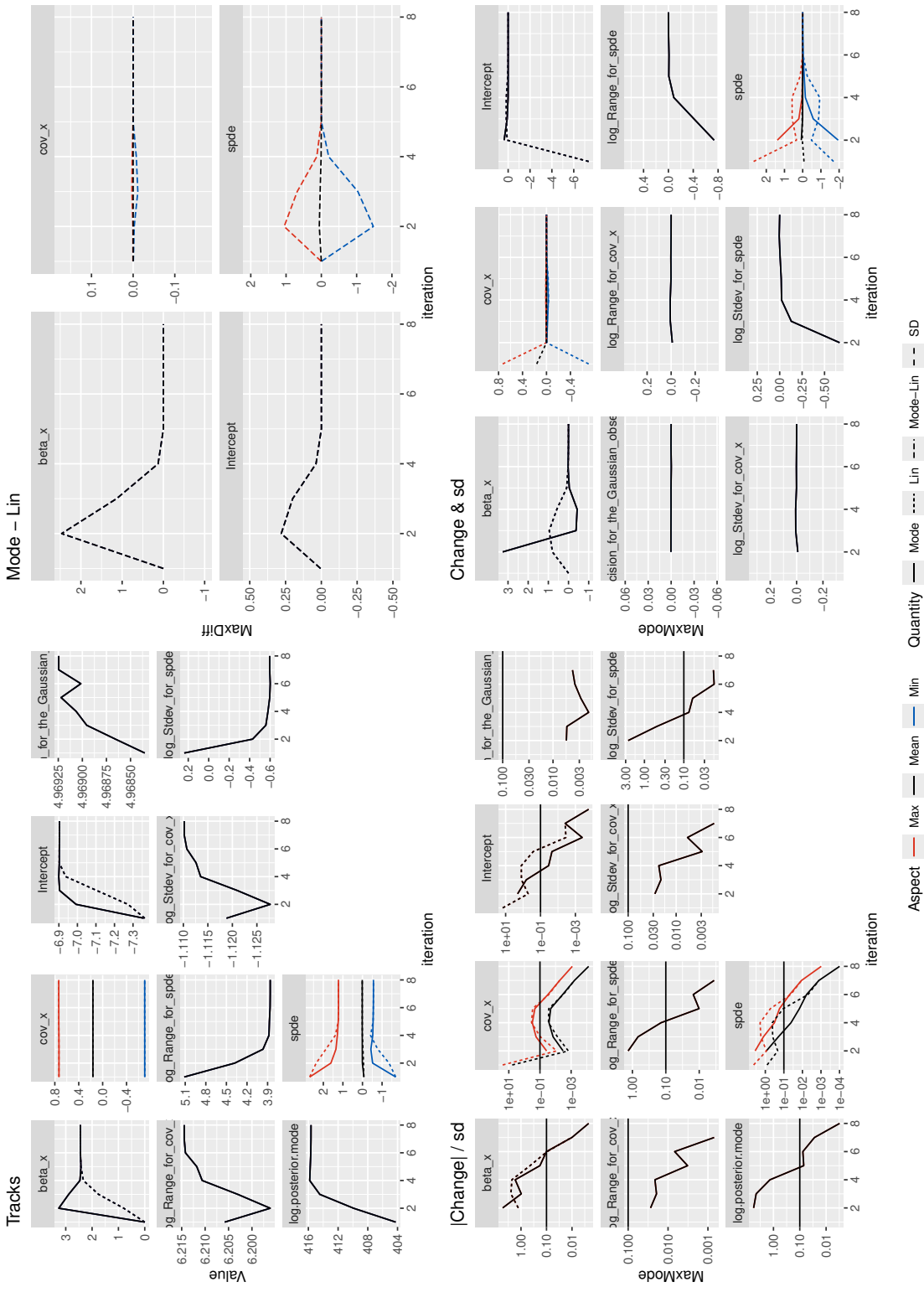
Convergence plots for fit\_ic\_pts\_sd01



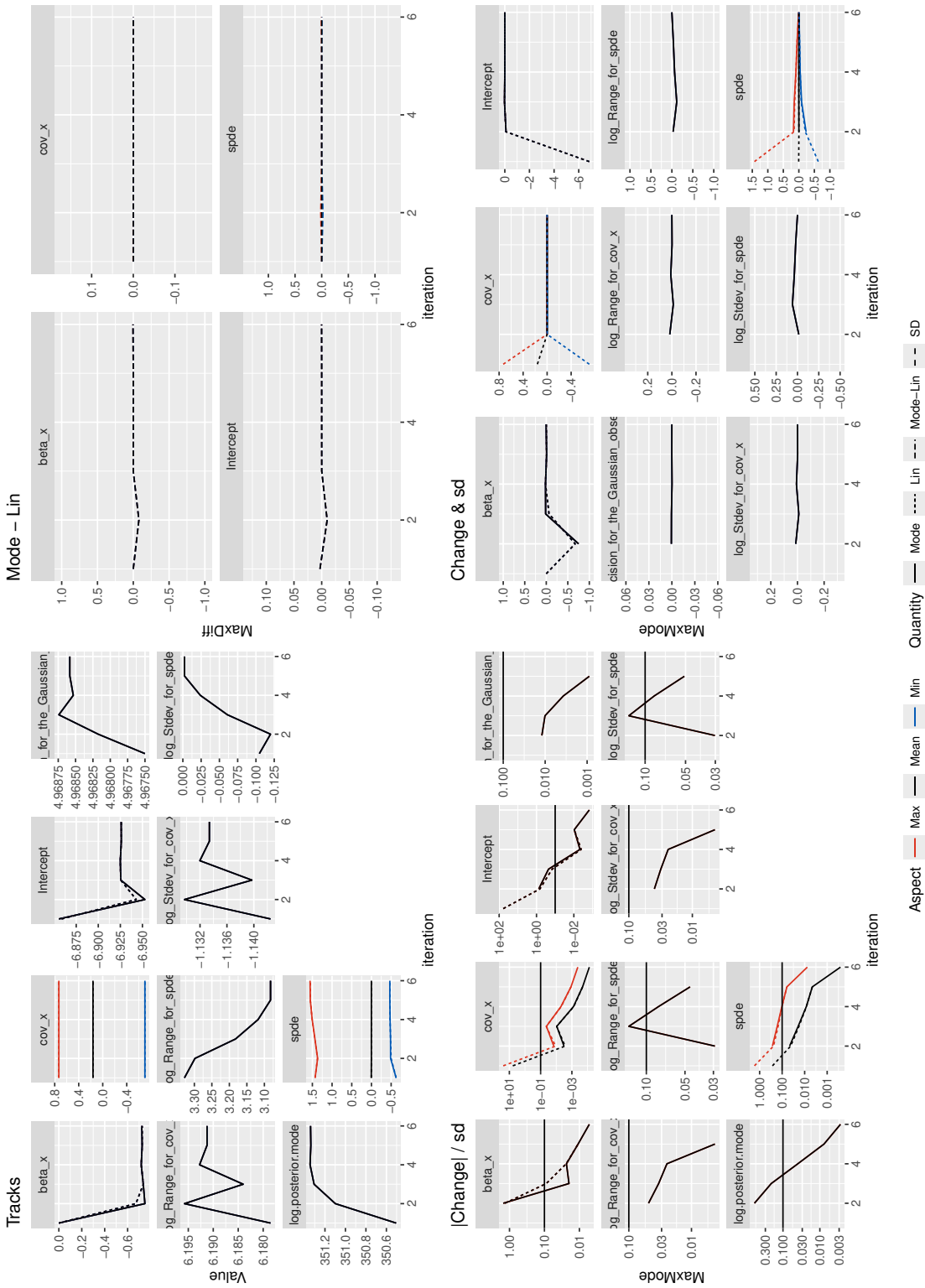
## Convergence plots for fit\_ic\_pts\_sd01\_nl



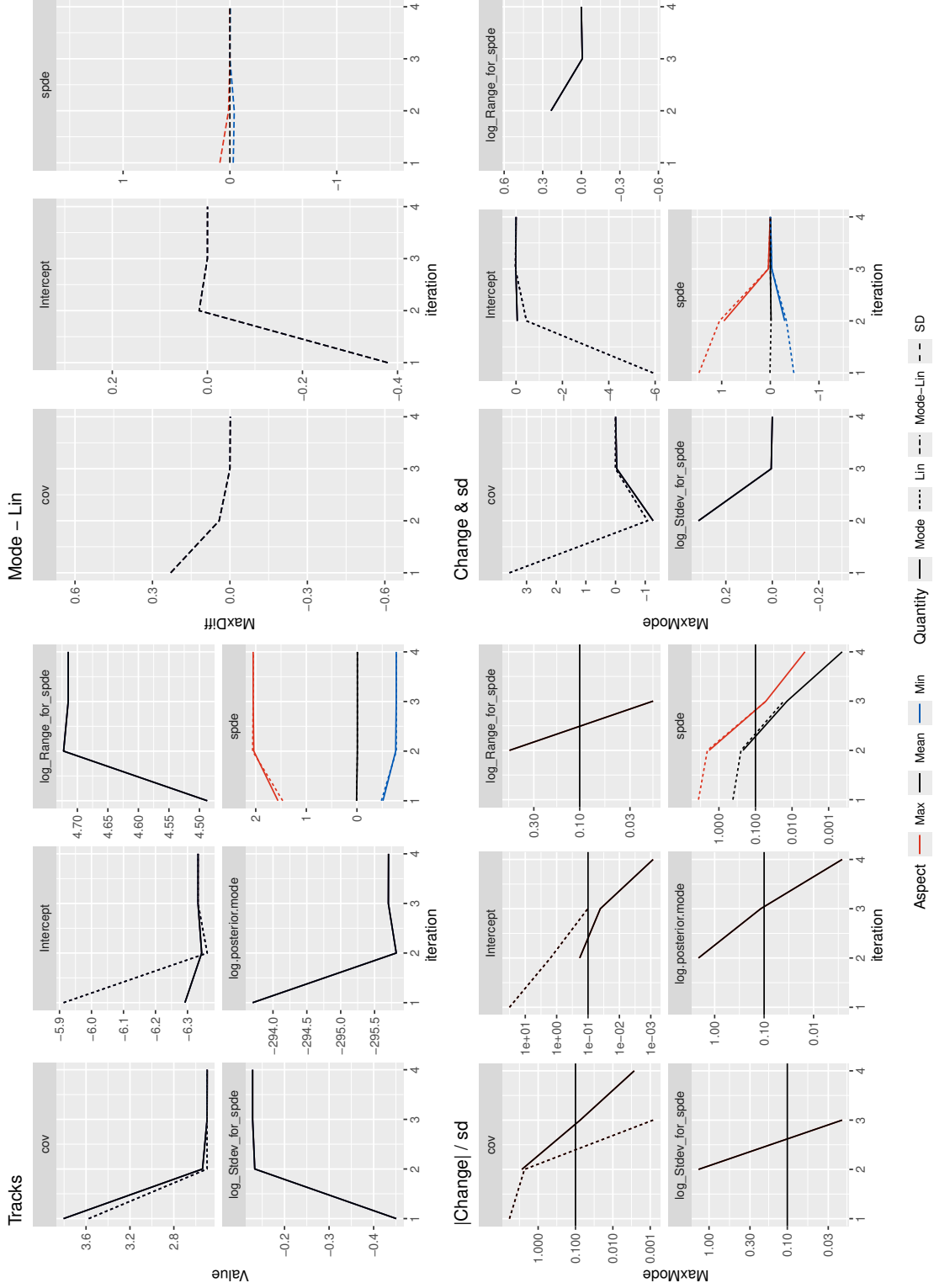
## Convergence plots for fit\_ic\_sd01



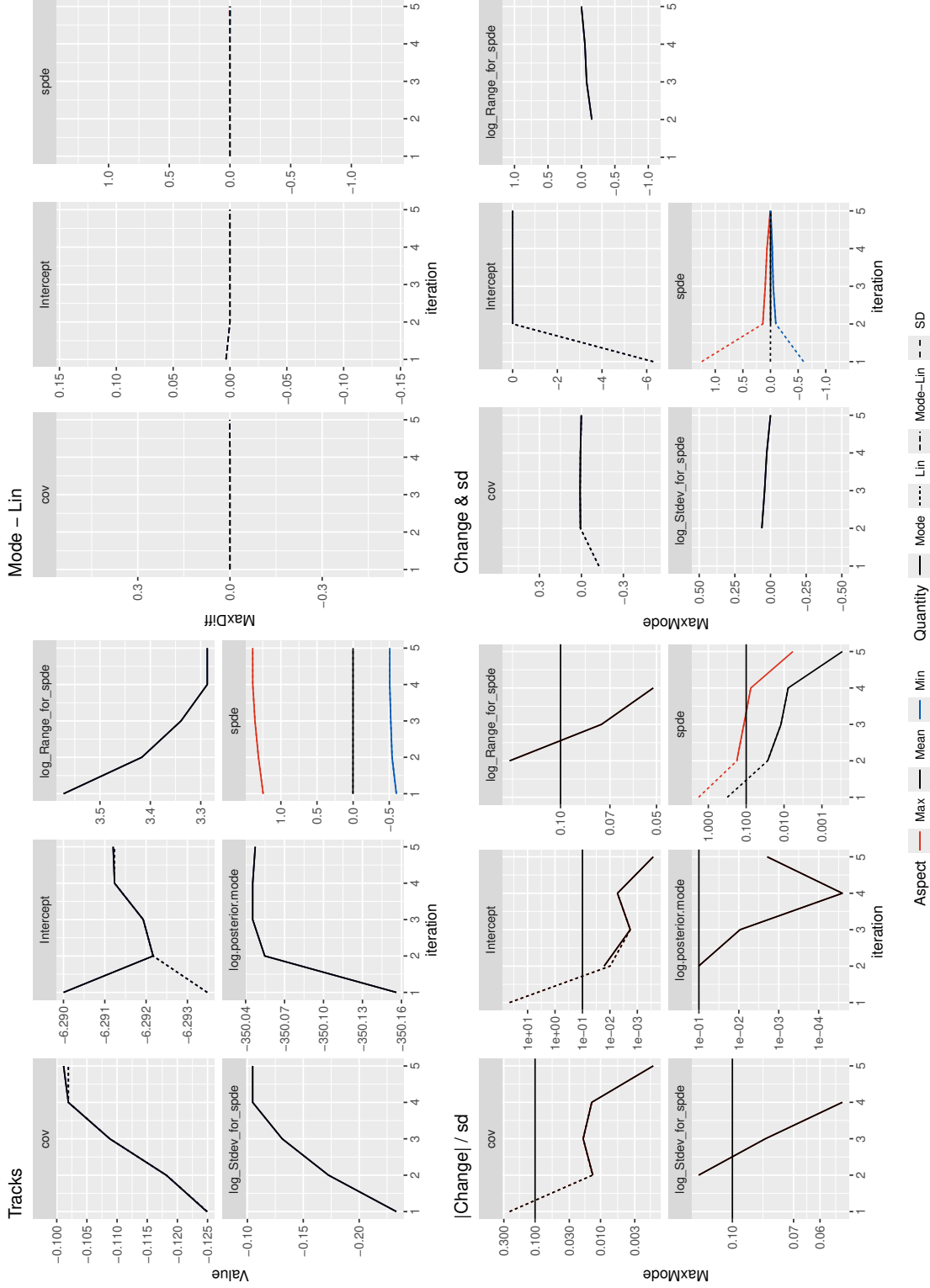
## Convergence plots for fit\_ic\_sd01\_nl



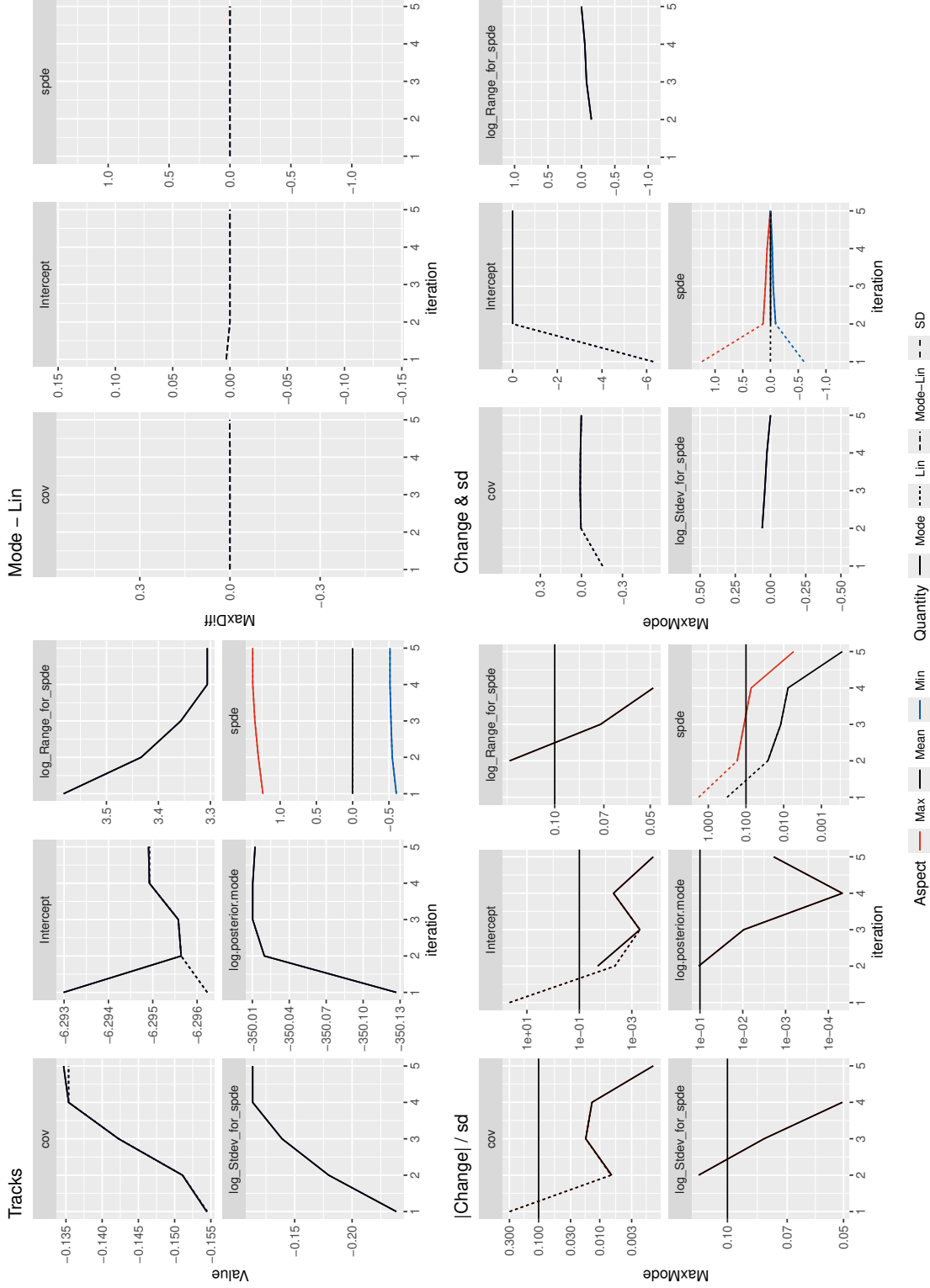
## Convergence plots for fit\_icov2\_ap



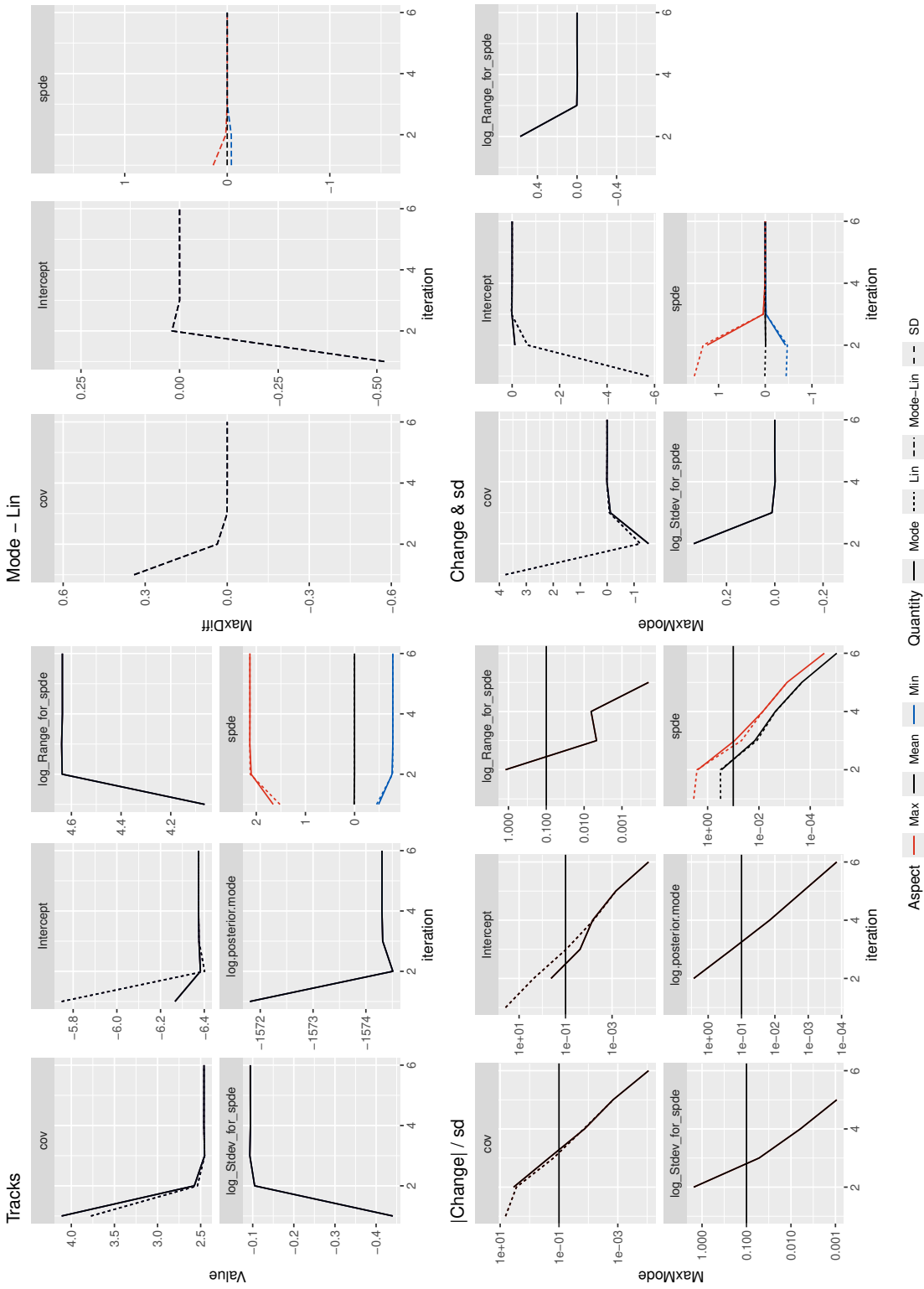
### Convergence plots for fit\_icov2\_nl\_ap



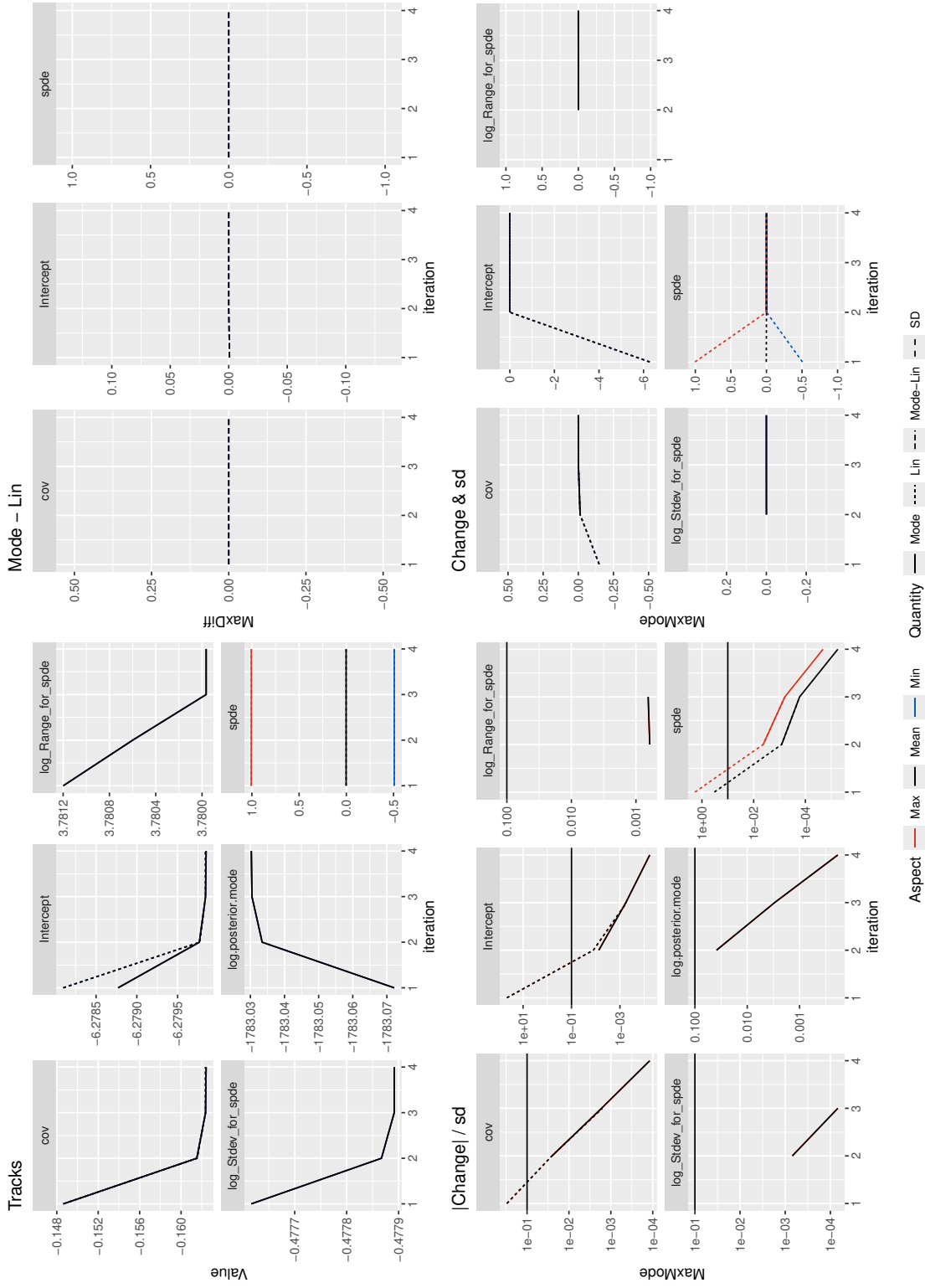
## Convergence plots for fit\_icov2\_nl\_sd01



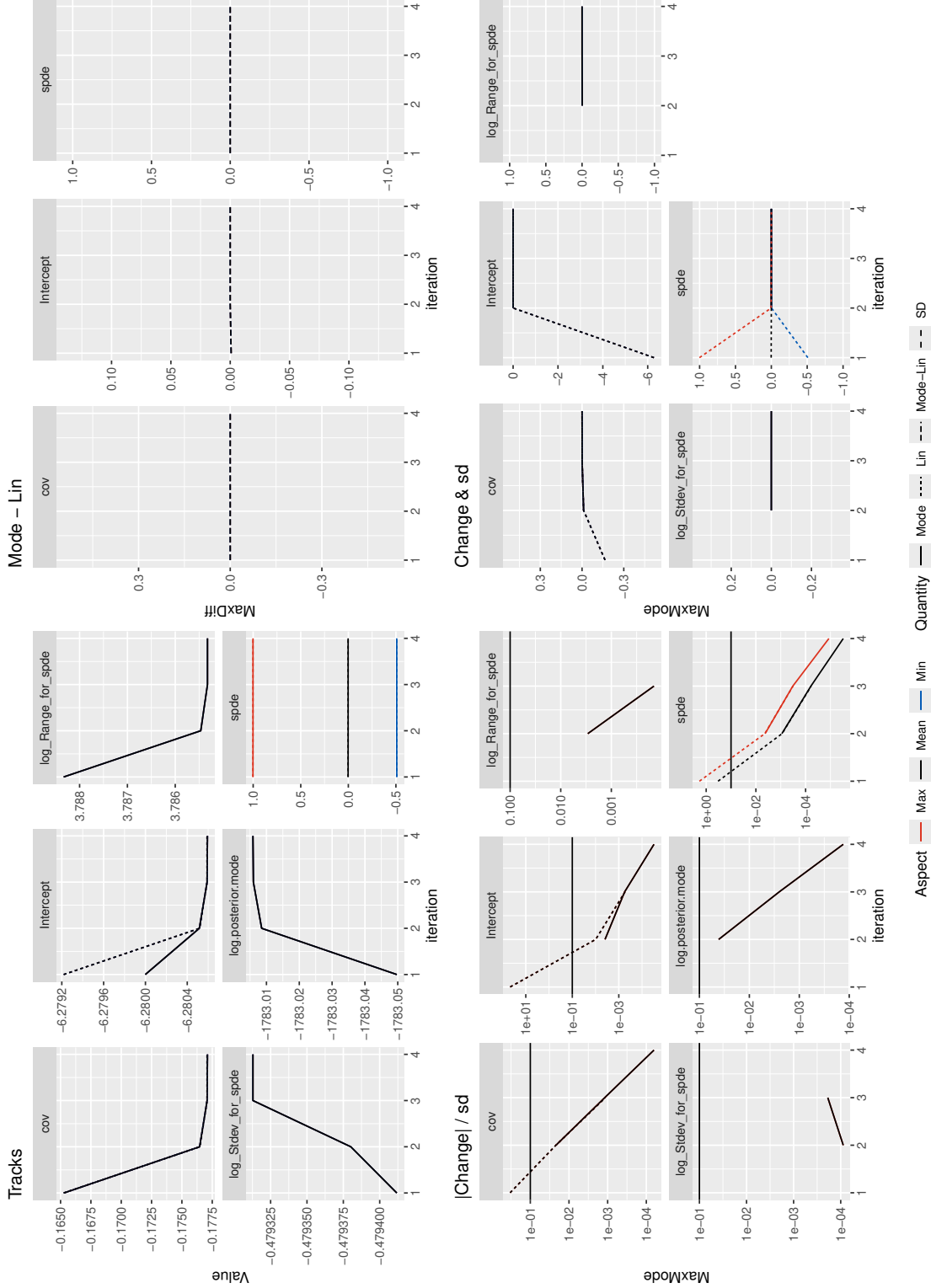
Convergence plots for fit\_icov2\_ap\_pts



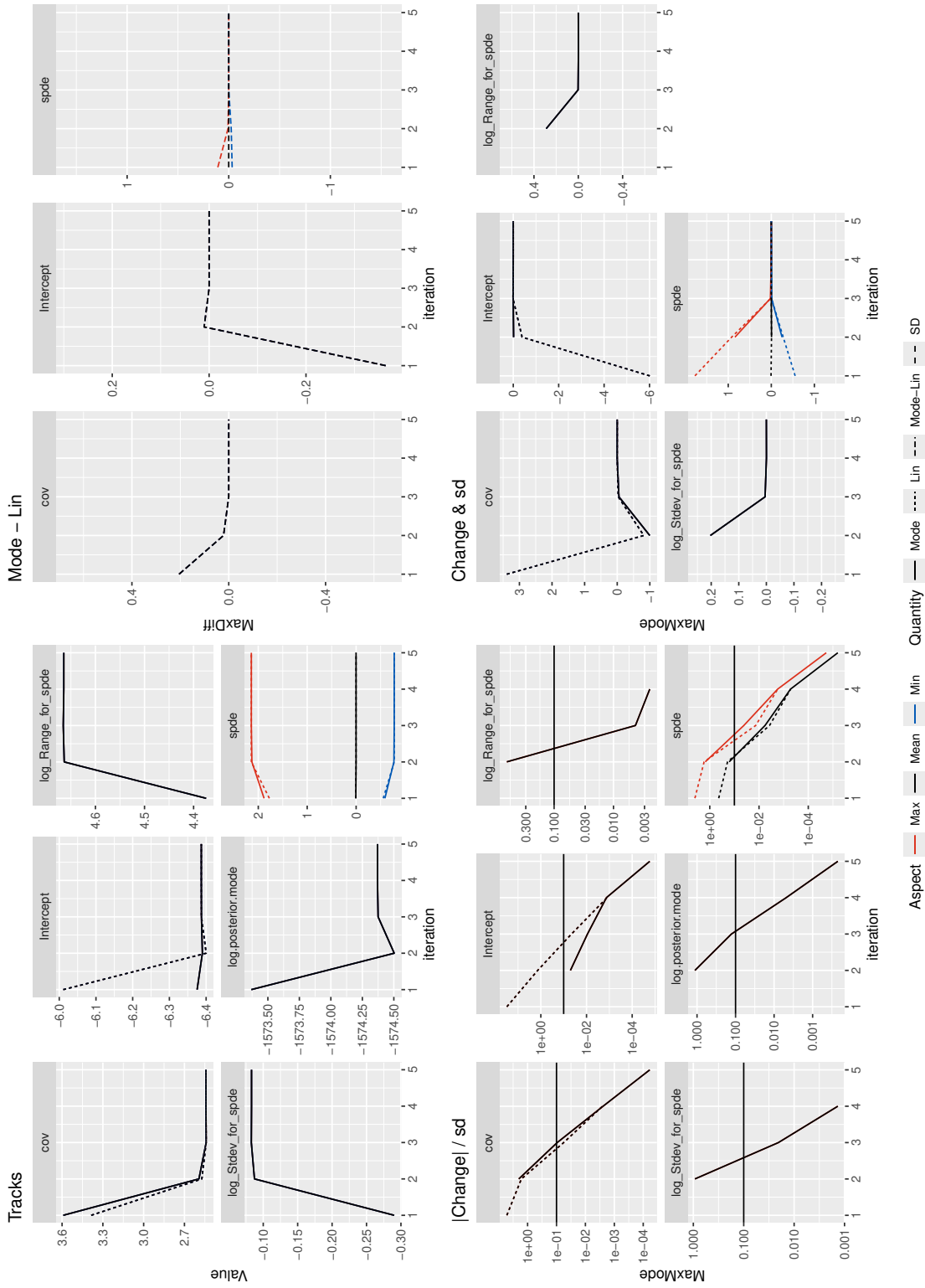
## Convergence plots for fit\_icov2\_ap\_pts\_nl



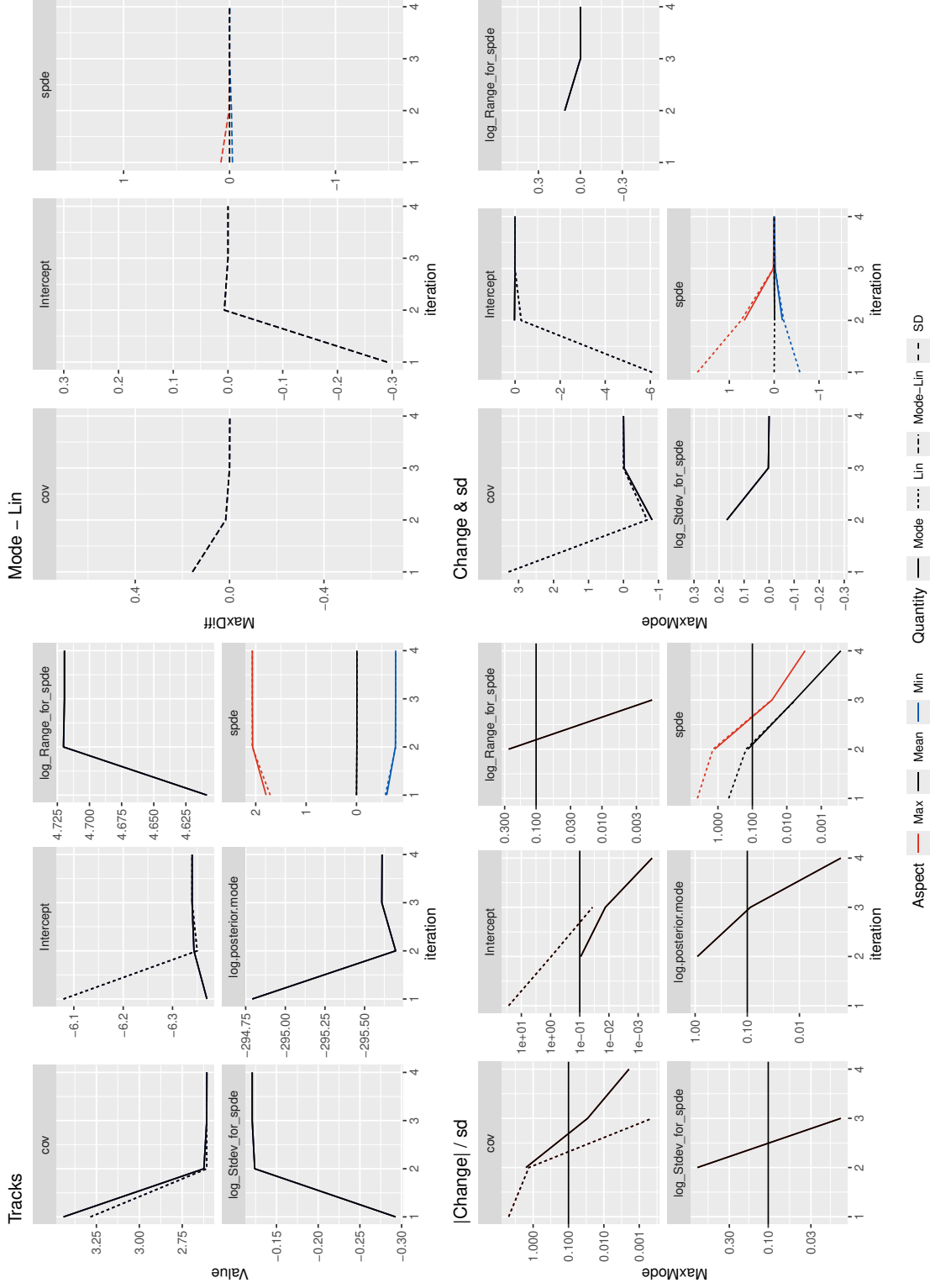
### Convergence plots for fit\_icov2\_pts\_nl\_sd01



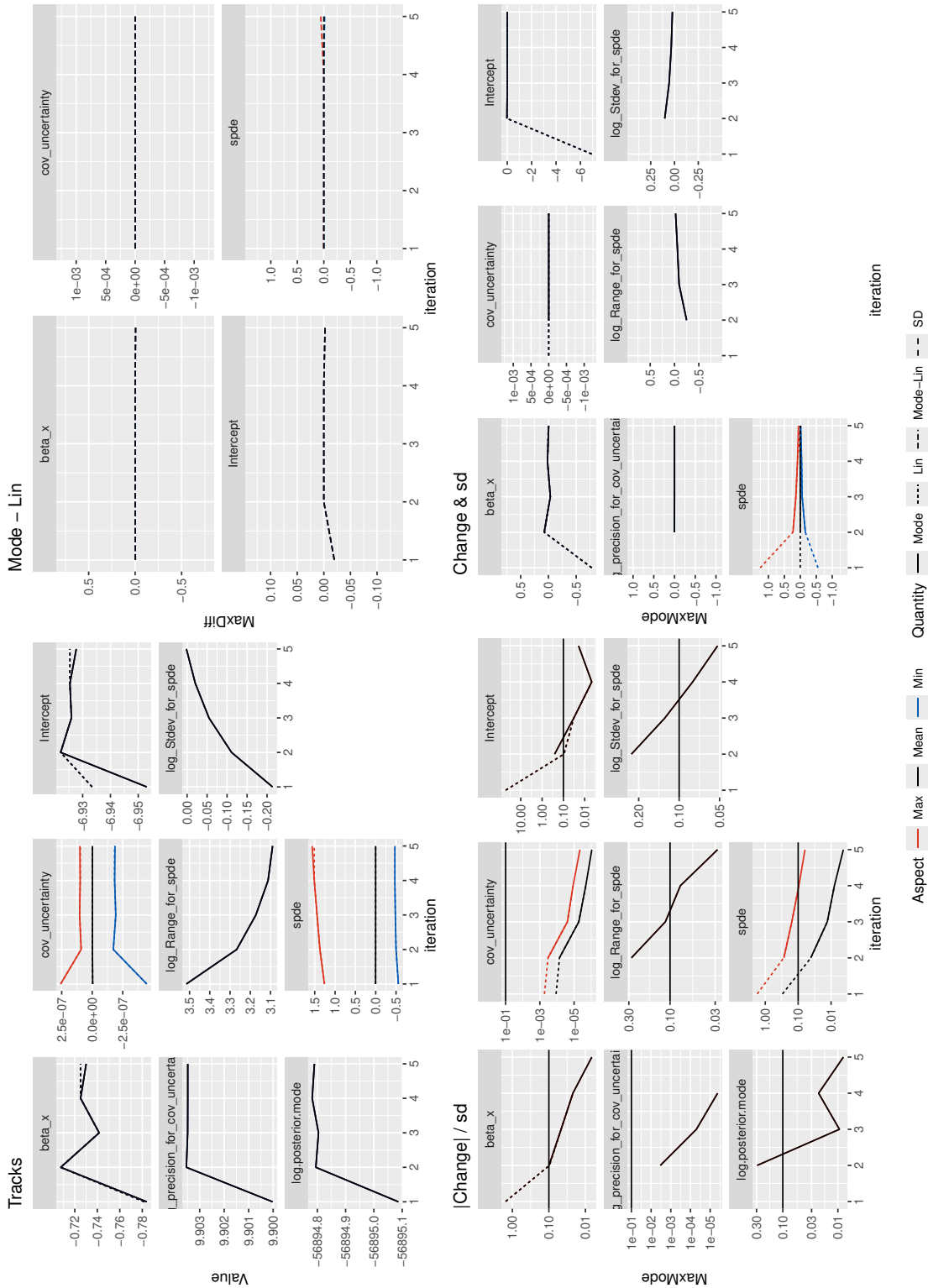
Convergence plots for fit\_icov2\_pts\_sd01



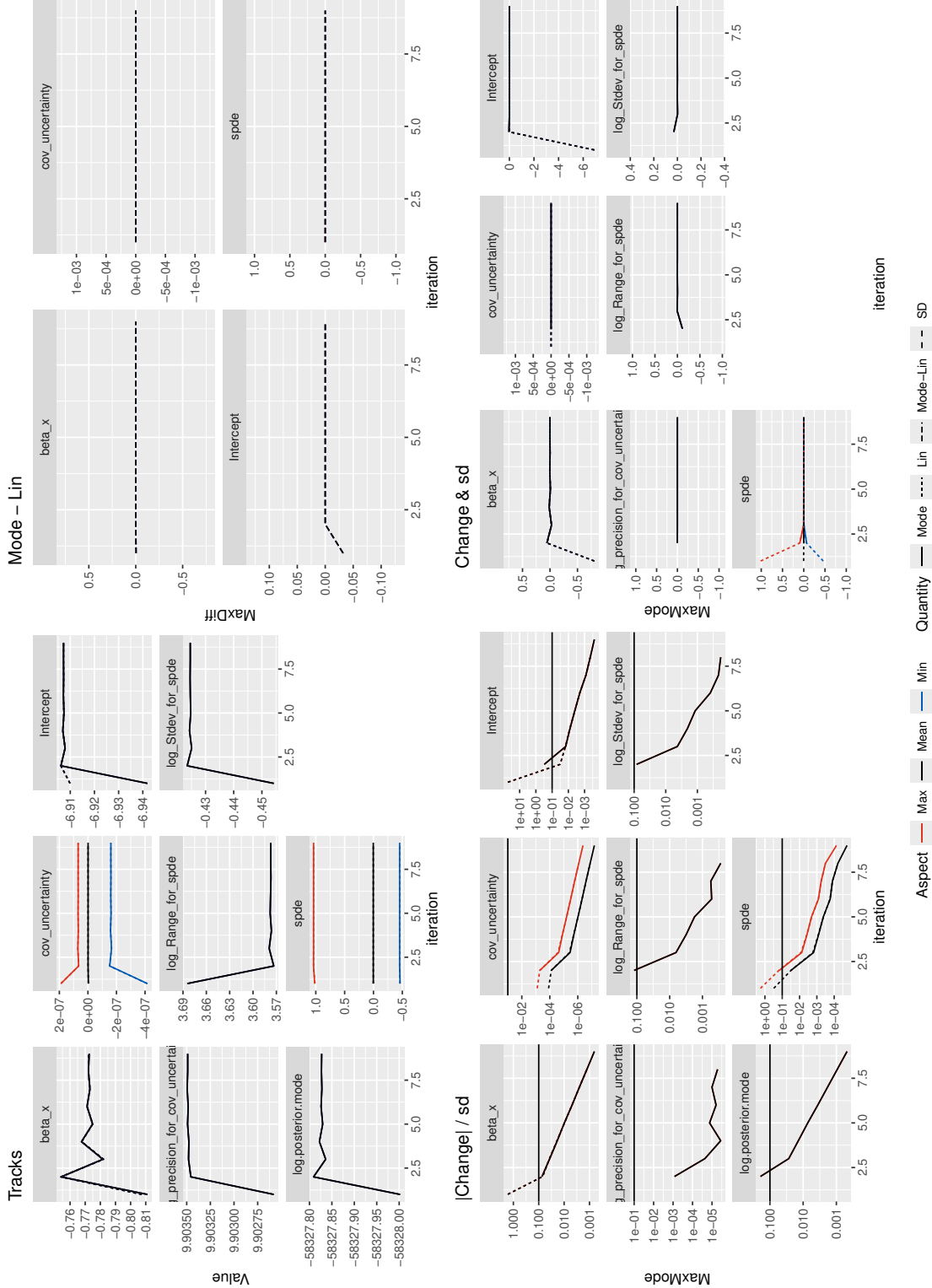
## Convergence plots for fit\_icov2\_sd01



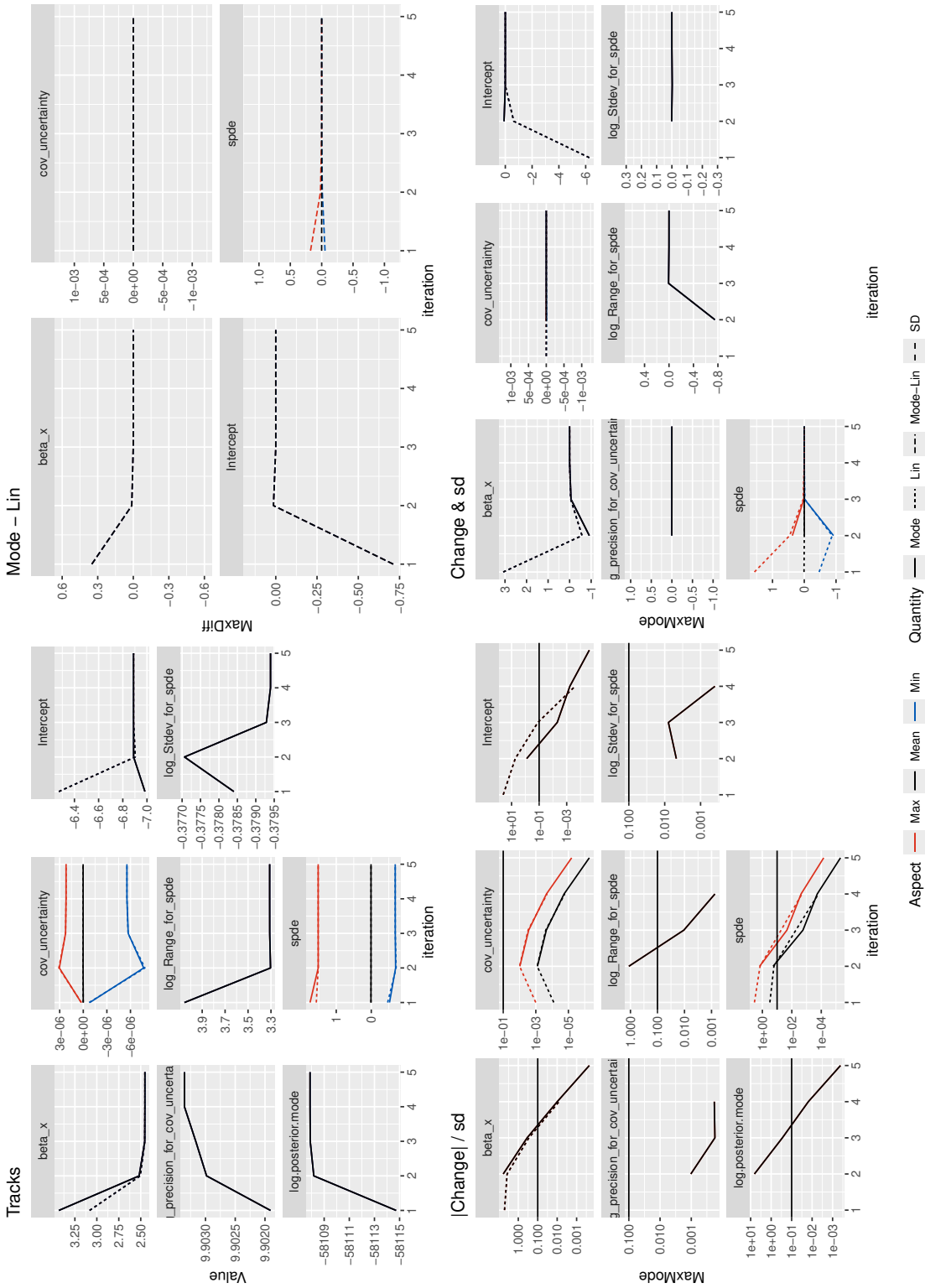
## Convergence plots for fit\_icov3\_nl\_sd01



## Convergence plots for fit\_icov3\_pts\_nl\_sd01

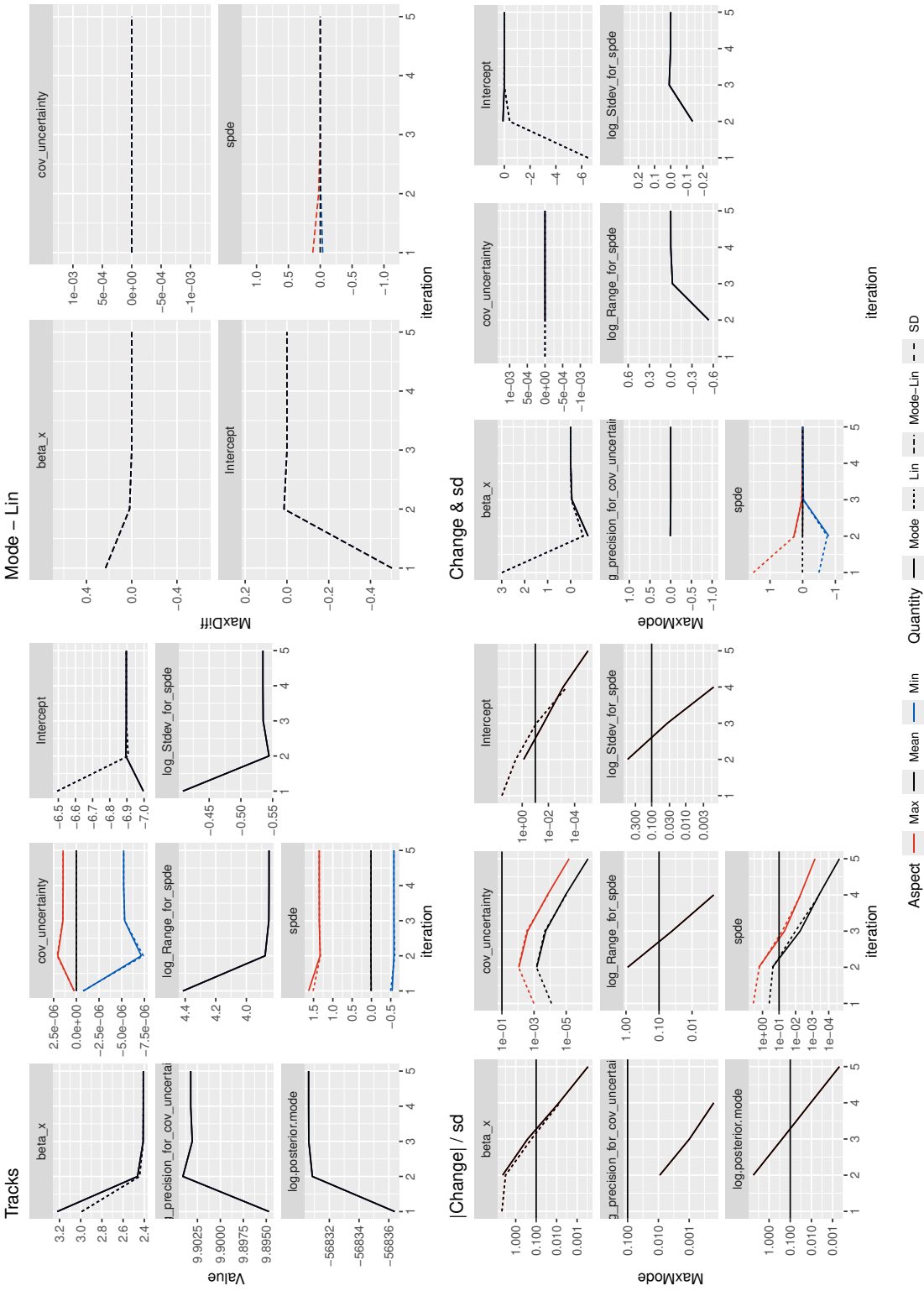


Convergence plots for fit\_icov3\_pts\_sd01

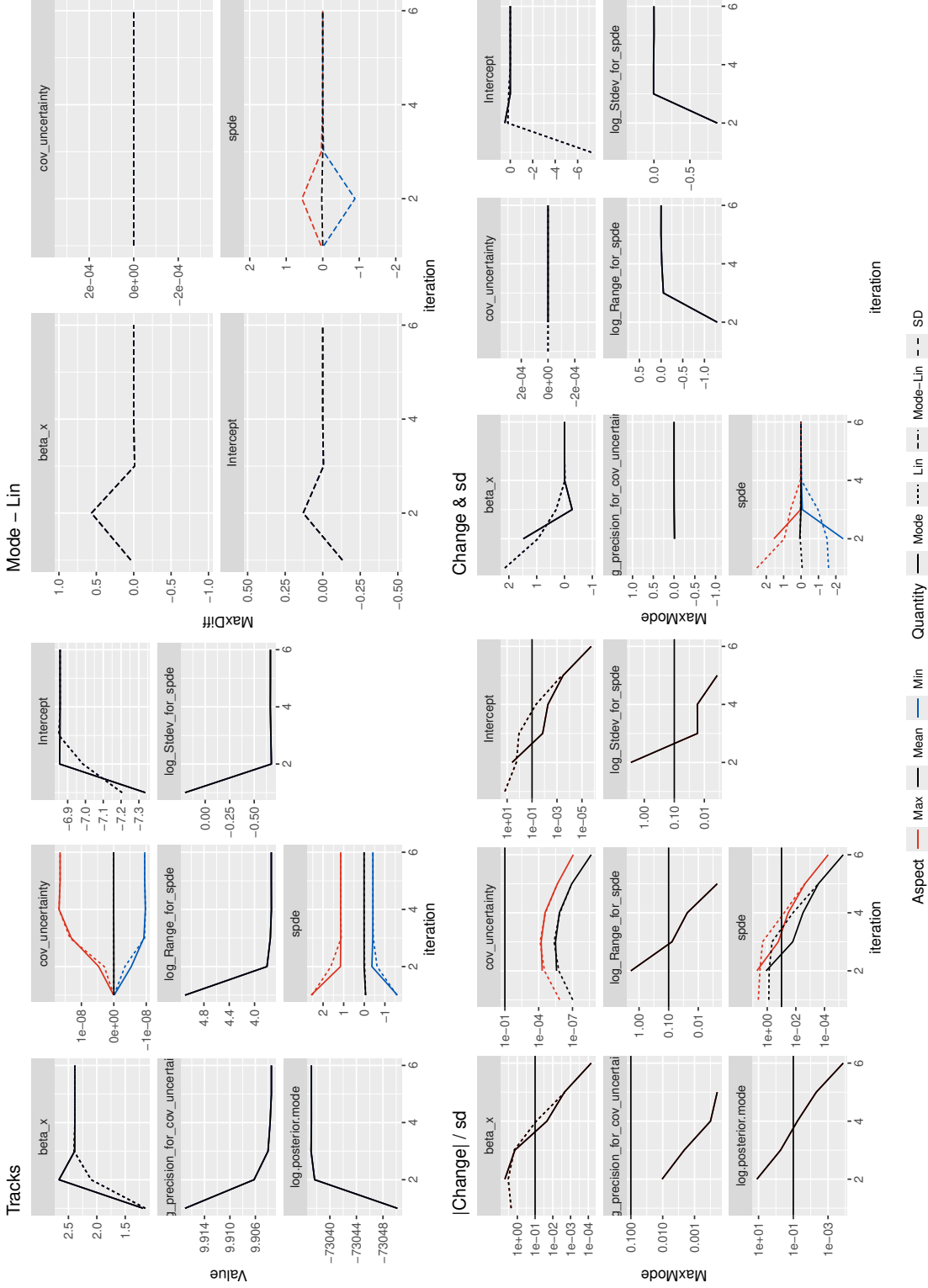


## Convergence plots for fit\_icov3\_sd01

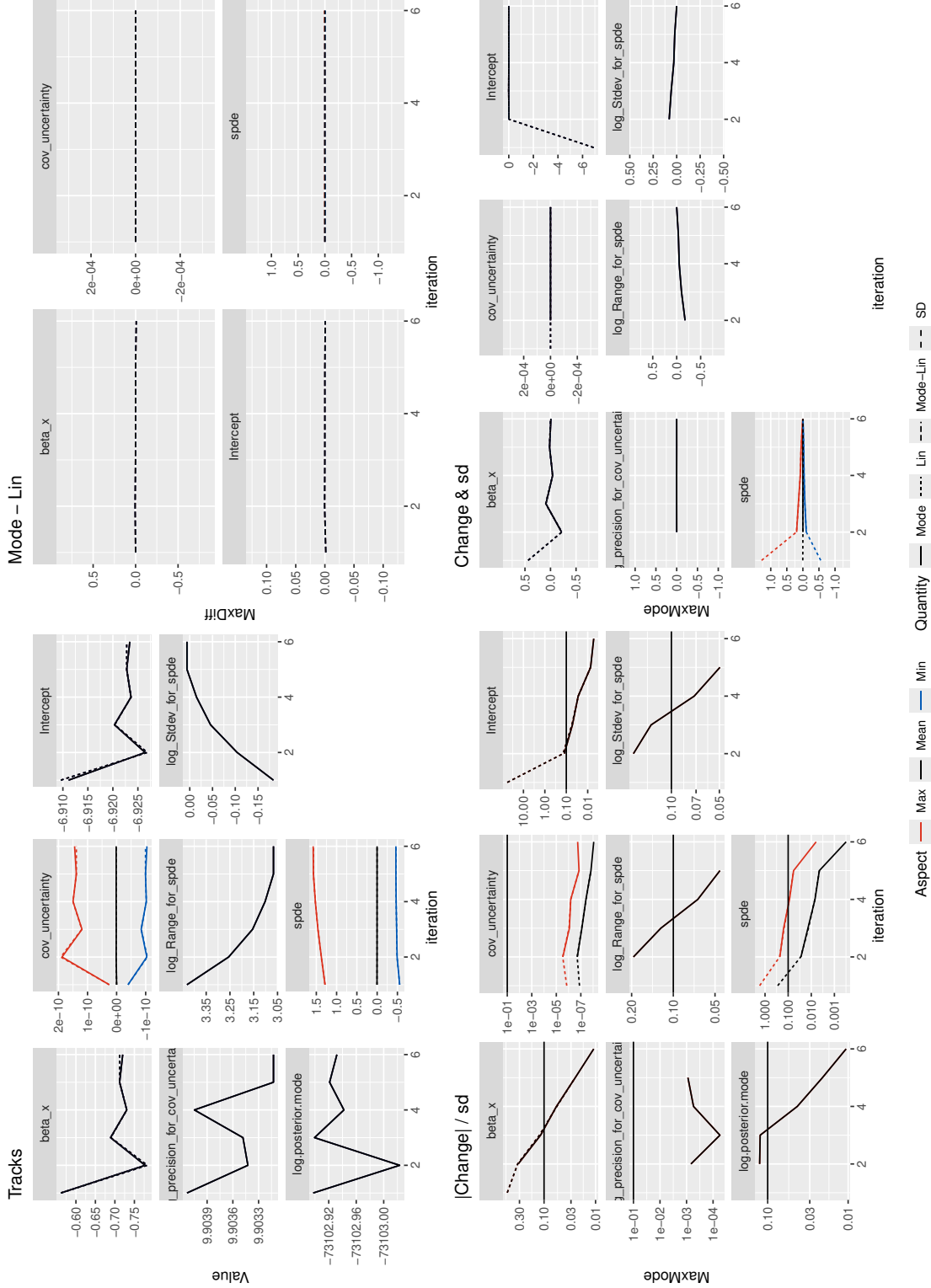
### Tracks



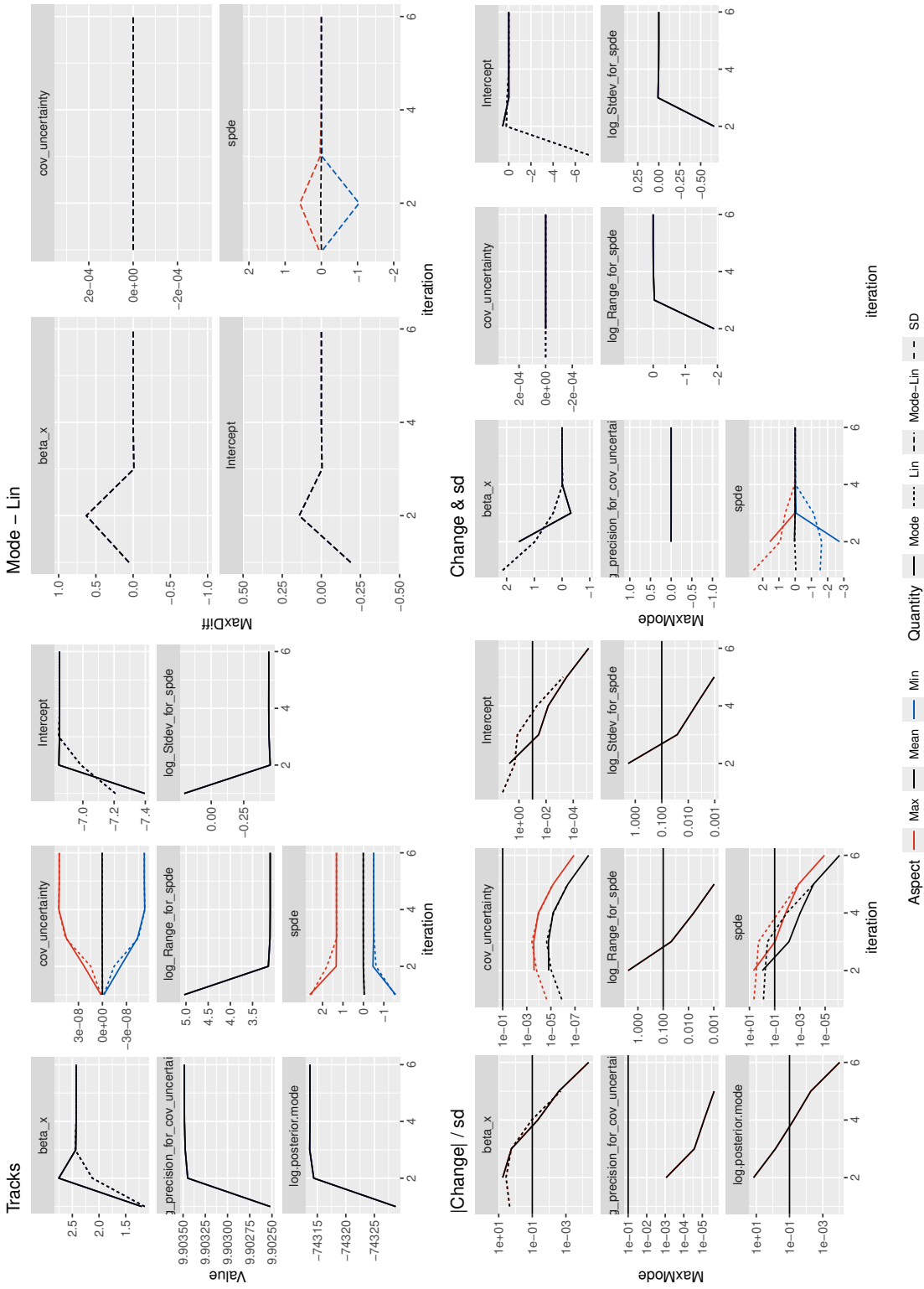
## Convergence plots for fit\_icovap



## Convergence plots for fit\_icovap\_nl



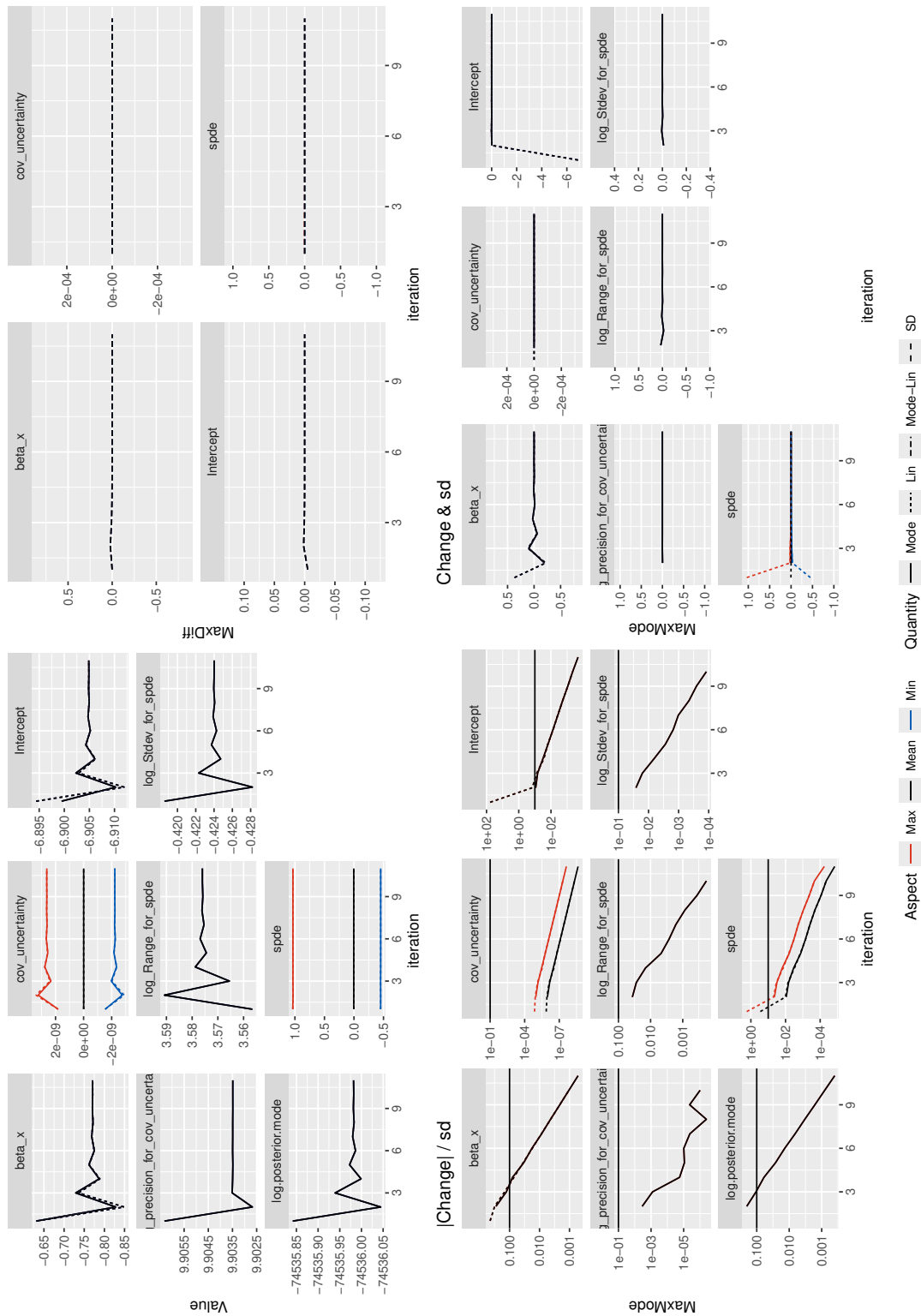
## Convergence plots for fit\_icovap\_pts



## Convergence plots for fit\_icovap\_pts\_nl

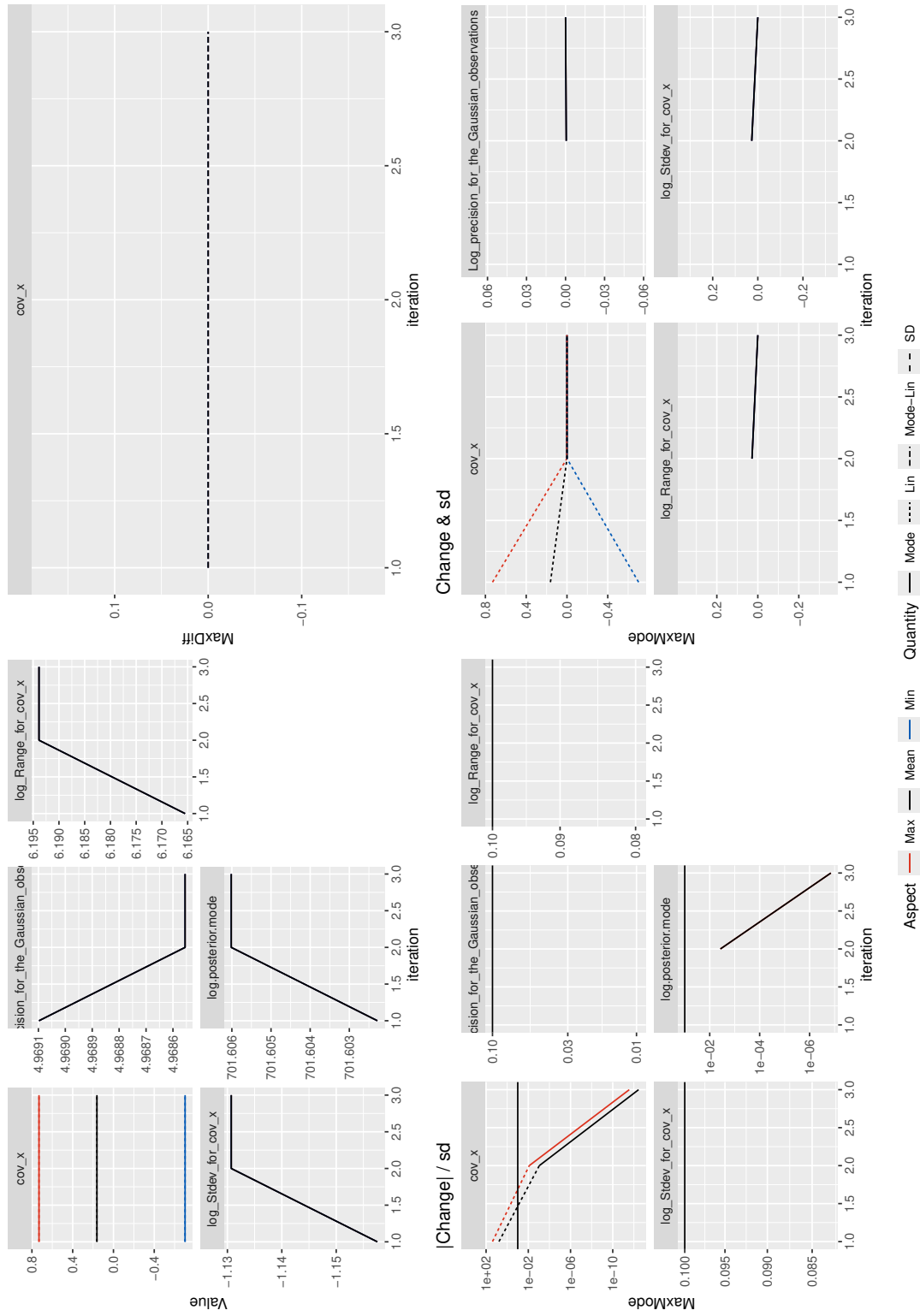
### Tracks

### Mode - Lin

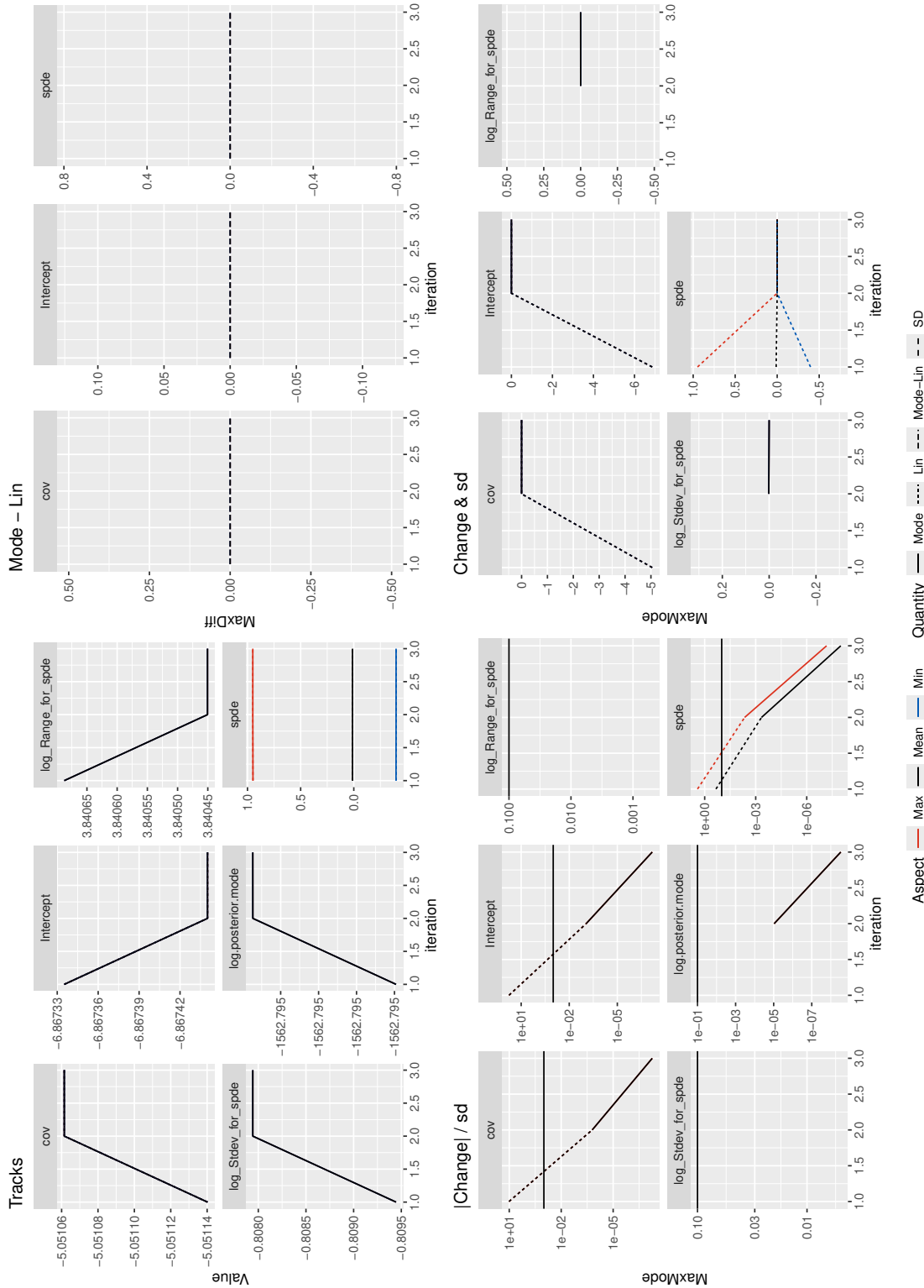


## Convergence plots for fit\_icov\_sd01

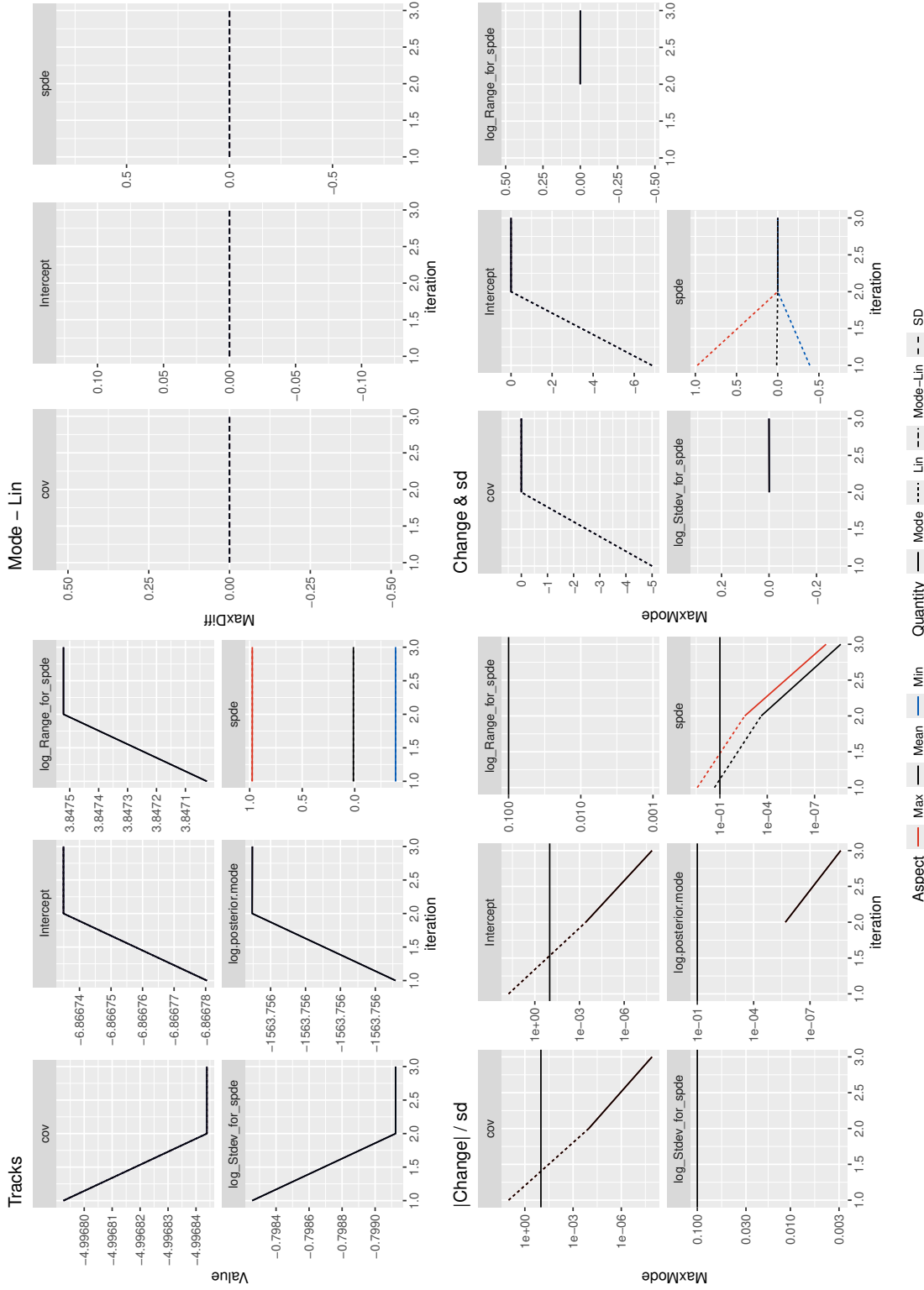
### Tracks



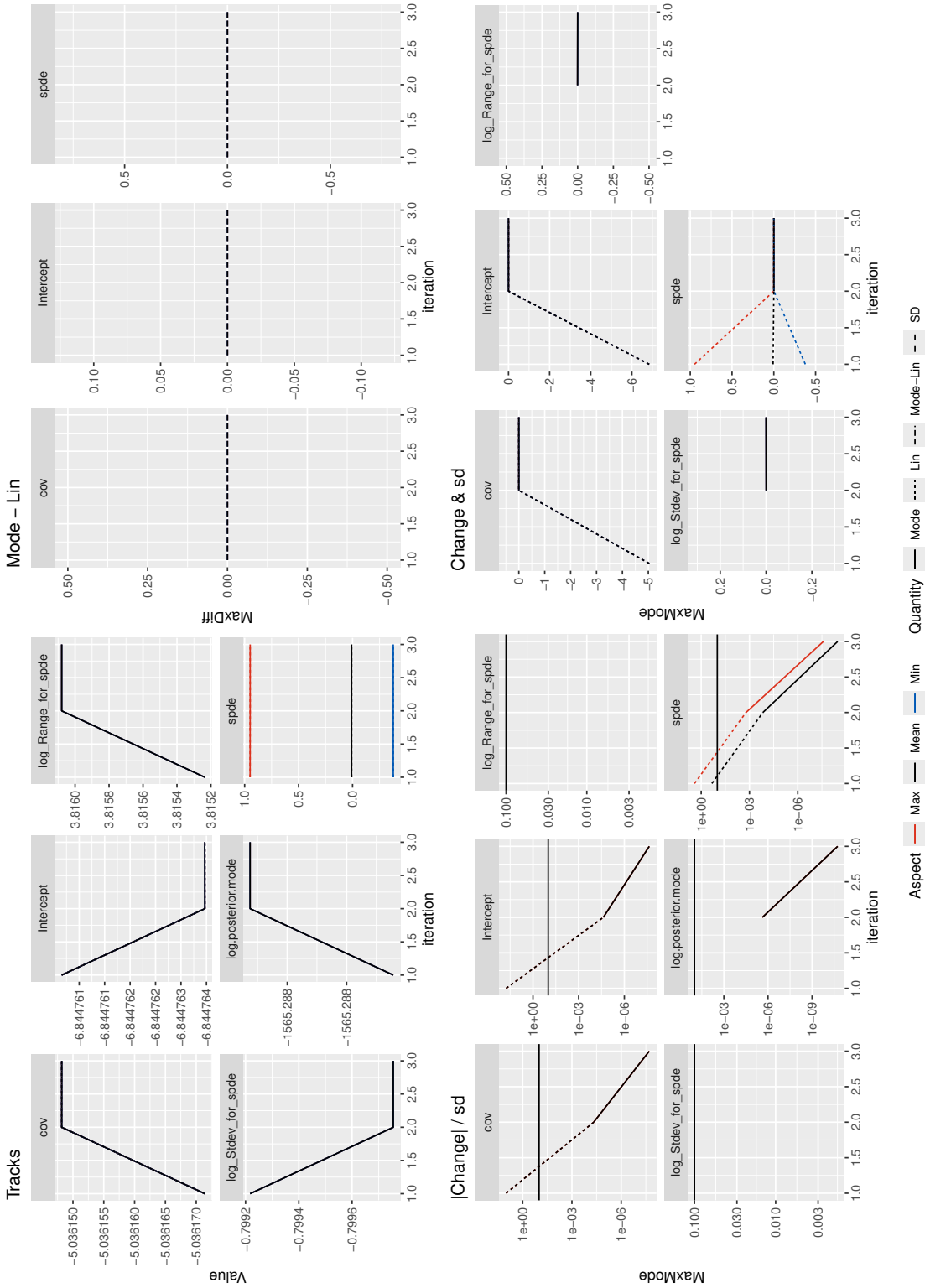
## Convergence plots for fit\_pts



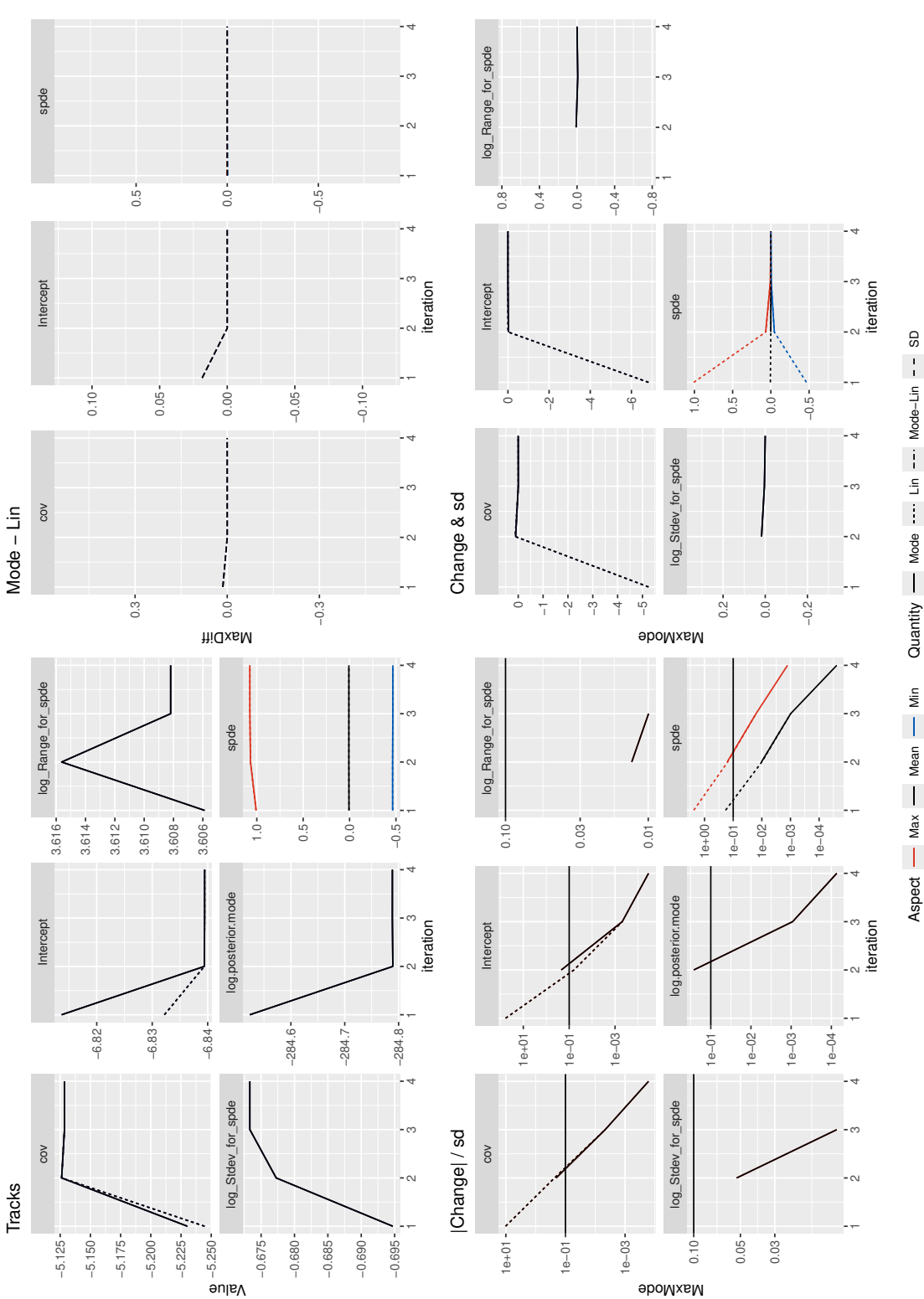
## Convergence plots for fit\_pts\_agg



## Convergence plots for fit\_pts\_poly



## Convergence plots for filly



## E Reproducibility

The results were generated with `INLA` 25.01.23, `inlabru` 2.12.0.9005 and `fmesher` 0.2.0. The shape file of Nepal's municipalities can be downloaded: <https://opendatanepal.com/dataset/nepal-municipalities-wise-geographic-data-shp-geojson-topojson-kml/resource/06b90abc-1380-46ed-b529-e455de6d794d>. The reproducible code for the simulation study can be found in the github repository: <https://github.com/enoch26/misalignedata>.

## References

- Alvioli, M., Guzzetti, F., and Marchesini, I. (2020). Parameter-free delineation of slope units and terrain subdivision of Italy. *Geomorphology*, 358:107124.
- Bachl, F. E., Lindgren, F., Borchers, D. L., and Illian, J. B. (2019). `inlabru`: an R package for Bayesian spatial modelling from ecological survey data. *Methods in Ecology and Evolution*, 10(6):760–766.
- Baddeley, A., Bárány, I., and Schneider, R. (2007). Spatial point processes and their applications. *Stochastic Geometry: Lectures Given at the CIME Summer School Held in Martina Franca, Italy, September 13–18, 2004*, pages 1–75.
- Bayliss, K., Naylor, M., Illian, J., and Main, I. G. (2020). Data-Driven Optimization of Seismicity Models Using Diverse Data Sets: Generation, Evaluation, and Ranking Using Inlabru. *Journal of Geophysical Research: Solid Earth*, 125(11):e2020JB020226.
- Bolin, D. and Lindgren, F. (2017). Quantifying the uncertainty of contour maps. *Journal of Computational and Graphical Statistics*, 26(3):513–524.
- Bolin, D., Simas, A. B., and Wallin, J. (2024). Gaussian Whittle-Matérn fields on metric graphs. *Bernoulli*, 30(2):1611–1639.

Cameletti, M., Gómez-Rubio, V., and Blangiardo, M. (2019). Bayesian modelling for spatially misaligned health and air pollution data through the inla-spde approach. *Spatial Statistics*, 31:100353.

Carpenter, B., Hoffman, M. D., Brubaker, M., Lee, D., Li, P., and Betancourt, M. (2015). The stan math library: Reverse-mode automatic differentiation in c++. [arXiv preprint arXiv:1509.07164](https://arxiv.org/abs/1509.07164).

Dawid, A. P. and Sebastiani, P. (1999). Coherent dispersion criteria for optimal experimental design. *Annals of Statistics*, pages 65–81.

Diggle, P. J. (2013). Spatial point processes. In *Statistical Analysis of Spatial and Spatio-Temporal Point Patterns*. Chapman and Hall/CRC, 3 edition. Num Pages: 28.

Fan, X., Domènec, G., Scaringi, G., Huang, R., Xu, Q., Hales, T. C., Dai, L., Yang, Q., and Francis, O. (2018). Spatio-temporal evolution of mass wasting after the 2008 Mw 7.9 Wenchuan earthquake revealed by a detailed multi-temporal inventory. *Landslides*, 15:2325–2341.

Fuglstad, G.-A., Simpson, D., Lindgren, F., and Rue, H. (2015). Interpretable priors for hyperparameters for Gaussian random fields. [arXiv preprint arXiv:1503.00256](https://arxiv.org/abs/1503.00256), 2.

Fuglstad, G.-A., Simpson, D., Lindgren, F., and Rue, H. (2019). Constructing priors that penalize the complexity of Gaussian random fields. *Journal of the American Statistical Association*, 114(525):445–452.

Gneiting, T. and Raftery, A. E. (2007). Strictly proper scoring rules, prediction, and estimation. *Journal of the American statistical Association*, 102(477):359–378.

Hjelle, Ø. and Dæhlen, M. (2006). *Triangulations and Applications*. Springer Science & Business Media. Google-Books-ID: cRXAe8CVbBYC.

Jones, J. N., Boulton, S. J., Stokes, M., Bennett, G. L., and Whitworth, M. R. (2021). 30-year record of Himalaya mass-wasting reveals landscape perturbations by extreme events. *Nature communications*, 12(1):6701.

Kelejian, H. H. and Prucha, I. R. (1998). A generalized spatial two-stage least squares procedure for estimating a spatial autoregressive model with autoregressive disturbances. *The journal of real estate finance and economics*, 17:99–121.

Kincey, M. E., Rosser, N. J., Densmore, A. L., Robinson, T. R., Shrestha, R., Singh Pujara, D., Horton, P., Swirad, Z. M., Oven, K. J., and Arrell, K. (2023). Modelling post-earthquake cascading hazards: Changing patterns of landslide runout following the 2015 Gorkha earthquake, Nepal. *Earth Surface Processes and Landforms*, 48(3):537–554.

Kincey, M. E., Rosser, N. J., Robinson, T. R., Densmore, A. L., Shrestha, R., Pujara, D. S., Oven, K. J., Williams, J. G., and Swirad, Z. M. (2021). Evolution of coseismic and post-seismic landsliding after the 2015 Mw 7.8 Gorkha earthquake, Nepal. *Journal of Geophysical Research: Earth Surface*, 126(3):e2020JF005803.

Lambert, D. M., Brown, J. P., and Florax, R. J. (2010). A two-step estimator for a spatial lag model of counts: Theory, small sample performance and an application. *Regional science and urban economics*, 40(4):241–252.

Lindgren, F. (2018). Spatially varying mesh quality.

Lindgren, F., Bachl, F., Illian, J., Suen, M. H., Rue, H., and Seaton, A. E. (2024). inlabru: software for fitting latent Gaussian models with non-linear predictors. [arXiv preprint arXiv:2407.00791](https://arxiv.org/abs/2407.00791).

Lindgren, F., Bakka, H., Bolin, D., Krainski, E., and Rue, H. (2020). A diffusion-based spatio-temporal extension of Gaussian Matérn fields. [arXiv preprint arXiv:2006.04917](https://arxiv.org/abs/2006.04917).

Lindgren, F., Bolin, D., and Rue, H. (2022). The SPDE approach for Gaussian and non-Gaussian fields: 10 years and still running. *Spatial Statistics*, 50:100599.

Lindgren, F., Rue, H., and Lindström, J. (2011). An explicit link between Gaussian fields and Gaussian Markov random fields: the stochastic partial differential equation approach. *Journal of the Royal Statistical Society: Series B (Statistical Methodology)*, 73(4):423–498.

Liu, G.-R. (2009). Meshfree methods: moving beyond the finite element method. CRC press.

Llamazares-Elias, L., Latz, J., and Lindgren, F. (2024). A parameterization of anisotropic Gaussian fields with penalized complexity priors. arXiv preprint arXiv:2409.02331.

Loche, M., Alvioli, M., Marchesini, I., Bakka, H., and Lombardo, L. (2022). Landslide susceptibility maps of Italy: Lesson learnt from dealing with multiple landslide types and the uneven spatial distribution of the national inventory. Earth-Science Reviews, 232:104125.

Lombardo, L., Opitz, T., and Huser, R. (2018). Point process-based modeling of multiple debris flow landslides using INLA: an application to the 2009 Messina disaster. Stochastic Environmental Research and Risk Assessment, 32(7):2179–2198.

Lombardo, L., Opitz, T., and Huser, R. (2019). 3 - Numerical Recipes for Landslide Spatial Prediction Using R-INLA: A Step-by-Step Tutorial. In Pourghasemi, H. R. and Gokceoglu, C., editors, Spatial Modeling in GIS and R for Earth and Environmental Sciences, pages 55–83. Elsevier.

Møller, J., Syversveen, A. R., and Waagepetersen, R. P. (1998). Log Gaussian Cox Processes. Scandinavian Journal of Statistics, 25(3):451–482.

Naylor, M., Serafini, F., Lindgren, F., and Main, I. (2022). Bayesian modelling of the temporal evolution of seismicity using the ETAS.inlabru R-package. arXiv:2212.06077 [stat].

Opitz, T., Bakka, H., Huser, R., and Lombardo, L. (2022). High-resolution Bayesian mapping of landslide hazard with unobserved trigger event. The Annals of Applied Statistics, 16(3):1653–1675. Publisher: Institute of Mathematical Statistics.

Quigley, M. C., Hughes, M. W., Bradley, B. A., van Ballegooij, S., Reid, C., Morgenroth, J., Horton, T., Duffy, B., and Pettinga, J. R. (2016). The 2010–2011 Canterbury earthquake sequence: Environmental effects, seismic triggering thresholds and geologic legacy. Tectonophysics, 672:228–274.

Rosser, N., Kincey, M., Oven, K., Densmore, A., Robinson, T., Pujara, D. S., Shrestha, R., Smutny, J., Gurung, K., Lama, S., et al. (2021). Changing significance of landslide hazard and risk after the 2015 Mw 7.8 Gorkha, Nepal earthquake. *Progress in Disaster Science*, 10:100159.

Rue, H., Gómez-Rubio, V., Bakka, H., Lenzi, A., Castro-Camilo, D., Simpson, D., Lindgren, F., and Krainski, E. (2018). *Advanced Spatial Modeling with Stochastic Partial Differential Equations Using R and INLA*. Chapman and Hall/CRC, New York.

Simpson, D., Illian, J. B., Lindgren, F., Sørbye, S. H., and Rue, H. (2016). Going off grid: computationally efficient inference for log-Gaussian Cox processes. *Biometrika*, 103(1):49–70.

Spiekermann, K. and Wegener, M. (2008). Environmental feedback in urban models. *International Journal of Sustainable Transportation*, 2(1):41–57.

Whittle, P. (1954). On stationary processes in the plane. *Biometrika*, pages 434–449.

Whittle, P. (1963). Stochastic-processes in several dimensions. *Bulletin of the International Statistical Institute*, 40(2):974–994.

Williams, J. G., Rosser, N. J., Kincey, M. E., Benjamin, J., Oven, K. J., Densmore, A. L., Milledge, D. G., Robinson, T. R., Jordan, C. A., and Dijkstra, T. A. (2018). Satellite-based emergency mapping using optical imagery: experience and reflections from the 2015 Nepal earthquakes. *Natural Hazards and Earth System Sciences*, 18(1):185–205. Publisher: Copernicus GmbH.